



Ingalls, M. et al. (2018) Paleocene to Pliocene low-latitude, high-elevation basins of southern Tibet: implications for tectonic models of India-Asia collision, Cenozoic climate, and geochemical weathering. *Geological Society of America Bulletin*, 130(1-2), pp. 307-330. (doi:[10.1130/B31723.1](https://doi.org/10.1130/B31723.1))

This is the author's final accepted version.

There may be differences between this version and the published version. You are advised to consult the publisher's version if you wish to cite from it.

<http://eprints.gla.ac.uk/149296/>

Deposited on: 10 October 2017

Enlighten – Research publications by members of the University of Glasgow  
<http://eprints.gla.ac.uk>

1 Paleocene to Pliocene low-latitude high elevation of southern Tibet:  
2 Implications for tectonic models of India-Asia collision, Cenozoic  
3 climate, and geochemical weathering

4 **Miquela Ingalls<sup>1</sup>, David Rowley<sup>1</sup>, Gerard Olack<sup>1</sup>, Brian Currie<sup>2</sup>, Shanying Li<sup>2</sup>, Jennifer**  
5 **Schmidt<sup>4</sup>, Marissa Tremblay<sup>5,6</sup>, Pratigya Polissar<sup>7</sup>, David L. Shuster<sup>5,6</sup>, Ding Lin<sup>8</sup> and**  
6 **Albert Colman<sup>1</sup>**

7 *<sup>1</sup>Department of the Geophysical Sciences, The University of Chicago, Chicago, Illinois 60637,*  
8 *USA*

9 *<sup>2</sup>Department of Geology & Environmental Earth Science, Miami University, Oxford, Ohio*  
10 *45055, USA*

11 *<sup>4</sup>Department of Earth & Environmental Sciences, Lehigh University, Bethlehem, Pennsylvania*  
12 *18015, USA*

13 *<sup>5</sup>Department of Earth & Planetary Science, University of California, Berkeley, California 94720,*  
14 *USA*

15 *<sup>6</sup>Berkeley Geochronology Center, 2455 Ridge Road, Berkeley, California 94709, USA*

16 *<sup>7</sup>Lamont-Doherty Earth Observatory of Columbia University, 61 Route 9W, Palisades, New York*  
17 *10964, USA*

18 *<sup>8</sup>Institute for Tibetan Plateau Research, Chinese Academy of Sciences, Beijing, PRC.*

19 **ABSTRACT**

20 The elevation history of the Tibetan Plateau promises insight into the mechanisms and  
21 dynamics that develop and sustain high topography over tens of millions of years. We present the  
22 first nearly continuous Cenozoic elevation history from two sedimentary basins on the southern  
23 Tibetan Plateau within the latest Cretaceous to Eocene Gangdese arc. Oxygen isotope and  $\Delta_{47}$   
24 clumped isotope compositions of non-marine carbonates allow us to constrain carbonate  
25 formation temperature and reconstruct the paleo-precipitation record of the Eocene to Pliocene

26 Oiyug basin and Paleocene to Eocene Penbo basin. We exploit the systematic decrease of surface  
27 temperature and meteoric water  $\delta^{18}\text{O}$  with elevation to derive paleo-elevation estimates for these  
28 basins. Minimally altered and unaltered pedogenic and lacustrine carbonates from the Oiyug  
29 basin yield  $\Delta_{47, \text{CDES}}$  values of 0.625 to 0.755, that correspond with temperatures of 1 to 30 °C  
30 using a  $\Delta_{47}$  thermometer for low temperature carbonates (Zaarur et al., 2013). Similarly, the  
31 Penbo Basin yields  $\Delta_{47, \text{CDES}}$  values of 0.701 to 0.726, corresponding with temperatures of 6 to  
32 12°C. The apparent evidence for survival of primary clumped isotope values in the face of  
33 substantial burial and heating is an important result for the field of carbonate clumped-isotope  
34 thermometry.

35 Our paleoelevation estimates for the Eocene to Pliocene Oiyug basin (~6.5-4.1  
36 kilometers) support previous evidence (Spicer et al., 2003; Currie et al., 2005; Polissar et al.,  
37 2009; Currie et al., 2016) that high elevations were attained in southern Tibet by at least ~30 Ma.  
38 Stable isotope results allow for the possibility of significant topographic subsidence during the  
39 Miocene as a result of regional extension. In the Penbo basin, our paleoelevation estimates for  
40 the Paleocene to Eocene Nianbo Formation (4.4  $^{+1.3}/_{-1.7}$  km) and Eocene Pana Formation (4.1  
41  $^{+1.2}/_{-1.6}$  km) extend the altitude record of the southern Plateau to pre-India-Asia collision. These  
42 results support the “Lhasaplano” model of an Andean-type continental margin tectonic system.

43 The rise of the Himalayas and Tibet is often invoked to understand isotopic proxies for  
44 global chemical weathering in the Cenozoic and has constrained the debate on the nature of CO<sub>2</sub>  
45 – climate – weathering feedbacks. The nature of the Tibetan paleo-elevations from pre- to post-  
46 collision, as presented here, indicates that high relief at low latitude prevailed on the Asian  
47 margin much earlier than previously thought. Thus high topography alone at low latitude is not  
48 sufficient to account for the Cenozoic weathering proxy record.

49

## 50 INTRODUCTION

51 The debate over when and how the largest and highest plateau on Earth reached its  
52 current altitude is re-framed in the context of recent evidence for an older onset of India-Eurasia  
53 collision. This has important implications for tectonics (Le Pichon et al., 1992; Kapp et al.,  
54 2007), crustal mass balance considerations (Ingalls et al., 2016), and feedbacks among tectonics,  
55 weathering, climate, and the global carbon cycle (e.g., Raymo and Ruddiman, 1992).

56 Recent efforts have established an age of onset of the India-Eurasia continental collision  
57 of ~58 Ma from the Indian deep-water, off-shelf passive continental margin environment  
58 represented by Eocene strata near Sangdanlin in south-central Tibet (DeCelles et al., 2014; Hu et  
59 al., 2015). Ingalls et al. (2016) use these and other data to suggest an age of ~56±2 Ma for  
60 collision of thicker (>20 km) continental crust in the vicinity of Sangdanlin, a younger age of

61 ~51 Ma in the Zaskar region farther west (Gaetani and Garzanti, 1991; Green et al., 2008), and  
62 an essentially unconstrained  $\sim 54 \pm 4$  Ma age nearer to the eastern syntaxis.

63 Our study of the tectonic history of Penbo and Oiyug Basins provides a framework for  
64 the land surface evolution of the southern margin of Eurasia and the sedimentary basins  
65 associated with the Linzizong volcanic arc and younger sedimentary basins during the Cenozoic  
66 collisional history spanning  $\sim 55$  Ma to  $\sim 5$  Ma. We present  $\delta^{18}\text{O}_c$  measurements on lacustrine,  
67 pedogenic, and groundwater calcites from both basins. We use clumped-isotope derived mineral  
68 formation temperatures from a subset of the calcite samples to calculate the original oxygen  
69 isotopic composition of meteoric water ( $\delta^{18}\text{O}_w$ ) from  $\delta^{18}\text{O}_c$  measurements. Finally, we assess  
70 alteration and secondary calcite precipitation with careful petrographic analyses and  
71 characterization of possible diagenesis coupled with our clumped-isotope results.

72 The Oiyug basin sedimentary record spans nearly the entire Cenozoic, making it a unique  
73 site for reconstructing the elevation history of the southern part of the Tibetan Plateau (Fig.1).  
74 Previous paleoaltimetry studies of the basin include paleoenthalpy-derived estimates of  $\sim 15$  Ma  
75 elevations from floral physiognomy (Spicer et al., 2003; Khan et al., 2014), oxygen isotope-  
76 based estimates from carbonate minerals (Currie et al., 2005, 2016), and compound-specific  $\delta\text{D}$   
77 of leaf wax n-alkanes (Currie et al., 2016). These studies have progressively added archives as a  
78 means of testing new proxies and validating prior reconstructions of past hypsometry and  
79 environmental conditions. We provide new stable isotope data from Paleogene nonmarine  
80 carbonates to extend the temporal range of the isotopic record in the Oiyug basin. Additionally,  
81 we present clumped isotope estimates of carbonate formation temperatures to better constrain  
82 paleo-water isotopic compositions for samples previously analyzed by Currie et al. (2016). These

83 data thus help remove bias in paleo-elevation estimates through assumptions regarding  
84 carbonate-water fractionation temperatures.

85         The clumped isotope paleothermometry and stable isotope paleoaltimetry results  
86 presented here support the existence of an Andean-type continental arc on the southern margin of  
87 Eurasia with elevations >4.1 km at the onset or just prior to the onset of the India and Eurasia  
88 collision in the Penbo/Linzhou region near Lhasa. We also advance the elevation record of the  
89 Oiyug Basin, ~160 km west of Lhasa, into the Eocene and provide additional support that the  
90 Oiyug basin was high throughout the Oligocene to Pliocene, building on the work of Currie et al.  
91 (2016). Our high paleo-elevations agree with aspects of the “Lhasaplano” model (Kapp et al.,  
92 2007) – a high-standing Lhasa terrane before India-Asia collision – and provides additional  
93 evidence against models invoking en masse (England and Houseman, 1986; Harrison et al.,  
94 1992, 1995; Molnar et al., 1993) or local plateau uplift (Wang et al., 2006) from significantly  
95 lower elevations in the Neogene.

96

### 97 **Stable isotope paleoaltimetry in the India-Asia collision zone**

98         Numerous investigations have reconstructed the elevation history of the Himalayas and  
99 Tibetan Plateau using the oxygen isotopic composition of non-marine carbonates (Garzzone et  
100 al., 2000; Rowley et al., 2001; Currie et al., 2005; Rowley and Currie, 2006; DeCelles et al.,  
101 2007; Quade et al., 2007; Saylor et al., 2009; Ding et al., 2014; Huntington et al., 2015). The  
102 isotopic composition of the carbonate minerals relates to that of the water from which they  
103 precipitated, which in turn depends upon the composition of meteoric water falling in the  
104 drainage basin. Paleoelevation estimates then derive from the sensitive relationship between  
105 elevation and the isotopic value of precipitation in low-latitude (<35°) orographic systems

106 (Rowley and Garzzone, 2007; Rowley, 2007). This connection is predicted based on atmospheric  
107 thermodynamic modeling of the expected isotopic lapse rate for water vapor and precipitation  
108 and is verified by modern observations (Rowley et al., 2001; Rowley and Garzzone, 2007;  
109 Rowley, 2007). The primary determinants of the  $\delta^{18}\text{O}_w$ -elevation relationship are the temperature  
110 (T) and relative humidity (RH) of the starting air mass. Rowley et al. (2001) used National  
111 Centers for Environmental Prediction (NCEP) reanalysis output of modern global monthly mean  
112 data over entirely oceanic, low latitude ( $<35^\circ$ ) regions to compute the probability density  
113 function of T and RH (Kalnay et al., 1996). Each starting T and RH populates a unique vertical  
114 trajectory through isotopic composition and elevation space. The set of these vertical trajectories  
115 define the expected isotopic compositions of low-latitude atmospheric vapor and use empirical  
116 fitting to the frequency distribution of isotopic composition of precipitation as a function of  
117 elevation. Model elevations are calculated using a quartic function that describes the relationship  
118 between elevation and  $\Delta(\delta^{18}\text{O}_p)$ , where  $\Delta(\delta^{18}\text{O}_p)$  is the difference between the oxygen isotopic  
119 composition of precipitation at sea level and at high altitude. This function is the condensation-  
120 weighted mean polynomial fit to a  $\sim 33000$  iteration regression of 40 years of monthly global  
121 mean T and RH data:

$$122 \text{ Elevation (m)} = -0.0155(\Delta(\delta^{18}\text{O}_p))^4 - 1.1302(\Delta(\delta^{18}\text{O}_p))^3 - 33.939(\Delta(\delta^{18}\text{O}_p))^2 - 642.71(\Delta(\delta^{18}\text{O}_p)) \quad (1)$$

123 This model was assessed by sampling modern stream waters in the Himalaya to central  
124 Tibet, calculating  $\Delta(\delta^{18}\text{O}_p)$ , and comparing their predicted elevations with the actual modern  
125 elevations. This isotopic method yields reasonable fits to these datasets (Rowley et al., 2001;  
126 Currie et al., 2005; Rowley and Currie, 2006; Rowley and Garzzone, 2007; Hren et al., 2009).  
127 There is some tendency of the model to underestimate elevations rather than overestimate,

128 suggesting that it is likely a conservative proxy for past elevations. Further discussion of the  
129 paleoaltimetry model parameters can be found in the Appendix.

130 The Siwalik Group is favored as an archive for low-latitude, near sea level climate  
131 conditions in the Neogene, as both carbon and oxygen isotopic compositions are interpreted to be  
132 primary (Quade et al., 1995; Quade and Cerling, 1995), and there exists excellent control on  
133 depositional age and burial history. We calculate  $\Delta(\delta^{18}\text{O}_p)$  using the mean low elevation  $\delta^{18}\text{O}_w$   
134 value determined from 2.5 to 12 Ma paleosol carbonates (1-5 cm diameter) of the Siwalik Group  
135 in Pakistan and Nepal (Quade and Cerling, 1995; Quade et al., 2013). The Siwalik carbonates are  
136 presumed to precipitate in near isotopic equilibrium from soil water, which is closely related to  
137 meteoric water. Temperature- and mineral-specific fractionation factors ( $\alpha_{\text{CO}_3\text{-H}_2\text{O}}$ ) are used to  
138 derive paleo-surface or groundwater composition ( $\delta^{18}\text{O}_w$ ) from carbonate isotopic values ( $\delta^{18}\text{O}_c$ ).  
139 We calculate  $\delta^{18}\text{O}$  of water in the mineralizing solution using fractionation equations for calcite  
140 (Kim & O'Neil, 1997), dolomite (Vasconcelos et al., 2005), and siderite (Zhang et al., 2001)  
141 (Tables 1 and 2), which are calculated using the average  $\Delta_{47}$ -derived temperature for each  
142 geologic unit. The dominant controls on  $\delta^{18}\text{O}_c$  values of unaltered to minimally altered carbonate  
143 are extent of Rayleigh distillation of water vapor in the air masses that deliver precipitation to the  
144 region, which scales with elevation (Dansgaard, 1954) and extent of evaporative  $^{18}\text{O}$ -enrichment.  
145 An assessment of evaporative enrichment is incorporated into our presentation of the isotopic  
146 data.

147  $T(\Delta_{47})$  for paleosols from the upper 2.5 km (<5.5 Ma) of the Siwalik Group at Surai  
148 Khola in Nepal were <34°C (Quade et al., 2013). Although the deposits older than 5.5 Ma  
149 experienced greater burial depths and yielded higher  $T(\Delta_{47})$ , Quade et al. (2013) argues that the  
150 Surai Khola sedimentary package is rock-buffered and has undergone little recrystallization, and

151 therefore  $\delta^{18}\text{O}_c$  is preserved. The average  $\delta^{18}\text{O}_c$  of the Neogene Siwaliks is  $-7.4\text{‰VPDB}$  (Quade  
152 et al., 2013). Due to the extent of  $\Delta_{47}$  alteration during burial in Surai Khola, we do not use the  
153 clumped isotope-derived temperatures from deposits older than 5.5 Ma for the calculation of  
154  $\delta^{18}\text{O}_w$  from  $\delta^{18}\text{O}_c$ . Instead, we use low elevation warm month mean temperatures (WMMT) of  
155  $28.1\pm 3.4^\circ\text{C}$  derived from a CLAMP (Climate Leaf Analysis Multivariate Program) analysis of  
156 two lower Siwalik mid-Miocene fossil flora (Khan et al., 2014). We assign a  $\delta^{18}\text{O}_w$  of  $-6.6\pm 2.8\text{‰}$   
157 VSMOW as our low elevation precipitation isotopic value ( $\delta^{18}\text{O}_w$ ) in the Miocene and older  
158 sediments and  $-4.6\pm 1.4\text{‰}$  VSMOW to the Pliocene sediments to account for climate change  
159 during the Cenozoic. Error is propagated through the paleo-elevation model using the sum in  
160 quadrature of the uncertainties associated with calculating mean  $\delta^{18}\text{O}_w$  values for each sample, as  
161 well as the  $2\sigma$   $\Delta_{47}$  uncertainty.

162

### 163 **A Case for Multiple Proxies in Reconstructions of Ancient Topography and Environments**

164 Carbonate stable isotope paleoaltimetry depends critically on the preservation of a  
165 primary  $\delta^{18}\text{O}_c$  signal in the variably altered rocks preserved in collisional zones. Primary  
166 carbonate isotopic compositions are prone to alteration and diagenetic resetting by deep burial  
167 (Leier et al., 2009), which can shift  $\delta^{18}\text{O}_c$  to lower values, eliminating the possibility of  
168 constraining elevation history using the stable isotope record (Garzzone et al., 2004; Leier et al.,  
169 2009). Such a lowering of  $\delta^{18}\text{O}_c$  would result in an incorrectly high paleo-elevation interpretation  
170 (Garzzone et al., 2004). We employ petrography, vitrinite reflectance, thermochronometric data,  
171 and clumped isotope thermometry to assess alteration and rule out the use of isotopic data from  
172 thermally mature samples in paleo-elevation reconstructions.



173           The exploitation of multiple paleo-elevation and paleo-environmental proxies in a single  
174 stratigraphic package allows for calibration and checks among conventional archives. Currie et  
175 al. (2016) conducted such a study in the Oiyug basin, characterizing ~30 My of relative elevation  
176 stasis in the evolving depositional environment of the Oiyug Basin. Currie et al. (2016)  
177 synthesized multiple proxies for paleo-meteoric water ( $\delta^{18}\text{O}_{\text{FeCO}_3}$ ,  $\delta^{18}\text{O}_{\text{CaCO}_3}$ ,  $\delta\text{D}_{\text{leaf wax}}$ ) to provide  
178 mid-Miocene (5.1 km  $^{+1.3}/_{-1.9}$  km) and late-Oligocene to mid-Miocene (4.1 km  $^{+1.2}/_{-1.6}$  km) paleo-  
179 elevation estimates of this region, and a unique opportunity for testing the fidelity of other stable  
180 isotope proxies. Khan et al. (2014) determined a mid-Miocene (~15 Ma) paleo-elevation of  
181 5.54±0.73 km by reevaluating paleo-enthalpy estimates for a fossil flora locality (Spicer et al.,  
182 2003) in the Oiyug Basin relative to new fossil flora localities in the Siwaliks, their sea level  
183 proxy.

184           Clumped isotopes can be powerful in studying the evolution of ancient land surfaces  
185 when the original isotopic signature is preserved (Ghosh et al., 2006b; Quade et al., 2007). In this  
186 study, we apply calcite  $\Delta_{47}$ -derived formation temperatures ( $T(\Delta_{47})$ ; Table 3) to previously  
187 published (Currie et al., 2016; Fig. 1) and new oxygen isotopic compositions of lacustrine and  
188 pedogenic carbonates (n=141) to better estimate  $\delta^{18}\text{O}_w$  of paleo-waters (Tables 1 and 2).  $\delta^{18}\text{O}_w$  is  
189 the isotopic composition of the water from which the carbonate formed, assuming equilibrium.  
190 We use this value to represent the precipitation-weighted hypsometric mean isotopic  
191 composition of surface water, which then enters into standard stable isotope paleoaltimetric  
192 determinations (Rowley, 2007).

193

#### 194 **Geologic setting**

195 *Linziyong volcanic arc, southern Lhasa block*

196 Cretaceous-early Tertiary Gangdese arc magmatism is commonly attributed to this northward  
197 subduction of Indian oceanic lithosphere beneath Tibet (Burg et al., 1983; Tapponnier et al.,  
198 1986, 1981). Neo-Tethyan oceanic lithosphere attached to Indian plate was subducted beneath  
199 southern Eurasia prior to and during the early stages of continent-continent collision along the  
200 Indus-Yarlung Suture (IYS)—the tectonic boundary between the Indian subcontinent and  
201 Eurasia (Murphy et al., 1997; Ding and Lai, 2003). The volcanism represented by the Linzizong  
202 Group (~69 to 43 Ma) and post-Early Cretaceous (<100 Ma) Gangdese batholiths constitute the  
203 active continental margin of southern Eurasia.

204 Portions of the central to northern Lhasa terrane were covered in shallow marine platform  
205 sediments during the Aptian-Albian, potentially as far south as the Penbo basin (Kapp et al.,  
206 2005; Leier et al., 2007), demonstrating that much of the Lhasa terrane was at sea level in the  
207 mid-Cretaceous (Zhang, 2000). These marine sequences place a lower bound on the uplift  
208 history of the southern margin of Eurasia, but the timing of the tectonic and magmatic rise of the  
209 southern Lhasa terrane and Linzizong volcanic arc to modern elevation remains controversial.

210

#### 211 *Penbo/Linzhou Basin*

212 The Penbo, also referred to as the Linzhou, basin (Fig. 1B) is located approximately 35  
213 km north of Lhasa and 75 km north of the IYS. The modern hypsometric mean elevation of the  
214 basin drainage area is ~4200 m with surrounding peaks <5300 m. The samples in this study were  
215 collected from modern elevations of 3950 to 4200 m.

216 This basin exposes a sedimentary and volcanic record spanning pre- to syn-collisional  
217 time (~67 to ~48 Ma) and is the type locality of the non-marine Linzizong Group (He et al.,  
218 2007). Here, the stratigraphic thickness of the Linzizong Group is approximately 3500 m (He et

219 al., 2007). We focus our paleoelevation reconstruction in the Penbo Basin primarily on the ~56.5  
220 to ~53 Ma Nianbo Fm and the ~50 Ma upper Pana Fm because they preserve abundant lacustrine  
221 limestone, groundwater and paleosol carbonate nodules, and they have pre- to early syn-  
222 collisional depositional ages. The age range of the sampled Linzizong stratigraphy of the Penbo  
223 Basin is well constrained by zircon U/Pb radiometric ages of tuffs near the base and top of the  
224 measured stratigraphy (Ding et al., 2014; He et al., 2007). Additionally, a hornblende  $^{40}\text{Ar}/^{39}\text{Ar}$   
225 age from a mafic dike intruding the Nianbo Formation provides a latest possible age of  
226 Linzizong deposition within Penbo basin (Yue and Ding, 2006).

227         The sedimentary rocks of the Nianbo Formation in the Oiyug Basin are mapped as age-  
228 correlative with the type Nianbo in the Penbo Basin. These ages together with stratigraphic and  
229 lithological correlation allow us to place the paleo-altitude results from the Nianbo Formation,  
230 discussed below, in the Oiyug Basin into temporal and regional context.

231         The ~240 meter-thick Paleocene-Eocene Nianbo Fm (Fig. 2) unconformably overlies the  
232 lower Upper Cretaceous Shexing Fm in this section. Nearby, the Nianbo conformably to  
233 disconformably overlies the Paleocene Dianzhong Fm, that in turn unconformably overlies the  
234 Shexing and Takena Formations. The Linzizong Group and particularly the Nianbo Fm are  
235 spatially heterogeneous such that no section in the field is representative. Nonetheless, the  
236 overall stratigraphy and sedimentology of the Nianbo Fm can be broken into three lithologic  
237 sequences: two upward-fining packages with an ash-flow tuff and massive conglomerate  
238 between the two. The lower subunit is dominated by purple and green laminated mudstones and  
239 volcanoclastic-dominated sandstones at its base. The mudstones contain nodular carbonate,  
240 pedogenic features, mottling, and bioturbation, and at least one non-deformed snail shell. These  
241 are overlain by fine-grained red siltstones abundant in pedogenic carbonate interbedded with

242 yellow to brown lacustrine marls. Fossil *ostracods* are found in the marls. Shell morphology is  
243 preserved but body cavities have sparry calcite infill. The uppermost part of the lower Nianbo  
244 Fm preserves well-developed calcic paleosols (Fig. 3).

245 The middle Nianbo subunit is defined by a period of vigorous volcanic activity. The  
246 volcanic agglomerate base is topped by a 5 meter-thick andesitic lava flow. A 25 meter-thick  
247 welded tuff/ash flow tops this sequence, followed by ~40 meters of gravel conglomerate.

248 The basal 10 meters of the upper Nianbo subunit is composed of interbedded red  
249 mudstones and medium to very coarse sandstones. The uppermost mudstones contain  
250 groundwater carbonate horizons and abundant pedogenic carbonate. Approximately 10 meters of  
251 coarse to gravel conglomerate overlies the ped-rich layers. The conglomerate is topped by ~10  
252 meters of alternating fine and coarse sandstones. The uppermost ~80 meters of the Nianbo are  
253 more variable in composition and depositional conditions: fining-upwards conglomerates, meter-  
254 thick micritic limestone beds, horizontally laminated medium-grained sandstones, sandy  
255 limestones, and paleosol horizons. Ostracods are found in one of the uppermost lacustrine  
256 limestone beds, implying a period of relatively shallow and open lakes with long residence times  
257 (Ding et al., 2014). The majority of the samples used for measuring paleo-elevation of the  
258 Nianbo Fm were derived from this upper subunit.

259 The uppermost preserved rocks of the Linzizong Group are the Pana Formation, a lower  
260 sequence of mostly andesitic volcanics and volcanoclastics overlain by a predominantly  
261 lacustrine succession of shales, mudstones, sandstones, and both pedogenic and lacustrine  
262 carbonates. The upper subunit of the Pana Formation was deposited between  $50.5 \pm 2.4$  Ma and  
263  $48.4 \pm 1.0$  Ma, as dated by U/Pb zircon laser ablation geochronology (Ding et al.,  
264 2014). Additionally, Eocene-age volcanic dikes cut the Nianbo and lower Pana Formations (He

265 et al., 2007). Locally Linzizong sediments may have experienced elevated temperatures due to  
266 this intrusive activity.

### 267 *Oiyug Basin*

268 The Oiyug Basin (Fig. 1C), also referred to as the Wuyu Basin, and mischaracterized as  
269 the Namling Basin (Spicer et al., 2003) that actually lies slightly farther west, is located 160 km  
270 west of Lhasa and 60 km north of the Indus Yarlung Suture (IYS). The basin covers an area of  
271 approximately 300 km<sup>2</sup> (Wang and Chen, 1999) of the Lhasa terrane. Sampled localities are  
272 currently at elevations of 4300-4400 m with surrounding elevations >5600 m. The modern  
273 hypsometric mean elevation of the basin drainage area is ~4600 m.

274 Paleogene-Neogene strata in the Oiyug Basin consist of the Paleocene Dianzhong,  
275 Paleocene-Eocene Nianbo Formation, the Oligocene-Miocene Rigongla Formation, the Miocene  
276 Gazhacun Group, and the Miocene-Pliocene Oiyug Formation. In this basin, the Nianbo  
277 Formation is comprised of andesite, fluvial volcanoclastics, lacustrine sandstones, mudstones and  
278 limestones, and argillaceous/calcareous paleosols. In this study, an approximately 500 m-thick  
279 section of the Nianbo Formation was measured in the northern part of the Oiyug Basin (Fig. 4).  
280 The section is bordered to the south by a low angle thrust fault that places Nianbo sediments  
281 above the younger Rigongla Formation. To the north, the section is separated from the overlying  
282 Rigongla Formation by an angular unconformity. The angular unconformity marks an erosional  
283 surface that removed upper Nianbo and Pana Fm sediments from this location prior to Rigongla  
284 Fm deposition (Fig. 1C).

285 The lower parts of the measured Nianbo Formation (Fig. 4) consists of ~270 m of  
286 andesitic volcanoclastic rocks sparsely interbedded with thin (~20-30 cm-thick) paleosol  
287 horizons. Pedogenic calcite (W0628-1) was collected from a moderately developed paleosol

288 horizon ~275 meters above the base of the section. Pedogenic calcite nodules in this part of the  
289 section are gray-green, texturally micritic, and typically elongate (~1 cm by 2-3 cm), surrounded  
290 by red muddy matrix. The matrix material is primarily composed of weathered volcanics.

291 Above the volcanics and weathered volcanics, the Nianbo Formation is dominated by  
292 lacustrine limestone, sandstone, and mudstone. The depositional environment is interpreted as  
293 marginal lacustrine. The dominant lithology at the base of the thick limestone package is  
294 laminated sandy limestone (W0628-2) with very fine-grained calcareous matrix and fine to  
295 medium quartz grains. The sandy beds interbedded with the marl limestone cliffs are interpreted  
296 as terrestrial alluvium deposited in an offshore to near-shore lake environment (Mack and  
297 Rasmussen, 1984). The sedimentology of this sequence and environmental interpretations align  
298 with the lithology and sequence stratigraphy of the upper subunit of the Nianbo Formation in the  
299 Penbo basin (Ding et al., 2014; this study). Approximately 10 meters above this sampling  
300 locality, sandy limestone fines to oxidized siltstone and red mudstone with authigenic calcareous  
301 concretions (W0628-3). The Nianbo Formation in the Oiyug Basin is mapped as Paleocene to  
302 early Eocene in age. While undated in the immediate study area, U/Pb ages from the Nianbo  
303 Formation sampled ~40 km to the west near Namling range from  $63.78 \pm 0.46$  Ma to  $50.2 \pm 2.2$  Ma  
304 (Wang et al., 2014) in line with dating in the type area in the Penbo Basin to the east.

305 Rigongla Formation rhyolitic and andesitic volcanoclastic rocks lie unconformably above  
306 the described section of Nianbo. A rhyolite (W0628-4) sampled from these volcanics yielded a  
307 late Oligocene age of  $28.90 \pm 1.52$  Ma (potassium feldspar  $^{40}\text{Ar}/^{39}\text{Ar}$ ; Table 4; Fig. A1), similar to  
308 a ~31 Ma K/Ar age reported for the lower Rigongla Formation elsewhere in the basin (Zhu et al.,  
309 2006). Given these ages, and the ~50 Ma age for the upper Nianbo in the region, ~20 million  
310 years of rock record is likely missing at the unconformity between the Nianbo and Rigongla

311 formations in the study area. Additional radiometric ages of volcanics interbedded with the  
312 Linzizong strata are needed in order to assess the continuity of the rock record preserved in the  
313 Oiyug basin.

314 The Rigongla Formation measured at the headwaters of the Ramaqu, consists of dacitic to  
315 andesitic volcanic rocks interbedded with an upward-fining >500 meter thick sedimentary  
316 sequence of conglomerates, sandstones, and mudstones (Fig. 1C) (Currie et al., 2016). Paleosol  
317 and groundwater carbonate nodules were collected from a ~20 meter thick mudstone horizon  
318 between alluvial fan and fluvial channel conglomerate sequences in the Rigongla Formation  
319 (Currie et al., 2016). The nodules are texturally micritic and 3-15 cm in diameter.

320 The Gazhacun Group, previously described as the Manxiang Formation (Zhu et al.,  
321 2006), directly overlies the volcanics of the upper Rigongla Formation. The base of the  
322 Gazhacun Group is comprised of ~140 meters of red and gray overbank mudstones and sparse  
323 fluvial channel sandstones and conglomerates (Currie et al., 2016). The overbank mudstones host  
324 clay-rich paleosol horizons with well-developed pedogenic calcite nodules 0.25 to 1.5 cm in  
325 diameter. The middle Gazhacun is interpreted to record a lacustrine depositional environment,  
326 represented by ~225 meters of gray, green, and light red shale and mudstone, and thin beds of  
327 siltstone and fine-grained sandstone (Currie et al., 2016). Samples from lacustrine strata of the  
328 middle Gazhacun are both early diagenetic calcite and dolomite nodules. Given the paucity of  
329 datable volcanics in the Rigongla Formation and lower-middle Gazhacun Group strata, the age of  
330 this stratigraphic interval is liberally bracketed between two K-feldspar  $^{40}\text{Ar}/^{39}\text{Ar}$  ages from the  
331 units above and below the lower Gazhacun: a rhyolite in the Rigongla Fm (28.90±1.52 Ma) and a  
332 felsic tuff in the upper Gazhacun (~15 Ma; Spicer et al., 2003).

333           The upper Gazhacun Group, measured along the Badamaqen, consists of ~100 meters of  
334 tuffaceous conglomerate and fining upwards sandstone, interbedded with carbonaceous siltstone,  
335 mudstone, shale, and coal. A siderite nodule (618A) and four shales were collected for isotopic  
336 analyses near the top of the floral locality section of Spicer et al. (2003) and Khan et al.  
337 (2014). The age of the top of the upper Gazhacun Group is constrained by  $^{40}\text{Ar}/^{39}\text{Ar}$  age of ~15  
338 Ma from felsic tuff deposits within the upper part of the unit and from the base of the overlying  
339 Zongdang Group (Spicer et al., 2003). The Zongdang Group consists of ~1900 meters of ash  
340 flow tuffs and volcanoclastics (Zhu et al., 2006; Chen et al., 2008). Ash flow tuffs from the  
341 uppermost Zongdang Group yielded K/Ar ages ranging from  $8.23 \pm 0.13$  to  $7.92 \pm 0.15$  Ma (Chen  
342 et al., 2008).

343           The upper Miocene-Pliocene Oiyug Formation conformably to unconformably overlies  
344 the Zongdang Group. This unit is an ~1 km-thick package of basin-centered lacustrine deposits  
345 and associated basin margin fan delta, fluvial, overbank, and swamp deposits (Zhu et al., 2006).  
346 The upper Oiyug Formation is dominated by lacustrine marl and mudstone (Currie et al., 2016).  
347 Lacustrine marl calcitic limestone, shales, nodular calcite, and nodular siderite were collected for  
348 isotopic analyses from the middle to upper Oiyug Formation, with an interpreted depositional  
349 age of ~5 Ma (Chen et al., 2008).

350

## 351 **METHODS**

352           In this study, we determined the  $\delta^{18}\text{O}_{\text{carb}}$  and  $\delta^{13}\text{C}_{\text{carb}}$  values of 105 carbonate samples  
353 collected from Paleocene to Eocene strata in the Penbo basin and 36 carbonate samples from the  
354 Eocene to Pliocene strata in the Oiyug basin. Of these samples, 7 from Penbo and 12 from Oiyug  
355 were used to determine clumped-isotope estimates of carbonate precipitation temperature



356 T( $\Delta_{47}$ ). Currie et al. (2016) reported carbon and oxygen stable isotopic compositions of  
357 Oligocene to Pliocene strata in the Oiyug basin, and this work adds new stable isotope  
358 compositions from Paleogene strata. We obtained a potassium feldspar total fusion  $^{40}\text{Ar}/^{39}\text{Ar}$  age  
359 for Rigongla Formation volcanics in the Oiyug basin in order to provide an upper bound for  
360 Nianbo Formation deposition. We measured apatite (U-Th)/He ages for the Qianggeren granite  
361 in the Penbo basin in order to constrain the erosional unroofing age.

362

### 363 **Carbonate Sample Preparation**

364 The outer layer of carbonate samples was removed to expose fresh material for stable  
365 isotope analysis and making petrographic slides. Samples were powdered using a Foredom TX  
366 low speed drill with a Brasseler US#2 HP Round bit at low speed to avoid significant frictional  
367 heating and the potential for carbonate C-O bond reordering.

368 Petrographic slides were made for a subset of samples that appeared minimally or  
369 unaltered in hand sample in order to evaluate for visual signs of aqueous alteration (dissolution  
370 features, recrystallization textures, secondary carbonates, authigenic metal oxide precipitates,  
371 etc.; see Tables 5-6). Petrographic analyses allow distinction between two contrasting textural  
372 relationships among preserved carbonates. One group consists of pedogenic carbonate nodules  
373 and lacustrine limestone, some of which preserve ostracods and charophyte debris within a  
374 micritic matrix with only very minor spar-filled vugs and/or microspar recrystallization (Tables 5  
375 and 6). This minimally altered group also includes wackestones lacking evidence of secondary  
376 recrystallization. The second group, consisting of lacustrine limestone and pedogenic carbonate  
377 nodules, is characterized by varying degrees of alteration including extensive development of  
378 sparry calcite, oxidation, cross cutting veins, and increase in grain size of the formerly micritic

379 matrix and sparry calcite veins. We discuss our isotopic results with respect to our petrographic  
380 assessment of degree of alteration.

381 For the Penbo Basin, the  $\Delta_{47}$  analyses were carried out independently from the  
382 petrographic observations (isotopic measurements and petrographic observations shared only  
383 after both were completed). This blind test was carried out at Miami University as a means of  
384 assessing our ability to correctly characterize alteration by petrographic observation. For the  
385 Oiyug Basin, petrographic and  $\Delta_{47}$  analyses were both completed at the University of Chicago.

386

### 387 **Standard stable isotope measurements**

388 Isotopic measurements were completed in the stable isotope facility in the Department of  
389 the Geophysical Sciences at The University of Chicago. All samples were analyzed for calcite  
390  $\delta^{18}\text{O}_c$  and  $\delta^{13}\text{C}_c$  and weight %  $\text{CaCO}_3$  using a Gas Bench II (Thermo, Bremen, Germany)  
391 connected to a Delta V Plus (Thermo) stable isotope ratio mass spectrometer. Stable oxygen and  
392 carbon isotopic measurements are reported in ‰ using conventional delta notation:

$$393 \quad \delta^{18}\text{O}_c = \left( \frac{(^{18}\text{O}/^{16}\text{O})_{\text{sample}}}{(^{18}\text{O}/^{16}\text{O})_{\text{standard}}} - 1 \right) \times 1000 \text{ ‰} \quad (2)$$

394 with analogous formulation for  $\delta^{13}\text{C}_c$ . All carbonate oxygen and carbon isotopic compositions  
395 are reported on the VPDB scale.

396 Samples were weighed out to yield roughly 100-200  $\mu\text{g}$   $\text{CaCO}_3$  equivalent. Comparable  
397 size ranges of the isotopic standards NBS-18 ( $\delta^{13}\text{C} = -5.01\text{‰}$  VPDB;  $\delta^{18}\text{O} = -23.20\text{‰}$  VPDB;  
398 Coplen et al., 2006), NBS-19 ( $\delta^{13}\text{C} = 1.95\text{‰}$  VPDB;  $\delta^{18}\text{O} = -2.19\text{‰}$  VPDB; Gonfiantini, 1983),  
399 and periodically LSVEC ( $\delta^{13}\text{C} = -46.6\text{‰}$  VPDB; Coplen et al., 2006) were interspersed with the  
400 Tibetan samples. These standards were used to assess, and correct when needed, for linearity  
401 and drift. Results for carbonate  $\delta^{13}\text{C}_c$  and  $\delta^{18}\text{O}_c$  are reported on the VPDB scale ( $\pm 0.1\text{‰}$

402 analytical uncertainty). The calculated values for water in isotopic equilibrium with the  
403 carbonate minerals,  $\delta^{18}\text{O}_w$ , are reported on the VSMOW scale.

404

#### 405 **Clumped isotope ( $\Delta_{47}$ ) analyses**

406 The carbonate clumped isotope thermometer is established using the temperature-  
407 dependent enrichment of “clumped” isotopologues in carbonates, and can be used to determine  
408 carbonate mineralization temperature (Ghosh et al., 2006a; Ghosh et al., 2006b; Eiler, 2007;  
409 Huntington et al., 2009; etc.). The “clumping” refers to ions or molecules with more than one  
410 rare isotope (e.g., a clumped carbonate ion:  $^{13}\text{C}^{18}\text{O}^{16}\text{O}_2^{2-}$ ). The formation of carbonate minerals  
411 in internal isotopic equilibrium results in greater clumping at lower temperatures. The clumped  
412 isotope composition of carbonates is measured on  $\text{CO}_2$  released by phosphoric acid digestion of  
413 carbonate minerals. The composition is reported as a  $\Delta_{47}$  value expressed in units of ‰, where  
414  $\Delta_{47}$  is defined as the enrichment in clumped  $\text{CO}_2$  with molecular mass 47 (dominated by  
415  $^{13}\text{C}^{18}\text{O}^{16}\text{O}$ ) relative to the amount of clumping expected based on a stochastic distribution of C  
416 and O isotopes as measured in the bulk isotopic composition:  $\Delta_{47} = (R^{47}/R^{47*} - 1) \times 1,000$  ‰,  
417 where  $R^{47} = \text{mass } 47 / \text{mass } 44$ , and  $R^{47*}$  denotes analogy to  $R^{47}$ , but reflects the abundance  
418 predicted with a random distribution of isotopes.  $\delta_{47}$  is defined similarly to  $\delta^{13}\text{C}$  and  $\delta^{18}\text{O}$ , using  
419 the abundance ratios of  $\text{CO}_2$  isotopologues (rare mass 47 isotopologues compared to the common  
420 mass 44 isotopologue) referenced to a working gas that defines “zero”.

421 Carbonates were digested overnight in 5-7 ml of ~103% anhydrous phosphoric acid at  
422 26°C with acid densities of 1.92-1.94 g/cm<sup>3</sup>, verified gravimetrically prior to each use. Following  
423 acid digestion, the resultant  $\text{CO}_2$  was purified on a glass vacuum line to remove trace water  
424 vapor and isobaric contaminants. Gas was transferred through a cryogenic water trap (glass

425 tubing immersed in LN<sub>2</sub>-ethanol slurry at -80°C) with the CO<sub>2</sub> frozen out (LN<sub>2</sub>) downstream and  
426 with non-condensable gases then pumped away. These non-condensable gases typically gave a  
427 pressure of 0.1-0.2 Torr in a 250 ml volume segment of the vacuum line and reaction vessel as  
428 compared with a CO<sub>2</sub> partial pressure of 80 Torr in 15 mL. The frozen CO<sub>2</sub> sample was isolated  
429 from the rest of the system and warmed, with pressure reading serving as a monitor of CO<sub>2</sub> yield  
430 from the sample digestion (902 piezo vacuum transducer, MKS Instruments, Andover,  
431 MA). Then the CO<sub>2</sub> was passed through a Haysep Q (60/80 mesh, Supelco, Bellefonte, PA,  
432 USA) filled U-trap (6 mm i.d., 24 cm packed length) with an approximately 2 cm thick layer of  
433 powdered Ag<sub>3</sub>PO<sub>4</sub> (Strem Chemicals, Newburyport, MA, USA) mixed with quartz chips at the  
434 inlet end. Small quartz wool plugs capped with silver wool plugs were used on both ends of the  
435 column to retain fine mesh and powder packing material. The U-trap thus packed served as a  
436 chromatography column. We optimized the temperature of CO<sub>2</sub> chromatography by varying  
437 temperature of the column ~0 to 25°C, and passing gases equilibrated at 25°C and 1000°C  
438 through the column. No fractionation of the equilibrated gases occurred during the room  
439 temperature trials. The transfer of CO<sub>2</sub> through the column at room temperature was monitored  
440 barometrically, and freezing over of CO<sub>2</sub> was continued for approximately 10 minutes beyond  
441 the time required for the upstream pressure to reach baseline (40-45 minutes total). The collected  
442 CO<sub>2</sub> was cryogenically transferred through a second water trap to a cold finger, then isolated and  
443 warmed for pressure reading to confirm quantitative transfer. The purified CO<sub>2</sub> was stored in  
444 borosilcate tubes with CTFE valve body and o-ring seal (Kimble-Chase, Vineland, NJ) until  
445 loaded into the mass spectrometer sample bellows.

446 Clumped isotope measurements and traditional carbon and oxygen stable isotope  
447 measurements were made on a Finnigan MAT253 set to measure m/z 44-49 ion beams. We

448 employed the run structure and pressure baseline correction detailed in He et al. (2012). Oztech  
449 (Safford, AZ, USA) isotopic standard CO<sub>2</sub> tank gas (UOC 1766,  $\delta^{13}\text{C}=-3.61\text{‰}$  VPDB,  
450  $\delta^{18}\text{O}=24.99\text{‰}$  VSMOW) was used as the working reference gas during clumped isotope  
451 analyses, and  $\delta_{47}$  values were determined with the working gas defining zero.

452       Following Dennis et al. (2011), raw  $\Delta_{47}$  values are standardized to gases heated to  
453 1000°C to approximate near random distribution of isotopes, as well as gases equilibrated with  
454 waters of known composition at 4, 26, and 60°C. Standardized  $\Delta_{47}$  values are reported on an  
455 “absolute reference frame”, henceforth referred to as the Carbon Dioxide Equilibrium Scale  
456 (CDES) following Dennis et al. (2011) and allowing for interlaboratory comparison. We  
457 routinely measured standard calcite materials (Carrera Marble [CM] and four CaCO<sub>3</sub> materials  
458 from ETH-Zurich [ETH1 through 4]), which are analyzed at regular intervals in many clumped  
459 isotope facilities for the purpose of inter-laboratory calibrations and measurement comparisons.  
460 We also use frequent analyses of these standard materials as a check on internal consistency of  
461 repeated measurements within and between analytical periods (Table A1 and A2). Further  
462 discussion of quality control checks and corrections applied to measurements made on the  
463 MAT253 can be found in the Appendix.

464       Temperatures were calculated using the Zaarur et al. (2013) paleothermometer. There is  
465 presently a consensus in the clumped isotope research community that the conversion of  $\Delta_{47}$   
466 values to equilibrium temperatures should employ a paleothermometer that was determined on  
467 similar sample types and with similar acid digestion temperatures (Huntington et al., 2015;  
468 Defliese et al., 2015; Gallagher and Sheldon, 2016; Burgener et al., 2016; Ringham et al.,  
469 2016). Our 26°C acid digestion temperatures is essentially the same as the 25°C temperature  
470 used for the Zaarur et al. (2013) calibration. Use of this paleothermometer also maintains inter-

471 laboratory consistency with other paleoaltimetry studies on the Tibetan Plateau (Huntington et  
472 al., 2015). Errors are reported for each sample using the standard error of the mean for replicate  
473 sample digestions (in this study,  $\Delta_{47}$  s.e.m. of 0.011 to 0.040), that converts to temperature  
474 uncertainties of 2.3 to 8.2°C on the Zaarur et al. (2013) paleothermometer.

475

#### 476 **$^{40}\text{Ar}/^{39}\text{Ar}$ geochronology**

477 Standard K-feldspar  $^{40}\text{Ar}/^{39}\text{Ar}$  total fusion analyses were conducted for sample W0628-4  
478 in the Lehigh University Noble Gas Laboratory (Table 4). Approximately 2.4 mg of K-feldspar  
479 was loaded into an aluminum foil packet and stacked vertically with other unknowns along with  
480 GA1550 biotite flux monitor (age = 98.79 Ma) and  $\text{K}_2\text{SO}_4$  and  $\text{CaF}_2$  salts to correct for  
481 nucleogenic interferences. Following a cumulative 25-hour irradiation at the USGS Triga  
482 reactor, K-feldspars were split into three aliquots, loaded into a sample planchet and brought to  
483 vacuum by a turbomolecular pump coupled with a rotary backing pump. Samples were fused  
484 using a Merchantek dual UV/ $\text{CO}_2$  laser system. Extracted gas was purified with an SAES getter  
485 for 10 minutes. The gas was then measured by an Argus VI magnetic sector mass spectrometer  
486 equipped with five faraday cups. Masses 40, 39, 38, 37, and 36 were measured concurrently to  
487 enable calculation of the radiogenic  $^{40}\text{Ar}$  component and correct for nucleogenic interferences  
488 ( $^{40}\text{Ca}$ ,  $^{42}\text{Ca}$ ,  $^{37}\text{Cl}$ ,  $^{40}\text{K}$ ) on Ar isotopes. Raw data was reduced using ArArCalc software (Koppers,  
489 2002) to regress to time-zero beams and to correct for blank, mass discrimination, nucleogenic  
490 interferences, and decay following irradiation. Data for the three aliquots in the inverse isochron  
491 plot show a well-fit linear correlation with a  $^{40}\text{Ar}/^{36}\text{Ar}$  intercept indicative of a trapped excess Ar  
492 component (Fig. A1).

493

494 **Apatite (U-Th)/He thermochronometry**

495 Measurements for apatite (U-Th)/He thermochronometry were made in the Noble Gas  
496 Thermochronometry Laboratory at the Berkeley Geochronology Center. A brief description of  
497 the methodology is provided here; for a full description of the measurement procedures, see  
498 Tremblay et al. (2015).

499 Individual, euhedral apatite crystals with no visible fluid or mineral inclusions and  
500 equivalent spherical radii of 50  $\mu\text{m}$  or greater were selected, photographed, and measured using a  
501 Leica MZ16 stereomicroscope. Individual crystals were loaded into PtIr packets and heated  
502 under vacuum to  $1050 \pm 50$   $^{\circ}\text{C}$  for 6 minutes with an 810 nm wavelength diode laser. The  
503 extracted gas was spiked with an aliquot of  $^3\text{He}$ , purified, and analyzed using a Pfeiffer Prisma  
504 quadrupole mass spectrometer QMS 200 under static vacuum. Helium blanks, determined by  
505 heating empty PtIr packets, were typically less than  $5 \times 10^{-17}$  moles. To achieve complete helium  
506 extraction, each sample was reheated until the  $^4\text{He}$  yield was less than 0.5% of the  $^4\text{He}$  yield in  
507 the first heating step. Molar  $^4\text{He}$  abundances were calculated by dividing the measured  $^4\text{He}/^3\text{He}$   
508 ratio by the  $^4\text{He}/^3\text{He}$  ratio of a manometrically-calibrated  $^4\text{He}$  standard gas aliquot spiked with  
509 the same molar abundance of  $^3\text{He}$  as was the unknown, and multiplying this value by the  
510 standard gas's known  $^4\text{He}$  molar abundance.

511 After degassing, each sample was dissolved in 50 $\mu\text{L}$  of 7N  $\text{HNO}_3$  spike solution  
512 containing  $9.20 \times 10^{-10}$  mol/L  $^{233}\text{U}$ ,  $9.03 \times 10^{-10}$  mol/L  $^{229}\text{Th}$ , and 6.7% enriched  $^{147}\text{Sm}$  spike.  
513 Solutions were diluted by a factor of 20 and analyzed on a Thermo Scientific Neptune Plus  
514 multicollector ICP-MS with an Aridus2 desolvating nebulizer sample introduction system. To  
515 standardize the analyses, we also analyzed a spiked normal solution with known U, Th, and Sm  
516 concentrations. Spiked normal solution isotope ratio measurements were reproducible to much

517 better than 0.5% for each element. (U-Th)/He ages were calculated using blank corrected  
518  $^4\text{He}$ ,  $^{147}\text{Sm}$ ,  $^{232}\text{Th}$ , and  $^{238}\text{U}$  abundances. Raw ages were corrected for alpha ejection effects after  
519 Farley et al. (1996).

520

## 521 **DISCUSSION OF RESULTS**

### 522 **Geochronology and thermochronometry**

523 A rhyolite immediately above the Rigongla-Nianbo unconformity provides an  $^{40}\text{Ar}/^{39}\text{Ar}$   
524 K-feldspar age of  $28.90\pm 1.52$  Ma (Fig. A1), providing a minimum age of the underlying Nianbo  
525 Formation. A three-point regression in the inverse isochron is not ideal for these data and  
526 xenocrystic contamination cannot be ruled out in the Rigongla rhyolite. However, if this were the  
527 case, producing a well-defined regression line with reasonable trapped  $^{36}\text{Ar}/^{40}\text{Ar}$  intercept would  
528 require fortuitous trade-offs between each aliquot's age, trapped  $^{36}\text{Ar}/^{40}\text{Ar}$ , and trapped to  
529 radiogenic Ar ratio, and therefore is not likely. The inverse isochron age of  $28.9\pm 1.52$  Ma that  
530 we report is consistent with a K/Ar age of  $\sim 31$  Ma from the lower Rigongla formation elsewhere  
531 in the basin (Zhu et al., 2006) which lends additional confidence to our interpretation.

532 Apatite grains from two samples of Qianggeren granite (L0706-2 and L0706-3) from a  
533 quarry  $\sim 4$  km north of the Pana Formation in Penbo Basin yielded (U-Th)/He ages of  $14.86\pm 1.83$   
534 Ma and  $12.74\pm 1.47$  Ma ( $1\sigma$ ; Table 4), respectively. The Qianggeren granite sits in the hanging  
535 wall of the Gulu thrust. L0706-2 and L0706-3 are located  $< 1-2$  km from a reported zircon U/Pb  
536 age of  $51.9\pm 2.5$  Ma within the Qianggeren granite (He et al., 2007).

537

### 538 **$\delta^{13}\text{C}$ , $\delta^{18}\text{O}$ and clumped isotope-derived temperatures**

#### 539 ***Penbo Basin***



540           The oxygen isotopic compositions of all 68 calcites sampled from the Pana and Nianbo  
541 Formations in the Penbo basin range from  $\delta^{18}\text{O}$  of  $-22.8$  to  $-9.4\pm 0.1\text{‰}$ , with mean values of  $-$   
542  $14.0\pm 1.2\text{‰}$  and  $-15.1\pm 2.1\text{‰}$  ( $1\sigma$ ), respectively (Table 1). The carbon isotopic compositions  
543 range from  $\delta^{13}\text{C}$  of  $-10.4$  to  $-0.1\text{‰}$ . The mean  $\delta^{13}\text{C}_{\text{cc}}$  for all calcites of the Pana and Nianbo  
544 Formations vary by  $1.5\text{‰}$ , with values of  $-6.0\pm 1.5\text{‰}$  and  $-4.5\pm 2.3\text{‰}$  ( $1\sigma$ ), respectively.  
545 Pedogenic and lacustrine carbonate typically derive their carbon from different sources and  
546 precipitate under different environmental conditions, thus providing additional information for  
547 environmental reconstructions. As such, it is worth noting isotopic variability between modes of  
548 carbonate genesis. The mean  $\delta^{13}\text{C}_{\text{cc}}$  values for paleosol carbonate in the Paleocene-Eocene Pana  
549 and Nianbo Formations are  $-6.9\pm 0.8\text{‰}$  and  $-5.4\pm 2.2\text{‰}$ , respectively. The mean  $\delta^{13}\text{C}_{\text{cc}}$  values for  
550 lacustrine carbonate are  $-5.7\pm 1.8\text{‰}$  and  $-3.2\pm 1.7\text{‰}$ .

551           In the subset of samples with clumped isotope measurements and petrographic  
552 characterization, both the “primary” carbonates and those with more extensive signs of  
553 recrystallization span  $-12$  to  $-18\text{‰}$  in  $\delta^{18}\text{O}_{\text{c}}$  space. The three primary carbonates from the Nianbo  
554 Formation record  $\Delta_{47,\text{CDES}}$  values of  $0.700\text{-}0.730\pm 0.020$  (Table 3). These carbonates yield  $T(\Delta_{47})$   
555 of  $6$  to  $12\text{ °C}$  (Fig. 5A). As described in the Methods section (Sample Preparation), we interpret  
556 these as “primary” carbonate reflecting original depositional temperature. Four pedogenic and  
557 lacustrine carbonates exhibit more extensive recrystallization in thin section. These altered  
558 carbonates have  $\Delta_{47,\text{CDES}}$  values of  $0.540\text{-}0.590\pm 0.010$  with corresponding paleo-temperatures  
559 from  $41$  to  $55\text{ °C}$ . The upper end of this temperature range is similar to those determined from  
560 visual Thermal Alteration Index values for organics sampled from the base of the Penbo section.  
561 These values correspond to vitrinite reflectance values ( $R_0$ ) of  $0.4\%$  to  $0.5\%$ , indicating burial  
562 temperatures ranging from  $53\text{ °}$  to  $75\text{ °C}$  (Barker, 1988).

563 The observed variability in both  $\delta^{18}\text{O}_c$  and  $\Delta_{47}$  does not display any stratigraphic trend  
564 that can be attributed to progressive burial diagenesis with depth (Fig. 6). The samples that show  
565 petrographic and  $\Delta_{47}$  signs of alteration are not appreciably shifted in  $\delta^{18}\text{O}_c$ , implying that the  
566 alteration in these samples was rock-buffered, i.e. carbonate buffered the oxygen isotopic  
567 composition relative to the small amount of water present in the system. We emphasize paleo-  
568 elevations derived from samples with  $\Delta_{47}$  analyses (Table 3), but include data from all samples  
569 (measured  $\delta^{18}\text{O}_c$  only) under the assumption that any alteration took place in a rock-buffered  
570 system. The remainder of the discussion of the Penbo basin samples will focus on the  
571 implications of the isotopic compositions of the minimally altered, micritic carbonates.

## 572 *Oiyug Basin*

573 Traditional oxygen and carbon isotopic variations were assessed for trends with location  
574 in section (relative age) and sediment type (Table 2). Oxygen analyses of siderites and dolomites  
575 from the Oiyug basin yield different values from the dominant calcite mineralogy. For example,  
576 calcites from the Oiyug Formation (~8.1 to 2.5 Ma; Chen et al., 2008) yield  $\delta^{18}\text{O}_c$  and  $\delta^{13}\text{C}$   
577 values of -28.0 to  $-27.4 \pm 0.1\text{‰}$  and -0.1 to  $1.3\text{‰}$  (VPDB), and the siderite nodule,  $-10.8\text{‰}$  and  
578  $12.9\text{‰}$ . As such, siderites and dolomites are considered separately.

579 Calcites from the Gazhacun Group (>15.03 Ma; Spicer et al., 2003) yield mean  $\delta^{18}\text{O}_{cc}$   
580 and  $\delta^{13}\text{C}_{cc}$  values of  $-18.8 \pm 2.6\text{‰}$  (ranging -21.1 to  $-11.6\text{‰}$ ) and  $-6.3 \pm 1.6\text{‰}$  (ranging -8.0 to -  
581  $2.5\text{‰}$ ). Dolomites from the Gazhacun Group yield mean  $\delta^{18}\text{O}_{\text{MgCO}_3}$  and  $\delta^{13}\text{C}_{\text{MgCO}_3}$  values of -  
582  $6.9 \pm 2.3\text{‰}$  (ranging -11.3 to  $-5.5\text{‰}$ ) and  $-6.8 \pm 2.4\text{‰}$  (ranging -11.3 to  $-5.1\text{‰}$ ). One lacustrine  
583 siderite from the top of the Gazhacun Group yields  $\delta^{18}\text{O}_{\text{FeCO}_3}$  and  $\delta^{13}\text{C}_{\text{FeCO}_3}$  values of  $-17.1\text{‰}$  and  
584  $4.2\text{‰}$ , respectively. The mean  $\delta^{18}\text{O}_c$  and  $\delta^{13}\text{C}_{cc}$  values of calcite in the Rigongla Formation (31.4-  
585 15.1 Ma (Zhu et al., 2006)) are  $-16.4 \pm 4.0\text{‰}$  (ranging -20.4 to  $-11.9\text{‰}$ ) and  $-3.9 \pm 1.4\text{‰}$  (ranging -

586 6.2 to -2.6‰). Calcites from the Nianbo Formation (63.8 to 50.2 Ma; Wang et al., 2014) yield  
587 slightly lower  $\delta^{18}\text{O}_c$  of -24.9 to  $-18.6 \pm 0.1$ ‰. The mean  $\delta^{13}\text{C}_{cc}$  value of the Nianbo Formation is -  
588  $3.0 \pm 1.4$ ‰, which agrees within error with the carbon isotope values of the Nianbo Formation in  
589 the Penbo basin.

590 Eight of the pedogenic, groundwater, and lacustrine calcites yield  $\Delta_{47, \text{CDES}}$  measurements  
591 ranging from 0.625 to 0.755 (Table 3). These values correlate to temperatures that range from  
592  $\sim 30^\circ\text{C}$  to  $1^\circ\text{C}$  (Fig. 5B), which are in the realm of plausible low-latitude, high-elevation surface  
593 temperatures (Lawrimore et al., 2011).

594 A vein calcite (543Av) from the Lower Gazhacun Formation yields a low  $\Delta_{47}$  value of  
595  $0.467 \pm 0.014$  and corresponding higher temperature of  $83.3 \pm 6.0^\circ\text{C}$  ( $\pm$ s.e.m.,  $n=2$ ). This vein was  
596 sub-sampled from pedogenic calcite 543A, which yielded a  $\Delta_{47}$  value of  $0.625 \pm 0.010$  and paleo-  
597 temperature of  $30.1 \pm 2.6^\circ\text{C}$  ( $\pm$ s.e.m.,  $n=4$ ). Even if this pedogenic calcite precipitated at the  
598 warmest part of the day during the warmest month of the year,  $30^\circ\text{C}$  is likely warm for  $>4$  km  
599 elevation. There are at least two plausible scenarios that would result in a soil carbonate  $T(\Delta_{47})$   
600 greater than mean air temperature:

601 (1) Pedogenic  $T(\Delta_{47})$ , on average, exceeds mean summer air temperature by  $3$ - $5^\circ\text{C}$  (Hough et  
602 al., 2014), and mean annual air temperature by  $10$ - $15^\circ\text{C}$  due to summertime bias in soil carbonate  
603 formation (Quade et al., 2013) and increased solar heating of the soil surface (Passey et al.,  
604 2010). Applying the latter offset, the air temperature above the location of soil carbonate  
605 formation would be  $15$ - $20^\circ\text{C}$ . While seasonality may have the dominant effect on soil carbonate  
606  $\Delta_{47}$  (Passey et al., 2010; Suarez et al., 2011; Peters et al., 2013; Quade et al., 2013; Hough et al.,  
607 2014),  $\Delta_{47}$  also varies with soil depth and duration of shade cover (Quade et al., 2013), soil  
608 moisture as it relates to the timing of carbonate formation (Burgener et al., 2016), and local soil

609 hydrology (Ringham et al., 2016). This is to say, at the same elevation and atmospheric  
610 temperature, but under variable environmental conditions, two pedogenic calcites could record  
611 significantly different  $\Delta_{47}$  values. For example, the two pedogenic calcites most proximal to  
612 543A, within the Gazhacun Formation and 40m below in the Rigongla Formation, yield T( $\Delta_{47}$ )  
613 values of  $7.6 \pm 3.3^\circ\text{C}$  and  $9.8 \pm 4.3^\circ\text{C}$ , respectively. Therefore, it is reasonable to believe that the  
614 air temperature above soil carbonate 543A was much cooler than  $30^\circ\text{C}$ .

615 (2) The bulk rock could have experienced low-grade alteration and partial recrystallization  
616 under higher temperature associated with the calcite vein (543Av). Even so, there are significant  
617 differences between  $\delta^{18}\text{O}_c$  and  $\Delta_{47}$  of 543A and 543Av, suggesting that the alteration was not  
618 pervasive enough to cause extensive bond reordering or bulk isotopic resetting of the whole rock.

619 Marl calcite W0628-2 of the Nianbo Formation is also interpreted as diagenetically  
620 altered based on a  $\Delta_{47}$  value of  $0.572 \pm 0.027$  ( $\pm$ s.e.m.,  $n=3$ ) and corresponding paleo-temperature  
621 of  $45.7 \pm 8.3^\circ\text{C}$ . However, the other two samples from the Nianbo Formation yield paleo-  
622 temperatures of  $0.7 \pm 2.3^\circ\text{C}$  ( $n=6$ ) and  $5.3 \pm 8.2^\circ\text{C}$  ( $n=3$ ) (Table 3; Fig. 5B). Further, W0628-2  
623 and W0628-3 are identical in  $\delta^{18}\text{O}_w$  within uncertainty regardless of the high apparent T( $\Delta_{47}$ )  
624 retained by W0628-2. This suggests that the isotopic composition of the Nianbo Formation in the  
625 Oiyug Basin also reflects a rock-buffered system. As such, samples collected from this section  
626 likely maintain oxygen isotopic fidelity even under higher diagenetic temperatures.

627

### 628 ***Multi-proxy assessment of diagenesis and maximum carbonate temperatures***

629 At sufficiently high temperature, solid-state bond reordering can occur in the carbonate  
630 lattice without the aid of water. Carbonate that experiences temperatures  $>100^\circ\text{C}$  for  $10^6$ - $10^8$   
631 years is subject to reordering of  $^{13}\text{C}$ - $^{18}\text{O}$  bonds to a more stochastic distribution, or a lower  $\Delta_{47}$

632 (Henkes et al., 2014). A high degree of  $^{13}\text{C}$ - $^{18}\text{O}$  clumping preserved in the carbonate lattice is  
633 thought to be diagnostic of primary carbonate because no known mechanisms are currently  
634 described to alter a carbonate to a higher  $\Delta_{47}$  value. However, recent measurements of latest  
635 Paleocene marine carbonates (Jialazi Fm) buried to at least 150-180°C (Orme, 2015) strongly  
636 suggest that  $^{13}\text{C}$ - $^{18}\text{O}$  bonds in the carbonate lattice can increase in relative abundance (increasing  
637  $\Delta_{47}$ ) during burial-exhumation-related alteration (Ingalls, 2017). The mechanism by which bond  
638 ordering can increase during alteration has yet to be adequately modeled and attributed to a  
639 geological process during burial and exhumation. Therefore, it is exceedingly important to  
640 provide multiple assessments of alteration and isotopic resetting/reordering when interpreting  
641 clumped isotope and traditional stable isotope data, and heed caution in interpreting high  $\Delta_{47}$   
642 measurements.

643         The detection of diagenetic alteration and isotopic resetting requires careful  
644 characterization of carbonate mineralogy, inspection for recrystallization and alteration textures  
645 using petrography and microscopy, and sub-sampling of  $\delta^{18}\text{O}_c$  of clasts, veins and matrix  
646 material (DeCelles et al., 2007; Saylor et al., 2009) to detect possible diagenesis and isotopic  
647 resetting. Unfortunately, micron-scale recrystallization in the matrix and on mineral edges may  
648 go unnoticed using only these techniques (Garzzone et al., 2004; Leier et al., 2009). We therefore  
649 complement petrographic observations with further geochemical analyses to constrain thermal  
650 history and therefore the potential for solid-state alteration.

651         The Oiyug and Penbo basins are structurally complex, with major thrust faults (i.e. Gulu,  
652 Puxiabaga, and Lega thrusts; He et al., 2007) that place Mesozoic strata structurally above our  
653 Paleocene-Eocene sections. Here, we carefully consider the thermal conditions experienced by  
654 Linzizong carbonates in order to assess the significance of our stable isotope paleoaltimetry and

655 carbonate clumped-isotope results in the Oiyug and Penbo basins. Constraints on the timing of  
656 Gulu thrust activation and consequent burial of the Paleocene-Eocene Linzizong strata in the  
657 Penbo basin are limited to K-feldspar  $^{40}\text{Ar}/^{39}\text{Ar}$  (He et al., 2007) and apatite (U-Th)/He  
658 thermochronometry (AHe) of the Qianggeren granite ~3 km north of Penbo basin (Fig. 1). These  
659 data suggest activation of the Gulu thrust occurred after the youngest Pana Formation  
660 sedimentation (~47 Ma), and prior to the exhumation of the Qianggeren granite to ~70°C (<3 km  
661 depth) ~12-15 Ma (AHe). The AHe ages closely match others to the east (Tremblay et al., 2015)  
662 and in the greater Lhasa region (Rohrmann et al., 2012), which are thought to reflect a period of  
663 regional exhumation of the southeastern Lhasa terrane. It is likely that the Paleocene-Eocene  
664 Linzizong strata exhumed to <3 km depth (cooler than threshold temperature for solid-state  
665 reordering) as well during this regional exhumation event. Regional exhumation at ~12-15 Ma  
666 places a critical bound on Linzizong burial duration.

667         It is possible that the AHe ages presented here represent rock uplift associated with  
668 thrust exhumation, but multi-diffusion domain modeling of K-feldspar from the Qianggeren  
669 granite yields a thermal history indicating rapid cooling from ~325°C to <150°C between ~42  
670 and 39 Ma (He et al., 2007). We suggest that the rapid exhumation of the Qianggeren granite in  
671 the hanging wall of the Gulu thrust records the initiation of thrusting, and thus places a  
672 maximum bound on the timing of burial of the Linzizong strata.

673         To determine the maximum burial temperature experienced by the Linzizong sediments,  
674 we must consider contributions to the thickness of rock overburden. The absence of strata  
675 younger than the Pana Fm in the Penbo basin and the absence of the Pana Fm at the Nianbo-  
676 Rigongla unconformity in the Oiyug basin could both be tied to regional upper crustal shortening  
677 (Rohrmann et al., 2012) and possibly Gulu thrust activation. It is possible that the Oligocene to

678 Miocene strata overlying the Linzizong Group never existed in the Penbo basin. If so, the  
679 Paleocene-Eocene Linzizong strata would have experienced thrust burial with a total overburden  
680 thickness equal to the structural thickness of the already deformed Jurassic-Triassic units. The  
681 Jurassic-Triassic units have an outcrop width of about 3 km north of Penbo basin. The hanging  
682 wall of the next north structural panel contains the Qianggeren pluton intrusive into Linzizong  
683 strata that unconformably overlie mapped Carboniferous units (NGAC map “H45C002003,”  
684 2002). Interestingly, a Paleocene-Eocene E<sub>1</sub> granitoid intrudes across the Gulu thrust about 22.5  
685 km farther east (29.9634°N, 91.4221°E; NGAC map “H46C003001,” 2012), implying most  
686 Gulu-associated deformation might be related to widespread pre-Linzizong deformation of the  
687 Shexing and older units below the Maqu unconformity. Reactivation of at least a segment of the  
688 Gulu Thrust post-Pana is clear, but may not be associated with significant overthrusting of the  
689 Penbo Basin. The multiple episodes of shortening, both pre-Linzizong and post preclude detailed  
690 structural reconstruction of the tectonic burial history of this region.

691       Organic geochemical proxies, however, support a cooler thermal history for the  
692 Linzizong strata. Vitrinite reflectance from a Nianbo Formation shale (645A) in the Penbo basin  
693 suggests these strata reached temperatures in excess of 110°C. Preliminary methylphenanthrenes  
694 (biomarkers) derived from this shale yield equivalent vitrinite reflectance values of 1.4±0.4%,  
695 suggesting that these strata reached temperatures in excess of 135°C at some point in their burial  
696 history, but not significantly greater based on the lack of typical petroleum biomarkers (i.e.  
697 sterane and hopane) and long-chain n-alkanes indicative of deep burial. Assuming a very  
698 conservative 25°C/km geothermal gradient for this arc-region these temperatures suggest no  
699 more than 6 km of total post-Nianbo burial by Pana and structurally emplaced overburden.

700 Using the kinetic parameters of Henkes et al. (2014), we can model the amount of solid-  
701 state reordering of C-O bonds within the calcite lattice that would occur under hypothetical time-  
702 temperature histories. Burial of the Nianbo strata by Pana plus thrust emplacement of Mesozoic  
703 rocks could contribute up to 6km of overburden. Given the loose constraints on thrust activation  
704 and duration of burial, we model the Paleocene-Eocene strata burial to <150°C (~6 km burial  
705 upon Gulu thrust activation) at ~42 to 39 Ma based on K-feldspar multi-diffusion domain  
706 modeling (He et al., 2007), followed by rapid regional exhumation to below 70°C at ~12 Ma  
707 (AHe, this study). Although rapid exhumation is not required by the AHe data, this scenario  
708 represents the longest possible burial duration consistent with the thermochronometric  
709 constraints. Under this scenario, we expect a  $\Delta_{47}$  value of ~0.590, or  $T(\Delta_{47})$  of 65°C. None of the  
710 carbonates from the Penbo basin yield  $\Delta_{47}$  values as low as this scenario, or temperatures as high.

711 Thus, the  $T(\Delta_{47})$  measurements of Nianbo Formation within the Penbo basin do not  
712 appear to reflect solid-state reordering and are interpreted to record primary isotopic  
713 compositions or early recrystallization temperatures during water-rock alteration at shallow  
714 depths. There could be minimal reordering at the lower bound temperatures from the organic  
715 thermal maturation estimates, perhaps boosting  $T(\Delta_{47})$  estimates on the order of 10°C (Stolper  
716 and Eiler, 2015). If primary temperatures were cooler than those we estimate directly, then this  
717 would result in higher paleoaltimetry estimates. We do not make any correction for this potential  
718 slight reordering, thus our altimetric estimates remain conservative. More importantly, the C-O  
719 bonds of Nianbo Fm carbonate yielding “low”  $T(\Delta_{47})$  measurements appear to be robust to  
720 elevated burial temperature no matter the precise time-temperature history of the Gulu thrust, and  
721 are interpreted to record primary mineral formation temperatures from the Paleocene to Eocene.



722 These samples provide apparent evidence for the survival of primary clumped isotope values  
723 even in the face of substantial burial and heating.

724

725 *Testing the predictive capability of petrographic observations in assessing carbonate*

726 *diagenesis*

727 A subset of nodular, groundwater, lacustrine marl, pedogenic, and vein calcite samples  
728 from Penbo and Oiyug were selected for  $\Delta_{47}$  analyses based on sedimentary and petrographic  
729 textures seen in thin section (Tables 5 and 6) in order to (1) sufficiently sample primary isotopic  
730 compositions to derive paleo-temperatures of each time slice throughout the Cenozoic, and (2)  
731 provide a comparison between microscopic assessment of primary carbonate textures and direct  
732 measurements of  $T(\Delta_{47})$ . This enabled a check on our ability to correctly assess diagenetic  
733 alteration in thin section. Based on visual observations in petrographic section, each sample was  
734 binned as “primary” (lacking evidence of recrystallization), “minor alteration” (heterogeneous,  
735 macroscopic and could be potentially avoided by careful sample drilling), or “diagenetic”  
736 (extensive recrystallization present).

737 Temperatures derived from clumped isotope measurements generally corresponded with  
738 the petrographic interpretations for six of the seven Oiyug basin samples. One sample, W0628-3  
739 from the Nianbo Formation, was predicted to be diagenetic and yield a high  $T(\Delta_{47})$  (low  $\Delta_{47}$ )  
740 because of extensive cross-cutting of secondary calcite veins. Contrary to this assessment,  
741 triplicate measurements of micrite from this sample yielded a  $T(\Delta_{47})$  of  $5.3 \pm 8.2^\circ\text{C}$  (s.e.m.). This  
742 combination of petrographic observation and isotopic measurement suggests two possible  
743 interactions: (1) alteration occurred very early in the rock’s history while the rock was at high  
744 elevation prior to burial, so the altered carbonate still yields a cool signal, or (2) most of the

745 sample mass is unaltered micrite. In the second scenario, even if the calcitic veins experienced  
746 warm temperatures, they do not significantly shift the bulk  $\Delta_{47}$  values. Thermochronometric data,  
747 petrography, and the  $\Delta_{47}$ -derived temperatures ( $T(\Delta_{47})$ ) are in agreement that sediments and  
748 paleosols from the Oiyug and Penbo basins have not reached high enough burial temperatures  
749 that would likely alter the original  $\Delta_{47}$  composition of carbonates via solid-state alteration.  
750 Therefore, we consider our low  $T(\Delta_{47})$  carbonates from both sedimentary basins to represent  
751 primary depositional conditions throughout the Cenozoic.

752

### 753 **Paleocene to Pliocene stable isotope paleoaltimetry of the Lhasa Terrane**

#### 754 ***Penbo Basin***

755 All clumped isotope samples from the Penbo Basin are derived from the Nianbo  
756 Formation. As such, we use the average of the three  $\Delta_{47}$ -derived “primary” paleo-temperatures  
757 ( $8.9 \pm 5.0$  °C) coupled with measured  $\delta^{18}\text{O}_c$  to calculate the isotopic composition of the water  
758 with which calcite equilibrated (Kim and O’Neil, 1997). Paleo-water  $\delta^{18}\text{O}_w$  values of the Nianbo  
759 Formation (ranging -11.8‰ to -22.6‰ VSMOW) are used to estimate elevation ( $\Delta(\delta^{18}\text{O}_p)$ ). We  
760 report both individual elevation estimates and the mean elevation of each dominant lithology  
761 within a geologic formation (Table 1; Fig. 6).

762 The best estimate of the paleo-elevation of the Nianbo Formation preserved in the Penbo  
763 basin is  $4.4^{+1.3}_{-1.7}$  km, comparable to modern elevation of this basin (Table 1; Fig. 6). We view  
764 this estimate to be conservative because we employ the modern isotopic lapse rate, which is  
765 likely significantly steeper than the true lapse rate in the Early Eocene (Rowley, 2007; Rowley  
766 and Garzzone, 2007). Further, the Siwalik value for low-latitude ( $\sim 19.6 \pm 3.9^\circ\text{N}$ ) (Quade et al.,  
767 1989), low elevation precipitation likely has lower  $\delta^{18}\text{O}$  than actual precipitation in the source

768 region for moisture advecting to higher altitudes during the considerably warmer Early Eocene.  
769 The use of an isotopically more negative low elevation precipitation source contributes to  
770 making our paleo-elevation calculations conservative, i.e., underestimates the true elevation.

771 We apply the mean  $T(\Delta_{47})$  derived from the underlying Nianbo Formation to calculate  
772  $\delta^{18}\text{O}_w$  of the overlying upper Pana Formation sediments. This succession yields paleo-surface  
773 water isotopic compositions of -16.9‰ to -13.4‰ VSMOW. These paleo-precipitation values  
774 correspond with an estimated paleo-elevation of the Pana Formation of  $4.1^{+1.2}/_{-1.6}$  km, identical  
775 to the underlying Nianbo Formation within error.

776

### 777 ***Oiyug Basin***

778 The Nianbo, Rigongla, and Lower Gazhacun Formations are dominated by a common  
779 lithology (pedogenic calcite), which allows for a straightforward characterization of the  
780 Paleocene to Miocene elevation history (Table 2). For samples with clumped isotope  
781 measurements, the sample-specific  $T(\Delta_{47})$  was applied to calculate carbonate-water isotopic  
782 fractionation. An average  $T(\Delta_{47})$  for each geologic formation was applied for samples on which  
783 only  $\delta^{18}\text{O}_c$  was measured. Employing  $T(\Delta_{47})$  values of  $3.0 \pm 8.2^\circ\text{C}$  for the Nianbo Formation,  
784  $9.8 \pm 4.3^\circ\text{C}$  for the Rigongla Formation, and  $18.9 \pm 8.2^\circ\text{C}$  for the Lower Gazhacun member, we  
785 calculate  $\Delta(\delta^{18}\text{O}_p)$  of  $-18.5 \pm 3.1\%$ ,  $-10.7 \pm 3.5\%$ , and  $-13.8 \pm 1.9\%$  VSMOW ( $1\sigma$ ), respectively.  
786 Taking the average ( $\pm 2\sigma$  model and analytical error) of all carbonates within, these formations  
787 yield mean elevation estimates of  $5.6^{+1.5}/_{-2.1}$  km,  $4.1^{+1.3}/_{-1.6}$  km, and  $4.5^{+1.5}/_{-1.7}$  km, respectively.  
788 The elevation estimate for the Paleocene-Eocene Nianbo Fm suggests that the Oiyug region was  
789 0.5-1.5 km higher at the onset of India-Asia collision than it is today.

790 Early and Middle Miocene Gazhacun carbonate oxygen compositions span a broad range  
791 -5.5 to -21.1‰VPDB. All marl and lacustrine calcite, mudstones, and dolomite deposited in the  
792 middle member of the Gazhacun Group are <sup>18</sup>O-enriched relative to other units. The higher δ<sup>18</sup>O<sub>c</sub>  
793 values in the middle Gazhacun member are interpreted as the result of evaporative enrichment  
794 because pedogenic calcites from stratigraphically proximal horizons yield low T(Δ<sub>47</sub>) values of  
795 3.9 to 19.7°C with low δ<sup>18</sup>O values.

796 Evaporative enrichment is not clearly evident in lacustrine calcite and siderite in the older  
797 Nianbo Formation or the younger Oiyug Formation. The mean elevation derived from the two  
798 calcite clumped isotope samples in the Oiyug Formation is 6.5<sup>+1.8</sup>/<sub>-2.3</sub> km using an average  
799 Δδ<sup>18</sup>O<sub>p</sub> of -24.2±1.5‰ (Table 2). As a comparison, the elevation estimate of siderite nodule  
800 618A from the upper Gazhacun is 4.4<sup>+1.3</sup>/<sub>-1.8</sub> km (Δ(δ<sup>18</sup>O<sub>p</sub>) of -11.7‰). We accept the elevations  
801 provided by the calcites in the Gazhacun and Oiyug Fms because of the preservation of primary  
802 Δ<sub>47</sub> values (Fig. 5B) and the evaporative trend demonstrated by plotting δ<sup>18</sup>O of the two siderite  
803 samples relative to δD<sub>leaf wax</sub> and δ<sup>18</sup>O<sub>calcite</sub> from the same sedimentary horizon (see discussion  
804 and Fig. A2).

805

### 806 *Comparing Isotopic and Temperature Lapse Rates*

807 There can be a correlation between degree of depletion of oxygen in meteoric water and  
808 formation temperature as both are controlled by atmospheric lapse rates. Estimates of tropical sea  
809 surface temperature for times bracketing the age of the Nianbo Formation imply T>30°C  
810 (Pearson et al., 2001) and thus a temperature gradient from sea level to the Penbo Basin of ≥  
811 20±5°C. Using a typical 6°C/km atmospheric lapse rate implies elevations in excess of 3 km.  
812 Ground surface temperatures are typically warmer than the atmosphere at the same height, and

813 pedogenic and lake carbonates appear to record this with a summer seasonal bias (Huntington et  
814 al., 2010). Thus our paleo-temperatures are also consistent with an elevation of ~4 km.

815

## 816 **HIGH ELEVATION SOUTHERN MARGIN OF EURASIA**

817 Using  $T(\Delta_{47})$  and  $\delta^{18}\text{O}$  of pedogenic and lacustrine carbonates from the Paleocene-  
818 Eocene Nianbo Formation, we are able to advance the elevation record of the southern Lhasa  
819 block an additional ~20 My compared with the oldest prior records (Currie et al., 2016). Our  
820 oldest paleo-elevations support a pre-existing 'high' topography on the southern margin of  
821 Eurasia prior to the onset of India-Asia collision (Ding et al., 2014), with elevations potentially  
822 ~1 km higher than today in some areas. However, the sediments of the Nianbo Formation could  
823 have been deposited at an even higher altitude. The Paleocene-Eocene elevation estimate  
824 presented here is conservative because the isotopic lapse rate model is constructed using global  
825 mean T and RH data for the modern low-latitude ocean surface. The warmer temperatures of the  
826 Eocene would shift the  $\Delta(\delta^{18}\text{O})$ -elevation relationship to higher elevation changes for a given  
827 offset in precipitation isotopic compositions. We accept the modern calibration as a conservative  
828 representation of past environmental conditions because we are data-limited in our knowledge of  
829 the frequency distribution of low-latitude ocean surface T and RH in the Paleocene-Eocene.

830 The Paleocene-Eocene Nianbo Fm sits unconformably below the Rigongla in the Oiyug  
831 Basin, so the elevation history between the two units is unconstrained. However, the similarity of  
832 estimated  $T(\Delta_{47})$  and  $\delta^{18}\text{O}$  of the Nianbo and Rigongla imply little variability during this interval.  
833 The Rigongla and lower Gazhacun Fms yield elevation estimates close to the modern mean  
834 elevation of the Oiyug Basin.

835           A face value assessment of model elevations from the middle and upper Gazhacun  
836 Formations, when interpreted based on  $\Delta(\delta^{18}\text{O}_p)$  alone, would suggest that the southern Lhasa  
837 block experienced an interval of topographic deflation to 2.5 km in the early-mid Miocene.  
838 However, it is unlikely that the hypsometric mean elevation of the Oiyug Basin experienced  
839 subsidence from 4.5 km to 2.5 km in the Miocene, followed by an uplift to >6 km in the  
840 Pliocene, and subsidence to ~4.6 km by present day. It is more likely that the enriched oxygen  
841 values of the Gazhacun Formation are an evaporative overprint of the original precipitation  
842 signal.

843           However, the potential low in Miocene elevation temporally corresponds with the  
844 formation of the Kailas Basin (26 to 18 Ma; DeCelles et al., 2011) and Liuqu conglomerate (~21-  
845 17 Ma; Leary et al., 2017), both interpreted to have formed during an elevation low within the  
846 suture zone. The Kailas Formation, named after its type locality at Mt. Kailas, extends ~1400  
847 km along strike and is <1 to 4 km thick where exposed. The Kailas basin is interpreted as a  
848 continental rift basin resulting from <5 to 10 km horizontal extension, attributed to rollback of  
849 the subducting Indian slab beneath Tibet (DeCelles et al., 2011). The shearing and subsequent  
850 breakoff of the Indian slab would have caused a southward and downward pull on the overlying  
851 Indian continent, resulting in enough extension to drive the subsidence necessary to form the  
852 Kailas basin in southern Tibet (DeCelles et al., 2011).  $\delta^{13}\text{C}$  values from carbonate nodules within  
853 the Liuqu conglomerate are used in a paleo-environmental assessment suggesting that the IYS  
854 was wet and well-vegetated during deposition (Leary et al., 2017). These conditions are  
855 suggestive of low elevation.

856           Additionally, Ding et al. (2017) present paleoenthalpy-based paleoaltimetry that agrees  
857 with a low elevation IYS during Liuqu deposition, although they date the deposition of Liuqu

858 floras to the latest Paleocene (~56 Ma). Ding et al. (2017) also present paleoflora-based  
859 paleoaltimetry results from the Qiuwu Formation in Qiabulin (~26-19 Ma), which more closely  
860 correlates with the elevation estimates of Leary et al. (2017). Based on the Qiuwu Formation  
861 paleoenthalpy estimates, the IYS was already well above sea level ( $\sim 2.3 \pm 0.9$  km) by this interval  
862 of the Miocene. Due to the temporal overlap of the extension associated with the formation of  
863 the Kailas basin and Liuqu conglomerate, assuming Miocene deposition, and the deposition of  
864 the  $^{18}\text{O}$ -enriched sediments of the middle Gazhacun member in the Oiyug Basin, it is  
865 conceivable but unlikely that the marl calcites and dolomites in this study preserve a primary  
866 isotopic signature representative of mid-Miocene precipitation at low elevation.

867 Further work to the west along the southern Lhasa Block could determine whether the  
868 apparent lower elevations are actually a local evaporative overprint as interpreted here or are  
869 seen in the coeval carbonate record in the southern Lhasa block, and whether there is evidence  
870 elsewhere of ~6 km elevations at this time in the Miocene.

871

## 872 **Past models of the regional tectonic history of the Lhasa Block**

873 The tectonic development of Earth's quintessential active continent-continent collision  
874 zone has been extensively studied for the past three decades, with particular attention paid to the  
875 development and persistence of extreme high elevations. However, the majority of previous  
876 work on the uplift history invoke models of en masse (England and Houseman, 1986; Harrison et  
877 al., 1992; Molnar et al., 1993; Harrison et al., 1995) or local (Wang et al., 2006) plateau uplift in  
878 the Neogene. The paleoaltimetry work presented in this paper provides geochemical evidence  
879 that counters models involving late Cenozoic uplift.

880

881 *Late Cretaceous to Early Cenozoic*

882 Contrary to earlier models of Neogene uplift, (Kapp et al., 2007) presented tectonic  
883 evidence that the Lhasa Block must have undergone extensive crustal thickening by the early  
884 Paleogene, if not in the Cretaceous. Kapp et al. (2007) used kinematic models to demonstrate  
885 that a pre-collisional northward-vergent retroarc thrust belt could have accommodated >250 km  
886 of N-S shortening. They attribute an additional >160 km of shortening to the emplacement of the  
887 Lhasa-Damxung thrust sheet, which is associated with a magmatic flare-up ~69 Ma due to  
888 removal of thickened mantle lithosphere. Kapp et al. (2007) coin their tectonic evolution model  
889 for the Lhasa terrane the “Lhasaplano”—a Cretaceous-early Tertiary Cordilleran-style  
890 (contractional) orogen associated with the Gangdese magmatic arc. Our >4 km Paleocene-  
891 Eocene elevation reconstruction largely agrees with the Lhasaplano model.

892 *Late Cenozoic*

893 Harrison et al. (1992) and Molnar et al. (1993) assert that the southern Tibetan Plateau  
894 reached its maximum elevation by  $8\pm 1$  Ma. Harrison et al. (1992, 1995) suggest that the  
895 initiation of slip on the Nyainqentanghla detachment fault is result of the Tibetan Plateau  
896 attaining its maximum potential crustal thickness for the lithospheric temperature distribution  
897 and convergence rate. They reason that slip on the NE-SW striking Yangbajian graben northwest  
898 of Lhasa and other N-S striking rifts are indicative of extensional orogenic collapse due to over-  
899 thickening of the continental crust during shortening. Potassium feldspar and biotite  $^{40}\text{Ar}/^{39}\text{Ar}$   
900 thermochronological data from the uplifted footwall of the graben-defining Nyainqentanghla  
901 detachment fault are indicative of fault and shear zone initiation at  $8\pm 1$  Ma. They use the  
902 numerically modeled temperature history and slip rate (3 mm/yr) to predict that the southern



903 Tibetan Plateau reached its elevation and crustal thickness threshold at this time, and collapsed  
904 under its over-thickened crustal mass by way of graben formation.

905         However, as has been argued previously by Currie et al. (2005, 2016), and fully  
906 consistent with the new data presented here from the Oiyug Basin, existing paleoaltimetry data  
907 from various regions of the Lhasa block, including the Nima Basin (DeCelles et al., 2007;  
908 Huntington et al., 2015), and Lunpola Basin (Polissar et al., 2009; Rowley and Currie, 2006),  
909 Himalayas (Garzzone et al., 2000; Rowley and Garzzone, 2007; Gébelin et al., 2013; Rowley et  
910 al., 2003), as well as eastern Tibet (Hoke et al., 2014; Li et al., 2015) are all consistent with little  
911 or no change in elevation in the past 20 or more million years and thus these data incompatible  
912 with significant late Neogene uplift compatible with the models of Harrison et al. (1992) and  
913 Molnar et al. (1993).

914

## 915 **THE IMPACT OF EVAPORATIVE ENRICHMENT OF SURFACE WATERS ON** 916 **PALEOELEVATION ESTIMATES**

917         Elevations derived from two siderite samples (621F and 618A of the Oiyug Basin) are  
918 apparently offset by up to 2 km from the bulk of the data in their sampled sections. Here we  
919 present an assessment of evaporative overprinting of primary water signatures in these siderites.  
920 We interpret the siderites as evaporatively enriched, and report the mean elevation estimates of  
921 each formation focusing on preserved primary oxygen values.

922         Evaporative re-enrichment of  $\delta^{18}\text{O}_w$ , as recorded by  $\delta^{18}\text{O}_c$ , is particularly prevalent in  
923 carbonates formed in closed lakes and some groundwater systems (Steinman et al., 2013). The  
924 covariance of oxygen and hydrogen isotopes of meteoric water usually follow the established  
925 Global Meteoric Water Line (GMWL; Friedman, 1953; Rozanski et al., 1993). However, fast

926 evaporation causes a kinetic isotope effect that disturbs this trend with a greater effect on the  
927 oxygen isotopes (Craig, 1961). The “evaporative slope”, or trajectory off the GMWL, is  
928 determined by local relative humidity and temperature (Clark and Fritz, 1997). Polissar et al.  
929 (2009), using combined  $\delta^{18}\text{O}$  and  $\delta\text{D}$  of samples from the Lunpola Basin, were able to  
930 corroborate the interpretation of Rowley and Currie (2006) that variable evaporative enrichment  
931 was the primary control on the isotopic composition of their samples. Polissar et al. (2009)  
932 thereby provides independent support for the use of the more negative oxygen isotopic  
933 compositions for the purposes of paleoaltimetry.

934 Oiyug Basin localities 618 (Upper Gazhacun Fm) and 621 (Oiyug Fm) provide both  $\delta^{18}\text{O}$   
935 and  $\delta\text{D}$  (from carbonates and organics, respectively), allowing us to plot these samples relative to  
936 the long-term precipitation amount-weighted mean GMWL ( $\delta\text{D}=8.20 \times \delta^{18}\text{O}+11.27$ ; Rozanski et  
937 al., 1993). We correlate  $\delta^{18}\text{O}_w$  and  $\delta\text{D}_w$  using the GMWL in order to compare relative isotopic  
938 enrichment of different materials within the same sedimentary horizons (618 or 621; Fig. A2).  
939 Calcite-derived surface water oxygen isotope compositions from the 621 horizon are isotopically  
940 lighter than their corresponding  $\delta\text{D}$  values, calculated from coeval leaf waxes. Very low  $\delta^{18}\text{O}_w$   
941 could indicate diagenesis, but because both calcites retain primary  $\Delta_{47}$ -derived temperatures, we  
942 can rule out the possibility of excessive alteration. However, the two siderites from the 618 and  
943 621 localities yield  $\delta^{18}\text{O}_w$  estimates that are ~4 to 10‰ higher than expected from  $\delta\text{D}$  of coeval  
944 leaf waxes. Based on the observation that the calcites from these localities appear to preserve  
945 primary  $\delta^{18}\text{O}_w$  values, we interpret the  $^{18}\text{O}$ -enriched siderites to be the product of groundwater  
946 evaporation. This suggests that any estimated water  $\delta^{18}\text{O}$  compositions from this section with  
947 values  $>-20\text{‰}$  are likely evaporatively  $^{18}\text{O}$ -enriched. We follow this approach by stressing  
948 elevation estimates based on the more  $^{18}\text{O}$ -depleted compositions under the assumption that more

949 enriched values reflect more extensive evaporative re-enrichment relative to precipitation (Clark  
950 & Fritz, 1997).

951

## 952 **CENOZOIC CLIMATE**

953       Reported  $T(\Delta_{47})$  values (Table 3) are likely warmer than mean annual air temperature  
954 (MAAT) due to the nature of increased carbonate precipitation in the warm months in both soils  
955 and lake settings (Quade et al., 2013; Huntington et al., 2010).  $T(\Delta_{47})$  therefore likely describes a  
956 warm month, June-July-August (JJA), temperature for lake-derived sediments and a peak  
957 summer temperature for paleosols (Quade et al., 2013). Soil carbonate formation (due to  $\text{CO}_2$   
958 outgassing during groundwater evaporation) is most prevalent in the summer due to incident  
959 sunlight warming the uppermost 25 cm of soil. Lacustrine carbonate formation occurs in warm,  
960 unmixed near-surface waters. Here, abundant sunlight supports photosynthetic carbon fixation,  
961 which in turn can drive calcite and aragonite supersaturation by increasing pH and providing  
962 carbonate nucleation sites (Stumm and Morgan, 1981). For the purpose of both isotopic and  
963 temperature lapse rates in calculating paleo-elevations, reporting warmer temperatures than  
964 MAAT assures a conservative estimate of paleo-elevation.

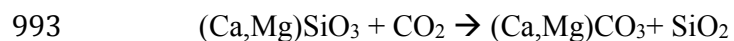
965       The increased evaporative signal seen in the middle Gazhacun lake sediments could  
966 indicate a paleo-environmental change, such as shallower, potentially closed playa lakes in this  
967 region in the mid-Miocene, or a paleo-climatic change, such as warmer temperatures, decreased  
968 humidity, or changes in atmospheric circulation injecting drier air masses. The lacustrine  
969 dolomites from the Badamaqen section are stratigraphically closest to clumped isotope sample  
970 555 with a  $T(\Delta_{47})$  value of  $19.7 \pm 4.2^\circ\text{C}$  ( $\pm$ s.e.m.). However, the lacustrine calcites, 551 and 553,  
971 are temporally bracketed by clumped isotope samples 554B and 548 with  $T(\Delta_{47})$  values of  $3.9 \pm$

972 3.4°C and  $7.6 \pm 3.3^\circ\text{C}$ , respectively. Khan et al. (2014) used the Climate Leaf Analysis  
973 Multivariate Program (CLAMP) on an ~15 Ma fossil flora from this region to estimate a WMMT  
974 of  $8.8^\circ\text{C}$  and cold month mean temperature (CMMT) of  $-6 \pm 4^\circ\text{C}$  for the Oiyug Basin. Sample 555  
975 does not provide enough evidence to suggest that the mean temperature of the Oiyug Basin was  
976 significantly warmer during the mid-Miocene. The evaporative enrichment signal, preserved as  
977 a shift to higher  $\delta^{18}\text{O}$  values in lake sediments can likely be attributed to shallow playa lake  
978 morphology. However, shifts in regional climate and atmospheric circulation should also be  
979 considered.

980

#### 981 **Tectonic-Weathering-Climate Feedbacks**

982 Himalayan paleoaltimetry, or more specifically, the timing of the rise of the Himalaya,  
983 has figured prominently in attempts to connect global cooling during the Cenozoic with  
984 continental weathering rates and  $p\text{CO}_2$  (Ruddiman and Kutzbach, 1989; Raymo and Ruddiman,  
985 1992; Harrison et al., 1992; Kutzbach et al., 1989; Molnar et al., 1993). Cenozoic cooling is  
986 documented most thoroughly in the  $\delta^{18}\text{O}$  records of benthic forams (e.g., Zachos et al., 2001).  
987 The potential for a connection between global climate and weathering is forged through the  
988 central role of  $\text{CO}_2$  as both a greenhouse gas and chemical weathering agent (e.g., Kump et al.,  
989 2000). The chemical weathering of silicate and aluminosilicate rocks consumes  $\text{CO}_2$  as carbonic  
990 acid, exporting cations and carbonate alkalinity to the oceans where both are removed as  
991 carbonate minerals with generic overall reactions (e.g., Ebelmen, 1845; Urey, 1952; Holland,  
992 1978; Berner and Maasch, 1996):



994 This type of chemical weathering serves as a net sink for atmospheric CO<sub>2</sub>. Raymo et al. (1988)  
995 and Raymo and Ruddiman (1992) suggested that uplift of the Himalaya could have enhanced  
996 chemical weathering rates by increasing the surface area of aluminosilicates available to weather.  
997 This surface area generation resulted from physical erosion processes that are accelerated by  
998 relief and glacial activity.

999 Evidence for the temporal link between the rise of the Himalaya and shifts in global  
1000 weathering fluxes has relied heavily on the marine Sr isotope record. Sr has a long residence  
1001 time in the oceans and is well mixed in terms of concentration and isotopic composition. Marine  
1002 carbonates record the <sup>87</sup>Sr/<sup>86</sup>Sr ratio of ambient seawater. The marine Sr isotope record is  
1003 strongly influenced by the weathering flux of Sr to the oceans, and therefore is used as a  
1004 weathering proxy (e.g., Richter et al., 1992; Edmonds, 1992). Shifts in the marine <sup>87</sup>Sr/<sup>86</sup>Sr  
1005 record over the Cenozoic appeared to coincide with earlier estimates for the timing of the uplift  
1006 of the Himalaya (e.g. Raymo and Ruddiman, 1992; Richter et al., 1992). Furthermore, modern  
1007 day weathering of highly radiogenic terrains in the Himalaya provides a large flux of radiogenic  
1008 Sr to the ocean, contributing to the continuing rise in the <sup>87</sup>Sr/<sup>86</sup>Sr ratio of sea water and  
1009 consistent with overall Neogene trends (Palmer and Edmond, 1989, 1992; Galy et al., 1999).

1010 Large changes in the Sr isotopic composition of the oceans from the late Eocene through  
1011 present are invoked to signify the onset and importance of weathering of the Himalaya and Tibet.  
1012 By extension, this curve is often cited as an indication that significant topography first developed  
1013 during the India-Eurasia collision at roughly 38 Ma (e.g. Raymo and Ruddiman, 1992; Misra and  
1014 Froelich, 2012). Misra and Froelich (2012) and others argue that other proxies for chemical  
1015 weathering rates and intensity of weathering, such as lithium isotopes, fit within this paradigm of  
1016 the onset of Tibetan weathering in the late Eocene.

1017 Our results provide strong evidence for high topography at the Tibetan margin dating to  
1018 at least 56 Ma. This is well before the marine  $^{87}\text{Sr}/^{86}\text{Sr}$  record begins its nearly monotonic climb  
1019 towards more radiogenic values. Palealtitudes in the Linzizong arc had reached modern  
1020 Tibetan elevations prior to the Paleocene – Eocene Thermal Maximum and overlapped with  
1021 Early Eocene equable climate states for the Earth (Fig. 8). These high elevations were achieved  
1022 at low latitudes (arc position roughly  $19 \pm 4^\circ \text{N}$ ; van Hinsbergen et al., 2012) in warm and wet  
1023 conditions favorable for intensive chemical weathering. All told, our paleoaltimetric findings  
1024 suggest that enhanced chemical weathering of the high Linzizong arc was insufficient to provide  
1025 significant climatic forcing, at least during the early and middle Eocene.

1026 This does not rule out the possibility for enhanced weathering related to high topography  
1027 along the southern Tibetan margin. The Linzizong arc was a source of highly reactive volcanic  
1028 glasses and lithologies, i.e., andesite, dacite, and rhyolite with some trachy-andesite and basaltic  
1029 trachy-andesite (Mo et al., 2008). Weathering of the Linzizong arc would have delivered rather  
1030 nonradiogenic Sr to the oceans. The  $^{87}\text{Sr}/^{86}\text{Sr}$  of relict volcanic arc dating to that interval is  
1031 generally between 0.7045 and 0.7075 (Mo et al., 2008). If the Linzizong Arc became globally  
1032 significant in terms of supplying weathered Sr to the oceans, the resultant Sr flux would not have  
1033 shifted marine  $^{87}\text{Sr}/^{86}\text{Sr}$  appreciably from its value of 0.7078 in the early Eocene.

1034 Even if there were enhanced chemical weathering associated with the early development  
1035 of high elevation in the Linzizong, the overall carbon cycle dynamics associated with tectonism  
1036 are complicated. Uplift and arc volcanism can be associated with enhanced outgassing of  
1037 metamorphic and volcanic  $\text{CO}_2$  (e.g., Kerrick and Caldeira, 1993), which could counteract or  
1038 even reverse the carbon balance in such a setting. If organic-rich marine sediments were also  
1039 exposed, then oxidative weathering of the organics would have served as an additional  $\text{CO}_2$

1040 source to the atmosphere (e.g., Beck et al., 1995). On the other hand, carbon sinks linked to  
1041 tectonism include the potential for enhanced organic carbon burial efficiency through rapid  
1042 burial rates in submarine fans and the high flux of fine grained sediments to the oceans with  
1043 subsequent mineral surface area control on organic matter burial (e.g., Hedges and Keil, 1995;  
1044 France-Lanord and Derry, 1997; Galy et al., 2007). Organic carbon burial rates could also be  
1045 influenced by changes in nutrient fluxes to the ocean as the rates and relative importance of  
1046 different weathering domains and marine depositional environments change (Compton and  
1047 Mallinson, 1996; Colman and Holland, 2000). Finally, the overall carbon mass balance for the  
1048 atmosphere-ocean system likewise links to carbon release from mid-ocean ridge (MOR)  
1049 spreading centers, and thus to global tectonism, which may or may not be coupled to regional  
1050 processes (Richter et al., 1992).

1051 Our results provide strong evidence that the marine Sr isotope record is not a sensitive  
1052 indicator for the early rise of the Tibetan margin nor for the impact that the development of this  
1053 topography had on global chemical weathering rates. The fact that this topography developed  
1054 during a time of globally warm climates suggests that any enhancement in chemical weathering  
1055 rates, which would have tended to lower atmospheric CO<sub>2</sub>, was offset by other features and  
1056 feedbacks in the global carbon cycle.

1057

## 1058 **CONCLUSIONS**

1059 We reconstruct an elevation history from the Tibetan Plateau spanning nearly the entire  
1060 Cenozoic, the onset of India-Asia collision to the present. This study provides multiple lines of  
1061 geochemical evidence that the southern margin of the Lhasa Block was at modern elevation or  
1062 higher (4 to >5km) around the onset of collision at about 55 Ma. In particular, carbonate clumped

1063 isotopes provide a new dimension to previous paleo-elevation reconstructions of the southern  
1064 Lhasa terrane. Additionally, the Paleocene-Eocene carbonates of the Penbo basin provide  
1065 apparent evidence that clumped isotope values can survive substantial burial and heating. This  
1066 result underscores the importance of detail and persistence in using isotopic proxies in studies of  
1067 past climate and tectonics.

1068 We find that both temperature lapse rates, informed by our clumped isotope  
1069 measurements, and traditional stable isotopic lapse rates of paleo-precipitation, informed by  
1070 oxygen isotopic compositions of lacustrine and pedogenic carbonates, agree that the sediments  
1071 associated with the Linzizong volcanic arc are in reasonable accord with the “Lhasaplano” model  
1072 of tectonic evolution. Further work on the central and northern plateau is necessary in order to  
1073 differentiate between a pre-existing Andean-type volcanic arc or more extensive high terrain  
1074 such as a proto-plateau in the early Cenozoic. Additionally, our data indicate high topography at  
1075 low latitude dating to before the Eocene Climatic Optimum, suggesting a more complicated  
1076 linkage between the Himalayan orogeny, proxies for chemical weathering, and the linkage  
1077 between tectonics, weathering, and climate.

1078

## 1079 **APPENDIX**

1080 **Figure A1. Inverse isochron plot of potassium feldspar  $^{40}\text{Ar}/^{39}\text{Ar}$  age.**

1081 **Figure A2. Effects of evaporation on siderites (dark red square), calcites (dark red circles)**  
1082 **and leaf wax (blue-green diamonds) from the same sedimentary horizon.** Inferred paleo-lake  
1083 and soil water hydrogen and oxygen isotope compositions are plotted for sedimentary horizons  
1084 621 (Oiyug Fm) and 618 (Gazhacun Gp). The  $\delta^{18}\text{O}_w$  values are calculated from  $\delta^{18}\text{O}_c$   
1085 measurements on carbonate minerals, and  $\delta\text{D}_w$  values are calculated from leaf waxes, as



1086 described in the main text. The  $\delta D_w$  and  $\delta^{18}O_w$  axes are aligned using the Rozanski et al (1993)  
1087 Global Meteoric Water Line equation ( $\delta D=8.20 \times \delta^{18}O+11.27$ ). This alignment means that if the  
1088 paleo-water isotopic composition lay on the modern Global Meteoric Water line, the  
1089 corresponding carbonate and leaf wax samples would yield inferred  $\delta^{18}O_w$  and  $\delta D_w$  values in the  
1090 same vertical position. Lacustrine siderite 621F has experienced much greater evaporative  
1091 enrichment than pedogenic calcites 621H and 621I from the same strata. This could be indicative  
1092 of a period of greater aridity or deposition in a closed playa lake rather than an open system, or a  
1093 change in atmospheric circulation over the Lhasa Block in the late Cenozoic. The difference  
1094 between the isotopic compositions of leaf waxes and siderite in the Miocene Gazhacun  
1095 Formation is negligible within uncertainty.

1096 **Table A1.** Summary of  $\Delta_{47}$  measurements on standard calcite materials run during the same  
1097 analytical periods as the samples reported in this paper (2014-2016).

1098 **Table A2.** Isotopic measurements ( $\delta^{13}C$ ,  $\delta^{18}O$ ,  $\Delta_{47,SG-WG}$ ,  $\delta_{47}$ ,  $\Delta_{48}$ ) of all standard calcite  
1099 materials run during the same analytical periods as the samples reported in this paper (2014-  
1100 2016).

1101

## 1102 **ACKNOWLEDGMENTS**

1103 We thank R. Plotnick and K. Ritterbush for assistance with petrographic analyses, B. He for  
1104 assistance with clumped isotope measurements, and D. Schrag and S. Bernasconi for providing  
1105 carbonate isotopic standards. M.I. would like to thank Madison Ball and Xu Qiang for assistance  
1106 in the field. The science and structure of this work were greatly improved by thoughtful reviews  
1107 by D. Orme and J. Quade, and comments from Editor B. Singer. This work is supported by  
1108 National Science Foundation EAR#0609756 awarded to B.C and #1111274 to D.B.R. and D.S.,

1109 and Geological Society of America Graduate Student Research Grant to M.I. Geochemical

1110 analyses were enabled by NSF EAR#0923831 awarded to A.S.C. and D.B.R.

1111

## 1112 REFERENCES CITED

- 1113 Barker, C.E., 1988, Geothermics of petroleum systems: Implications of the stabilization of  
1114 kerogen thermal maturation after a geologically brief heating duration at peak temperature:  
1115 Petroleum systems of the United States: US Geological Survey Bulletin, v. 1870, p. 26–29.
- 1116 Beck, R.A., Burbank, D.W., Sercombe, W.J., Riley, G.W., Barndt, J.K., Berry, J.R., Afzal, J.,  
1117 Khan, A.M., Jurgen, H., Metje, J., Cheema, A., Shafique, N.A., Lawrence, R.D., and Khan,  
1118 M.A., 1995, Stratigraphic evidence for an early collision between northwest India and Asia:  
1119 Nature, v. 373, p. 55–58, doi: 10.1038/373055a0.
- 1120 Berner, R., and Maasch, K., 1996, Chemical weathering and controls on atmospheric O<sub>2</sub> and  
1121 CO<sub>2</sub>: Fundamental principles were enunciated by J.J. Ebelman in 1845: *Geochimica et*  
1122 *Cosmochimica Acta*, v. 60, p. 1633–1637.
- 1123 Burg, J.-P., Proust, F., Tapponnier, P., and Chen, G.M., 1983, Deformation phases and tectonic  
1124 evolution of the Lhasa block (southern Tibet, China): *Eclogae Geologicae Helvetiae*, v. 76,  
1125 p. 643–665.
- 1126 Burgener, L., Huntington, K.W., Hoke, G.D., Schauer, A., Ringham, M.C., Latorre, C., and  
1127 Díaz, F.P., 2016, Variations in soil carbonate formation and seasonal bias over >4 km of  
1128 relief in the western Andes (30°S) revealed by clumped isotope thermometry: *Earth and*  
1129 *Planetary Science Letters*, v. 441, p. 188–199, doi:  
1130 <http://dx.doi.org/10.1016/j.epsl.2016.02.033>.
- 1131 Chen, H., Han, J., Ding, Z., Sun, H., and Guo, Z., 2008, Chronological dating and tectonic  
1132 implications of late Cenozoic volcanic rocks and lacustrine sequence in Oiyug Basin of  
1133 southern Tibet: *Science in China Series D*, v. 51, p. 275–283.
- 1134 Clark, I., and Fritz, P., 1997, *Environmental Isotopes in Hydrogeology*: Boca Raton, Lewis  
1135 Publishers.
- 1136 Colman, A.S., and Holland, H., 2000, The global diagenetic flux of phosphorus from marine  
1137 sediments to oceans: Redox sensitivity and the control of atmospheric oxygen levels:
- 1138 Compton, J., and Mallinson, D., 1996, Geochemical consequences of increased Late Cenozoic  
1139 weathering rates and the global CO<sub>2</sub> balance since 100 Ma: *Paleoceanography*, v. 11, p.  
1140 431–446.
- 1141 Coplen, T., Brand, W., Gehre, M., Groning, M., Meijer, H., Toman, B., and Verkouteren, R.,  
1142 2006, New guidelines for δ<sup>13</sup>C measurements: *Analytical Chemistry*, v. 78, p. 3439–2441.
- 1143 Craig, H., 1961, Isotopic variations in meteoric waters: *Science*, v. 133, p. 1702–1703.
- 1144 Currie, B.S., Polissar, P.J., Rowley, D.B., Ingalls, M., Li, S., and Freeman, K.H., 2016,  
1145 Multiproxy paleoaltimetry of the late Oligocene-Pliocene Oiyug Basin, southern Tibet:  
1146 *American Journal of Science*, v. 316, p. 401–436, doi: 10.2475/05.2016.01.
- 1147 Currie, B.S., Rowley, D.B., and Tabor, N.J., 2005, Middle Miocene paleoaltimetry of southern  
1148 Tibet: Implications for the role of mantle thickening and delamination in the Himalayan  
1149 orogen: *Geology*, v. 33, p. 181, doi: 10.1130/G21170.1.
- 1150 Dansgaard, W., 1954, The O<sub>18</sub> abundance in fresh water: *Geochimica et Cosmochimica Acta*, v.

1151 6, p. 241–260.

1152 DeCelles, P., Kapp, P., Gehrels, G., and Ding, L., 2014, Paleocene- Eocene foreland basin  
1153 evolution in the Himalaya of southern Tibet and Nepal: Implications for the age of initial  
1154 India- Asia collision: *Tectonics*, v. 33, doi: 10.1002/2014TC003522.

1155 DeCelles, P.G., Kapp, P., Quade, J., and Gehrels, G.E., 2011, Oligocene-Miocene Kailas basin,  
1156 southwestern Tibet: Record of postcollisional upper-plate extension in the Indus-Yarlung  
1157 suture zone: *Bulletin of the Geological Society of America*, v. 123, p. 1337–1362, doi:  
1158 10.1130/B30329.1.

1159 DeCelles, P.G., Quade, J., Kapp, P., Fan, M., Dettman, D.L., and Ding, L., 2007, High and dry in  
1160 central Tibet during the Late Oligocene: *Earth and Planetary Science Letters*, v. 253, p.  
1161 389–401, doi: 10.1016/j.epsl.2006.11.001.

1162 Defliese, W.F., Hren, M.T., and Lohmann, K.C., 2015, Compositional and temperature effects of  
1163 phosphoric acid fractionation on  $\Delta 47$  analysis and implications for discrepant calibrations:  
1164 *Chemical Geology*, v. 396, p. 51–60, doi: 10.1016/j.chemgeo.2014.12.018.

1165 Dennis, K., Affek, H., Passey, B., Schrag, D., and Eiler, J., 2011, Defining an absolute reference  
1166 frame for “clumped” isotope studies of CO<sub>2</sub>: *Geochimica et Cosmochimica Acta*, v. 75, p.  
1167 7117–7131, doi: 10.1016/j.gca.2011.09.025.

1168 Ding, L., and Lai, Q., 2003, New geological evidence of crustal thickening in the Gangdese  
1169 block prior to the Indo-Asian collision: *Chinese Science Bulletin*, v. 48, p. 1604–1610.

1170 Ding, L., Spicer, R.A., Yang, J., Xu, Q., Cai, Q., Li, S., Lai, Q., Wang, H., Spicer, T.E.V., Yue,  
1171 Y., Shukla, A., Srivastava, G., Ali Khan, M., Bera, S., et al., 2017, Quantifying the rise of  
1172 the Himalaya orogen and implications for the South Asian monsoon: *Geology*, p. G38583.1,  
1173 doi: 10.1130/G38583.1.

1174 Ding, L., Xu, Q., Yue, Y., Wang, H., Cai, F., and Li, S., 2014, The Andean-type Gangdese  
1175 Mountains: Paleoelevation record from the Paleocene–Eocene Linzhou Basin: *Earth and  
1176 Planetary Science Letters*, v. 392, p. 250–264, doi: 10.1016/j.epsl.2014.01.045.

1177 Ebelmen, J., 1845, Sur les produits de la decomposition des especes minerales de la famille des  
1178 silicates: *Ann. des Mines*, v. 7, p. 3–66.

1179 Edmonds, J.M., 1992, Himalayan tectonics, weathering processes, and the strontium isotope  
1180 record in marine limestones: *Science*, v. 258, p. 1594–1597.

1181 Eiler, J.M., 2007, “Clumped-isotope” geochemistry—The study of naturally-occurring, multiply-  
1182 substituted isotopologues: *Earth and Planetary Science Letters*, v. 262, p. 309–327, doi:  
1183 10.1016/j.epsl.2007.08.020.

1184 England, P., and Houseman, G., 1986, Finite strain calculations of continental deformation: 2.  
1185 Comparison with the India- Asia collision zone: *Journal of Geophysical Research*: ..., v.  
1186 91, p. 3664–3676.

1187 Farley, K.A., Wolf, R.A., and Silver, L.T., 1996, The effects of long alpha-stopping distances on  
1188 (U-Th)/He ages: *Geochimica et Cosmochimica Acta*, v. 60, p. 4223–4229.

1189 France-Lanord, C., and Derry, L., 1997, Organic carbon burial forcing of the carbon cycle from  
1190 Himalayan erosion: *Nature*, v. 390, p. 65–67.

1191 Friedman, I., 1953, Deuterium content of natural waters and other substances: *Geochimica et  
1192 Cosmochimica Acta*, v. 4, p. 89–103.

1193 Gaetani, M., and Garzanti, E., 1991, Multicyclic History of the Northern India Continental  
1194 Margin (Northwestern Himalaya) (1): *AAPG Bulletin*, v. 75, p. 1427–1446.

1195 Gallagher, T.M., and Sheldon, N.D., 2016, Combining soil water balance and clumped isotopes

1196 to understand the nature and timing of pedogenic carbonate formation: *Chemical Geology*,  
1197 v. 435, p. 79–91, doi: <http://dx.doi.org/10.1016/j.chemgeo.2016.04.023>.

1198 Galy, A., France-Lanord, C., Beyssac, O., Faure, P., Kudrass, H., and Palhol, F., 2007, Efficient  
1199 organic carbon burial in the Bengal fan sustained by the Himalayan erosional system:  
1200 *Nature*, v. 450, p. 407–410.

1201 Galy, A., France-Lanord, C., and Derry, L., 1999, The strontium isotopic budget of Himalayan  
1202 rivers in Nepal and Bangladesh: *Geochimica et Cosmochimica Acta*, v. 63, p. 1905–1925.

1203 Garzione, C.N., Dettman, D.L., and Horton, B.K., 2004, Carbonate oxygen isotope  
1204 paleoaltimetry: evaluating the effect of diagenesis on paleoelevation estimates for the  
1205 Tibetan plateau: *Palaeogeography, Palaeoclimatology, Palaeoecology*, v. 212, p. 119–140,  
1206 doi: 10.1016/j.palaeo.2004.05.020.

1207 Garzione, C.N., Dettman, D.L., Quade, J., DeCelles, P.G., and Butler, R.F., 2000, High times on  
1208 the Tibetan Plateau: Paleoelevation of the Thakkhola graben, Nepal: *Geology*, v. 28, p.  
1209 339–342.

1210 Gébelin, A., Mulch, A., Teyssier, C., Jessup, M.J., Law, R.D., and Brunel, M., 2013, The  
1211 Miocene elevation of Mount Everest: *Geology*, v. 41, p. 799–802, doi: 10.1130/G34331.1.

1212 Ghosh, P., Adkins, J., Affek, H., Balta, B., Guo, W.W., Schauble, E.E. a., Schrag, D., Eller, J.,  
1213 and Eiler, J.M., 2006, 13C–18O bonds in carbonate minerals: A new kind of  
1214 paleothermometer: *Geochimica et Cosmochimica Acta*, v. 70, p. 1439–1456, doi:  
1215 10.1016/j.gca.2005.11.014.

1216 Ghosh, P., Garzione, C.N., and Eiler, J.M., 2006, Rapid uplift of the Altiplano revealed through  
1217 13C-18O bonds in paleosol carbonates.: *Science (New York, N.Y.)*, v. 311, p. 511–5, doi:  
1218 10.1126/science.1119365.

1219 Gonfiantini, R., 1983, Advisory group meeting on stable isotope reference samples for  
1220 geochemical and hydrological investigations, *in* Report to the Director General, Vienna, p.  
1221 77.

1222 Green, O.R., Searle, M.P., Corfield, R.I., and Corfield, R.M., 2008, Cretaceous-Tertiary  
1223 Carbonate Platform Evolution and the Age of the India-Asia Collision along the Ladakh  
1224 Himalaya (Northwest India): *The Journal of Geology*, v. 116, p. 331–353, doi:  
1225 10.1086/588831.

1226 H45C002003, 2002, Digital Library of NGAC,.  
1227 H46C003001, 2012, Digital Library of NGAC,.

1228 Harrison, T.M., Copeland, P., Kidd, W.S.F., and Lovera, O.M., 1995, Activation of the  
1229 Nyainqentanghla Shear Zone: Implications for uplift of the southern Tibetan Plateau:  
1230 *Tectonics*, v. 14, p. 658–676.

1231 Harrison, T.M., Copeland, P., Kidd, W.S., and Yin, A., 1992, Raising tibet.: *Science (New York,*  
1232 *N.Y.)*, v. 255, p. 1663–70, doi: 10.1126/science.255.5052.1663.

1233 He, S., Kapp, P., DeCelles, P.G., Gehrels, G.E., and Heizler, M., 2007, Cretaceous-Tertiary  
1234 geology of the Gangdese Arc in the Linzhou area, southern Tibet: *Tectonophysics*, v. 433,  
1235 p. 15–37, doi: 10.1016/j.tecto.2007.01.005.

1236 He, B., Olack, G., and Colman, A., 2012, Pressure baseline correction and high-precision CO2  
1237 clumped-isotope ( $\Delta 47$ ) measurements in bellows and micro-volume modes.: *Rapid*  
1238 *communications in mass spectrometry*, v. 26, p. 2837–53, doi: 10.1002/rcm.6436.

1239 Hedges, J., and Keil, R., 1995, Sedimentary organic matter preservation: an assessment and  
1240 speculative synthesis: *Marine Chemistry*, v. 49, p. 81–115.

1241 Henkes, G.A., Passey, B.H., Grossman, E.L., Shenton, B.J., Perez-Huerta, A., and Yancey, T.E.,

1242 2014, Temperature limits for preservation of primary calcite clumped isotope  
1243 paleotemperatures: *Geochimica et Cosmochimica Acta*, v. 139, p. 362–382.  
1244 van Hinsbergen, D.J.J., Lippert, P.C., Dupont-Nivet, G., McQuarrie, N., Doubrovine, P. V,  
1245 Spakman, W., and Torsvik, T.H., 2012, Greater India Basin hypothesis and a two-stage  
1246 Cenozoic collision between India and Asia.: *Proceedings of the National Academy of*  
1247 *Sciences of the United States of America*, v. 109, p. 7659–64, doi:  
1248 10.1073/pnas.1117262109.  
1249 Hoke, G.D., Liu-Zeng, J., Hren, M.T., Wissink, G.K., and Garzzone, C.N., 2014, Stable isotopes  
1250 reveal high southeast Tibetan Plateau margin since the Paleogene: *Earth and Planetary*  
1251 *Science Letters*, v. 394, p. 270–278, doi: 10.1016/j.epsl.2014.03.007.  
1252 Holland, H., 1978, *The Chemistry of the Atmosphere and Oceans*: New York, Wiley, 351 p.  
1253 Hough, B., Fan, M., and Passey, B., 2014, Calibration of the clumped isotope geothermometer in  
1254 soil carbonate in Wyoming and Nebraska, USA: Implications for paleoelevation and  
1255 paleoclimate reconstruction: *Earth and Planetary Science Letters*, v. 391, p. 110–120.  
1256 Hren, M.T., Bookhagen, B., Blisniuk, P.M., Booth, A.L., and Chamberlain, C.P., 2009,  $\delta^{18}\text{O}$   
1257 and  $\delta\text{D}$  of streamwaters across the Himalaya and Tibetan Plateau: Implications for moisture  
1258 sources and paleoelevation reconstructions: *Earth and Planetary Science Letters*, v. 288, p.  
1259 20–32.  
1260 Hu, X., Garzanti, E., Moore, T., and Raffi, I., 2015, Direct stratigraphic dating of India-Asia  
1261 collision onset at the Selandian (middle Paleocene,  $59 \pm 1$  Ma): *Geology*, v. 43, p. 859–862,  
1262 doi: 10.1130/g36872.1.  
1263 Huntington, K.W., Eiler, J.M., Affek, H.P., Guo, W., Bonifacie, M., Yeung, L.Y., Thiagarajan,  
1264 N., Passey, B., Tripathi, a, Daëron, M., and Came, R., 2009, Methods and limitations of  
1265 “clumped”  $\text{CO}_2$  isotope ( $\Delta 47$ ) analysis by gas-source isotope ratio mass spectrometry.:  
1266 *Journal of mass spectrometry : JMS*, v. 44, p. 1318–29, doi: 10.1002/jms.1614.  
1267 Huntington, K.W., Saylor, J., Quade, J., and Hudson, A.M., 2015, High late Miocene-Pliocene  
1268 elevation of the Zhada Basin, southwestern Tibetan Plateau, from carbonate clumped  
1269 isotope thermometry: *Geological Society of America Bulletin*, v. 127, p. 181–199, doi:  
1270 10.1130/B31000.1.  
1271 Huntington, K.W., Wernicke, B.P., and Eiler, J.M., 2010, Influence of climate change and uplift  
1272 on Colorado Plateau paleotemperatures from carbonate clumped isotope thermometry:  
1273 *Tectonics*, v. 29, doi: 10.1029/2009TC002449.  
1274 Ingalls, M., 2017, Subduction and uplift of continental crust in the India-Asia collision zone:  
1275 Clumped-isotope paleothermometry and paleoaltimetry of the Lhasa block, southern Tibet:  
1276 PhD dissertation, University of Chicago, 250 p.  
1277 Ingalls, M., Rowley, D.B., Currie, B., and Colman, A.S., 2016, Large-scale subduction of  
1278 continental crust implied by India–Asia mass-balance calculation: *Nature Geoscience*, v. 9,  
1279 p. 848–853, doi: 10.1038/ngeo2806.  
1280 Kalnay, E., Kanamitsu, M., Kistler, R., Collins, W., Deaven, D., Gandin, L., Iredell, M., Saha,  
1281 S., White, G., Woollen, J., Zhu, Y., Chelliah, M., Ebisuzaki, W., Higgins, W., et al., 1996,  
1282 The NCEP/NCAR 40-Year Reanalysis Project: *Bulletin of the American Meteorological*  
1283 *Society*, v. 77, p. 437–471.  
1284 Kapp, P., DeCelles, P.G., Leier, A.L., Fabijanic, J.M., He, S., Pullen, A., Gehrels, G.E., and  
1285 Ding, L., 2007, The Gangdese retroarc thrust belt revealed: *GSA Today*, v. 17, p. 4–9, doi:  
1286 10.1130/GSAT01707A.1.  
1287 Kapp, P., Yin, A., Harrison, T.M., and Ding, L., 2005, Cretaceous-Tertiary shortening, basin

1288 development, and volcanism in central Tibet: *Bulletin of the Geological Society of*  
1289 *America*, v. 117, p. 865–878, doi: 10.1130/B25595.1.

1290 Kerrick, D., and Caldeira, K., 1993, Paleatmospheric consequences of CO<sub>2</sub> released during  
1291 early Cenozoic regional metamorphism in the Tethyan orogen: *Chemical Geology*, v. 108,  
1292 p. 201–230.

1293 Khan, M.A., Spicer, R.A., Bera, S., Ghosh, R., Yang, J., Spicer, T.E.V., Guo, S., Su, T., Jacques,  
1294 F., and Grote, P.J., 2014, Miocene to Pleistocene floras and climate of the Eastern  
1295 Himalayan Siwaliks, and new palaeoelevation estimates for the Namling–Oiyug Basin,  
1296 Tibet: *Global and Planetary Change*, v. 113, p. 1–10, doi: 10.1016/j.gloplacha.2013.12.003.

1297 Koppers, A.A.P., 2002, ArArCALC - software for Ar-40/Ar-39 age calculations: *Computers and*  
1298 *Geosciences*, v. 28, p. 605–619.

1299 Kump, L., Brantley, S., and Arthur, M., 2000, Chemical weathering, atmospheric CO<sub>2</sub>, and  
1300 climate: *Annual Review of Earth and Planetary Sciences*, v. 28, p. 611–667.

1301 Kutzbach, J.E., Guetter, P.J., Ruddiman, W.F., and Prell, W.L., 1989, Sensitivity of climate to  
1302 late Cenozoic uplift in southern Asia and the American west: Numerical experiments:  
1303 *Journal of Geophysical Research*, v. 94, p. 18393, doi: 10.1029/JD094iD15p18393.

1304 Lawrimore, J.H., Menne, M.J., Gleason, B.E., Williams, C.N., Wuertz, D.B., Vose, R.S., and  
1305 Rennie, J., 2011, An overview of the Global Historical Climatology Network monthly mean  
1306 temperature data set, version 3: *Journal of Geophysical Research*, v. 116, doi:  
1307 10.1029/2011JD016187.

1308 Leary, R.J., Quade, J., DeCelles, P.G., and Reynolds, A., 2017, Evidence from paleosols for low  
1309 to moderate elevation of the India-Asia suture zone during mid-Cenozoic time: *Geology*, v.  
1310 45, p. G38830.1, doi: 10.1130/G38830.1.

1311 Leier, A.L., DeCelles, P.G., Kapp, P., and Ding, L., 2007, The Takeda Formation of the Lhasa  
1312 terrane, southern Tibet: The record of a Late Cretaceous retroarc foreland basin: *Geological*  
1313 *Society of America Bulletin*, v. 119, p. 31–48, doi: 10.1130/B25974.1.

1314 Leier, A., Quade, J., DeCelles, P., and Kapp, P., 2009, Stable isotopic results from paleosol  
1315 carbonate in South Asia: Paleoenvironmental reconstructions and selective alteration: *Earth*  
1316 *and Planetary Science Letters*, v. 279, p. 242–254, doi: 10.1016/j.epsl.2008.12.044.

1317 Li, S., Currie, B.S., Rowley, D.B., and Ingalls, M., 2015, Cenozoic paleoaltimetry of the SE  
1318 margin of the Tibetan Plateau: Constraints on the tectonic evolution of the region: *Earth and*  
1319 *Planetary Science Letters*, v. 432, p. 415–424, doi: 10.1016/j.epsl.2015.09.044.

1320 Machette, M.N., 1985, Calcic soils of the southwestern United States: *Geological Society of*  
1321 *America Special Paper*, v. 203, p. 1–21, doi: 10.1130/SPE203-p1.

1322 Mack, G., and Rasmussen, K., 1984, Alluvial-fan sedimentation of the Cutler Formation (Permo-  
1323 Pennsylvanian) near Gateway, Colorado: *Geological Society of America Bulletin*, v. 95, p.  
1324 109 LP-116.

1325 Misra, S., and Froelich, P.N., 2012, Lithium isotope history of Cenozoic seawater: changes in  
1326 silicate weathering and reverse weathering: *Science*, v. 335, p. 818–823.

1327 Mo, X.X., Niu, Y.L., Dong, G.C., Zhao, Z.D., Hou, Z.Q., Zhou, S., and Ke, S., 2008,  
1328 Contribution of syncollisional felsic magmatism to continental crustal growth: A case study  
1329 of the Paleogene Linzizong volcanic succession in southern Tibet: *Chemical Geology*, v.  
1330 250, p. 49–67.

1331 Molnar, P., England, P., and Martinod, J., 1993, Mantle dynamics, uplift of the Tibetan Plateau,  
1332 and the Indian Monsoon: *Reviews of Geophysics*, v. 31, p. 357, doi: 10.1029/93RG02030.

1333 Murphy, M.A., Yin, A., Harrison, T.M., Dürr, S.B., Z, C., Ryerson, F.J., Kidd, W.S.F., X, W., X,

1334 Z., Durr, S.B., Z, C., Ryerson, F.J., Kidd, W.S.F., X, W., et al., 1997, Did the Indo-Asian  
1335 collision alone create the Tibetan plateau? *Geology*, v. 25, p. 719, doi: 10.1130/0091-  
1336 7613(1997)025<0719:DTIACA>2.3.CO;2.

1337 Orme, D.A., 2015, Basin evolution and exhumation of the Xigaze forearc and Indus-Yarlung  
1338 suture zone, Tibet: University of Arizona, 305 p.

1339 Palmer, M.R., and Edmond, J.M., 1992, Controls over the strontium isotope composition of river  
1340 water: *Geochimica et Cosmochimica Acta*, v. 56, p. 2099–2111.

1341 Palmer, M.R., and Edmond, J.M., 1989, The strontium isotope budget of the modern ocean:  
1342 *Earth and Planetary Science Letters*, v. 92, p. 11–26.

1343 Passey, B.H., Levin, N.E., Cerling, T.E., Brown, F.H., and Eiler, J.M., 2010, High-temperature  
1344 environments of human evolution in East Africa based on bond ordering in paleosol  
1345 carbonates.: *Proceedings of the National Academy of Sciences of the United States of*  
1346 *America*, v. 107, p. 11245–9, doi: 10.1073/pnas.1001824107.

1347 Pearson, P.N., Ditchfield, P.W., Singano, J., Harcourt-Brown, K.G., Nicholas, C.J., Olsson, R.K.,  
1348 Shackleton, N.J., and Hall, M.A., 2001, Warm tropical sea surface temperatures in the Late  
1349 Cretaceous and Eocene epochs.: *Nature*, v. 413, p. 481–7, doi: 10.1038/35097000.

1350 Peters, N. a., Huntington, K.W., and Hoke, G.D., 2013, Hot or not? Impact of seasonally variable  
1351 soil carbonate formation on paleotemperature and O-isotope records from clumped isotope  
1352 thermometry: *Earth and Planetary Science Letters*, v. 361, p. 208–218, doi:  
1353 10.1016/j.epsl.2012.10.024.

1354 Le Pichon, X., Fournier, M., and Jolivet, L., 1992, Kinematics, topography, shortening, and  
1355 extrusion in the India- Eurasia collision: *Tectonics*, v. 11, p. 1085–1098.

1356 Polissar, P.J., Freeman, K.H., Rowley, D.B., McInerney, F. a., and Currie, B.S., 2009,  
1357 Paleoaltimetry of the Tibetan Plateau from D/H ratios of lipid biomarkers: *Earth and*  
1358 *Planetary Science Letters*, v. 287, p. 64–76, doi: 10.1016/j.epsl.2009.07.037.

1359 Quade, J., Cater, J.M.L., Ojha, T.P., Adam, J., and Mark Harrison, T., 1995, Late Miocene  
1360 environmental change in Nepal and the northern Indian subcontinent: Stable isotopic  
1361 evidence from paleosols: *Geological Society of America Bulletin*, v. 107, p. 1381–1397,  
1362 doi: 10.1130/0016-7606(1995)107.

1363 Quade, J., and Cerling, T.E., 1995, Expansion of C4 grasses in the late Miocene of northern  
1364 Pakistan: Evidence from stable isotopes in paleosols: *Palaeogeography, Palaeoclimatology,*  
1365 *Palaeoecology*, v. 115, p. 91–116.

1366 Quade, J., Cerling, T.E., and Bowman, J.R., 1989, Development of Asian monsoon revealed by  
1367 marked ecological shift during hte latest Miocene in northern Pakistan: *Nature*, v. 342, p.  
1368 163–165, doi: 10.1038/340301a0.

1369 Quade, J., Eiler, J., Daëron, M., and Achyuthan, H., 2013, The clumped isotope geothermometer  
1370 in soil and paleosol carbonate: *Geochimica et Cosmochimica Acta*, v. 105, p. 92–107, doi:  
1371 10.1016/j.gca.2012.11.031.

1372 Quade, J., Garzzone, C., and Eiler, J., 2007, Paleoelevation reconstruction using pedogenic  
1373 carbonates: *Reviews in Mineralogy and Geochemistry*, v. 66, p. 53–87.

1374 Raymo, M., and Ruddiman, W., 1992, Tectonic forcing of late Cenozoic climate: *Nature*, v. 359,  
1375 p. 117–122.

1376 Raymo, M., Ruddiman, W., and Froelich, P.N., 1988, Influence of late Cenozoic mountain  
1377 building on ocean geochemical cycles: *Geology*, v. 16, p. 649–653.

1378 Richter, F., Rowley, D., and DePaolo, D., 1992, Sr isotope evolution of seawater: the role of  
1379 tectonics: *Earth and Planetary Science Letters*, v. 109, p. 11–23.

1380 Ringham, M.C., Hoke, G.D., Huntington, K.W., and Aranibar, J.N., 2016, Influence of  
1381 vegetation type and site-to-site variability on soil carbonate clumped isotope records,  
1382 Andean piedmont of Central Argentina (32-34°S): *Earth and Planetary Science Letters*, v.  
1383 440, p. 1–11.

1384 Rohrmann, A., Kapp, P., Carrapa, B., Reiners, P.W., Guynn, J., Ding, L., and Heizler, M., 2012,  
1385 Thermochronologic evidence for plateau formation in central Tibet: By 45 Ma: *Geology*, v.  
1386 40, p. 187–190, doi: 10.1130/G32530.1.

1387 Rowley, D.B., 2007, Stable Isotope-Based Paleoaltimetry: Theory and Validation: *Reviews in*  
1388 *Mineralogy and Geochemistry*, v. 66, p. 23–52, doi: 10.2138/rmg.2007.66.2.

1389 Rowley, D.B., and Currie, B.S., 2006, Palaeo-altimetry of the late Eocene to Miocene Lunpola  
1390 basin, central Tibet.: *Nature*, v. 439, p. 677–81, doi: 10.1038/nature04506.

1391 Rowley, D.B., Currie, B.S., and Pierrehumbert, R.T., 2003, Modern precipitation stable isotope  
1392 vs. elevation gradients in the High Himalaya, reply: *Earth and Planetary Science Letters*, v.  
1393 209, p. 401–403.

1394 Rowley, D.B., and Garzzone, C.N., 2007, Stable Isotope-Based Paleoaltimetry: *Annual Review*  
1395 *of Earth and Planetary Sciences*, v. 35, p. 463–508, doi:  
1396 10.1146/annurev.earth.35.031306.140155.

1397 Rowley, D.B., Pierrehumbert, R.T., and Currie, B.S., 2001, A new approach to stable isotope-  
1398 based paleoaltimetry: implications for paleoaltimetry and paleohypsometry of the High  
1399 Himalaya since the Late Miocene: *Earth and Planetary Science Letters*, v. 5836, p. 1–17,  
1400 doi: 10.1016/S0012-821X(01)00324-7.

1401 Rozanski, K., Araguas-Araguas, L., and Gonfiantini, R., 1993, Isotopic patterns in modern global  
1402 precipitation, *in* *Climatic Change in Continental Isotopic Records*, Washington, D. C.,  
1403 American Geophysical Union, p. 1–36, doi: 10.1029/GM078p0001.

1404 Ruddiman, W.F., and Kutzbach, J.E., 1989, Forcing of late Cenozoic northern hemisphere  
1405 climate by plateau uplift in southern Asia and the American west: *Journal of Geophysical*  
1406 *Research*, v. 94, p. 18409, doi: 10.1029/JD094iD15p18409.

1407 Saylor, J.E., Quade, J., Dettman, D.L., DeCelles, P.G., Kapp, P. a., and Ding, L., 2009, The late  
1408 Miocene through present paleoelevation history of southwestern Tibet: *American Journal of*  
1409 *Science*, v. 309, p. 1–42, doi: 10.2475/01.2009.01.

1410 Spicer, R.A., Harris, N.B.W., Widdowson, M., Herman, A.B., Guo, S., Valdes, P.J., Wolfe, J.A.,  
1411 and Kelley, S.P., 2003, Constant elevation of southern Tibet over the past 15 million years.:  
1412 *Nature*, v. 421, p. 622–4, doi: 10.1038/nature01356.

1413 Steinman, B.A., Abbott, M.B., Nelson, D.B., Stansell, N.D., Finney, B.P., Bain, D.J., and  
1414 Rosenmeier, M.F., 2013, Isotopic and hydrologic responses of small, closed lakes to climate  
1415 variability: Comparison of measured and modeled lake level and sediment core oxygen  
1416 isotope records: *Geochimica et Cosmochimica Acta*, v. 105, p. 455–471.

1417 Stolper, D.A., and Eiler, J.M., 2015, The kinetics of solid-state isotope-exchange reactions for  
1418 clumped isotopes: A study of inorganic calcites and apatites from natural and experimental  
1419 samples: *American Journal of Science*, v. 315, p. 363–411, doi: 10.2475/05.2015.01.

1420 Stumm, W., and Morgan, J.J., 1981, *Aquatic chemistry: an introduction emphasizing chemical*  
1421 *equilibria in natural waters*: New York, Wiley-Interscience, 583 p.

1422 Suarez, M.B., Passey, B.H., and Kaakinen, A., 2011, Paleosol carbonate multiple isotopologue  
1423 signature of active East Asian summer monsoons during the late Miocene and Pliocene:  
1424 *Geology*, v. 39, p. 1151–1154, doi: 10.1130/G32350.1.

1425 Tapponnier, P., Mercier, J.L., Proust, F., Andrieux, J., Armijo, R., Bassoulet, J.P., Brunel, M.,



- 1426 Burg, J.P., Colchen, M., Dupre, B., Girardeau, J., Marcoux, J., Mascle, G., Matte, P., et al.,  
1427 1981, The Tibetan side of the India-Eurasia collision: *Nature*, v. 294, p. 405–410.
- 1428 Tapponnier, P., Peltzer, G., and Armijo, R., 1986, On the mechanics of the collision between  
1429 India and Asia: Geological Society, London, Special Publications, v. 19, p. 113–157, doi:  
1430 10.1144/GSL.SP.1986.019.01.07.
- 1431 Tremblay, M., Fox, M., Schmidt, J.L., Tripathy-Lang, A., Wielicki, W., Harrison, T.M., Zeitler,  
1432 P.K., and Shuster, D.L., 2015, Erosion in Southern Tibet shut down at ~10 Ma due to  
1433 enhanced rock uplift within the Himalaya: *Proceedings of the National Academy of  
1434 Sciences*, v. 112, p. 12030–12035.
- 1435 Urey, H., 1952, *The Planets: Their Origin and Development*: New Haven, Yale University Press.
- 1436 Vasconcelos, C., McKenzie, J.A., Warthmann, R., and Bernasconi, S.M., 2005, Calibration of  
1437 the  $\delta 18\text{O}$  paleothermometer for dolomite precipitated in microbial cultures and natural  
1438 environments: *Geology*, v. 33, p. 317–320, doi: 10.1130/G20992.1.
- 1439 Wang, J., and Chen, Y., 1999, Sedimentary formation characteristics of hydrocarbon generation  
1440 and oil exploration prospects of Wuyu basin in Tibet: *Petroleum Exploration and  
1441 Development*, v. 26, p. 14–17.
- 1442 Wang, C., Dai, J., Zhao, X., Li, Y., Graham, S.A., He, D., Ran, B., and Meng, J., 2014, Outward-  
1443 growth of the Tibetan Plateau during the Cenozoic: A review: *Tectonophysics*, v. 621, p. 1–  
1444 43, doi: 10.1016/j.tecto.2014.01.036.
- 1445 Wang, Y., Deng, T., and Biasatti, D., 2006, Ancient diets indicate significant uplift of southern  
1446 Tibet after ca. 7 Ma: *Geology*, v. 34, p. 309–312, doi: 10.1130/G22254.1.
- 1447 Yue, Y., and Ding, L., 2006, Ar-40/Ar-39 Geochronology, geochemical characteristics and  
1448 genesis of the Linzhou basic dikes, Tibet.: *Acta Petrologica Sinica*, v. 22, p. 855–866.
- 1449 Zaarur, S., Affek, H.P., and Brandon, M.T., 2013, A revised calibration of the clumped isotope  
1450 thermometer: *Earth and Planetary Science Letters*, v. 382, p. 47–57, doi:  
1451 10.1016/j.epsl.2013.07.026.
- 1452 Zachos, J., Pagani, M., Sloan, L., Thomas, E., and Billups, K., 2001, Trends, rhythms, and  
1453 aberrations in global climate 65 Ma to Present: *Science*, v. 292, p. 686–693.
- 1454 Zhang, K.J., 2000, Cretaceous palaeogeography of Tibet and adjacent areas (China): tectonic  
1455 implications: *Cretaceous Research*, v. 21, p. 23–33, doi: 10.1006/cres.2000.0199.
- 1456 Zhang, C.L., Horita, J., Cole, D.R., Zhou, J., Lovley, D.R., and Phelps, T.J., 2001, Temperature-  
1457 dependent oxygen and carbon isotope fractionations of biogenic siderite: *Geochimica et  
1458 Cosmochimica Acta*, v. 65, p. 2257–2271, doi: 10.1016/S0016-7037(01)00596-8.
- 1459 Zhou, S., Mo, X.X., Zhao, Z.D., Qiu, R.Z., Niu, Y.L., Guo, T.Y., and Zhang, S.Q., 2010,  
1460 Biosynthetic origin of the saw-toothed profile in  $\delta 13\text{C}$  and  $\delta \text{D}$  of n-alkanes and systematic  
1461 isotopic differences between n-, iso- and anteiso-alkanes in leaf waxes of land plants:  
1462 *Journal of Asian Earth Sciences*, v. 37, p. 246–258.
- 1463 Zhu, Y., Fang, X., Gao, J., Yi, H., Wang, S., and Zhang, W., 2006, Oligo-Mioence depositional  
1464 facies of the Wuyu basin, southern Tibetan Plateau: *Acta Sedimentologica Sinica*, v. 24, p.  
1465 775–782.

1466  
1467

## 1468 **FIGURE CAPTIONS**

1469

1470 **Table 1. Stable isotope data for all carbonates and calculated paleo-elevations of the Penbo**  
1471 **Basin.** Calcite-water fractionation factors are calculated using the average primary  $T(\Delta_{47}) \pm 5^\circ\text{C}$ .  
1472 Samples are organized by carbonate type and approximate location in stratigraphic section by  
1473 correlating laterally extensive units between measured sections.  
1474

1475 **Table 2. Stable isotope data for all carbonates and calculated paleo-elevations of the Oiyug**  
1476 **Basin.**  $T(\Delta_{47})$  values used for carbonate-water oxygen isotope fractionation in each geologic  
1477 formation is presented above each table with mineral-specific fractionation factors. The  $T(\Delta_{47})$   
1478 value for each formation is calculated using the Zaarur et al. (2013) thermometer and the average  
1479 of  $\Delta_{47}$  measurements ( $\pm$ standard error of the mean [s.e.m.]) on primary calcite from the  
1480 formation. The error reported for  $\delta^{18}\text{O}_w$  is from the s.e.m. of the clumped isotope measurements  
1481 used to calculate temperature-dependent calcite-water fractionation factors.  
1482

1483 **Table 3. Stable isotope data for the subset of samples with  $\Delta_{47}$  measurements from both**  
1484 **basins.**  $\delta^{18}\text{O}$  and  $\delta^{13}\text{C}$  values were measured both on the gas bench ( $\text{CO}_2$  in tube headspace from  
1485  $\text{CO}_3$  dissolution in  $\sim 103\%$  phosphoric acid) and MAT253 ( $\text{CO}_2$  released from  $\text{CO}_3$  by  $>105\%$   
1486 phosphoric acid dissolution and passed through a series of water traps and a Haysep-Q  
1487 chromatographic column to remove contaminants). The Zaarur et al. (2013) thermometer was  
1488 applied to  $\Delta_{47}$  (CDES; Dennis et al., 2011) measurements.  
1489

1490 **Table 4. Summary of Ar/Ar and (U-Th)/He analytical measurements.**

1491 **Table 5. Petrographic thin sections of subset of samples from the Penbo Basin with**  
1492 **descriptions.** An initial assessment was made based on presence or non-presence of alteration  
1493 textures.  $T(\Delta_{47})$  values are included for the samples that were analyzed for  $\Delta_{47}$ .  
1494

1495 **Table 6. Petrographic thin sections of subset of samples from the Oiyug Basin with**  
1496 **descriptions.** An initial assessment was made based on presence or non-presence of alteration  
1497 textures.  $T(\Delta_{47})$  values are included.  
1498

1499 **Figure 1. Maps of the sampled regions. A.** Regional Landsat image of the Tibetan Plateau  
1500 (adapted from Currie et al., 2016). **B.** Geologic map of the Linzhou/Penbo region including the  
1501 Nianbo type section. Map is based on and geochronology sourced from Ding et al. (2014) and He  
1502 et al. (2007). **C.** Geologic map of the Oiyug basin displaying measured section locations from  
1503 Currie et al. (2016 ; gray) and this study (blue). The fossil floral locality of Spicer et al. (2003) is  
1504 depicted as a leaf.  
1505

1506 **Figure 2. Composite stratigraphic section of the Nianbo Formation in the Penbo Basin.** The  
1507 geographic location for the base of this section is  $29.999603^\circ\text{N}$ ,  $91.209293^\circ\text{E}$ . Coordinates for  
1508 other measured sections within the Nianbo Fm (blue rectangles, Fig. 1B) are  $29.9689^\circ\text{N}$ ,  
1509  $91.2147^\circ\text{E}$  and  $29.9715^\circ\text{N}$ ,  $91.1951^\circ\text{E}$ . The base of the Pana Fm measured section is located at  
1510  $30.0105^\circ\text{N}$ ,  $91.1470^\circ\text{E}$ .  
1511

1512 **Figure 3. Example of calcic paleosols from the lower Nianbo Formation. A.** Depth profile of  
1513 series of stacked paleosols developed in sandy alluvial mudstones at  $\sim 49$  m in Nianbo Fm  
1514 measured section (Fig. 2). Paleosols contain vertic features, root traces, insect burrows,

1515 pedogenic nodules and rhizocretions. Paleosols are interpreted as compound in nature with four  
1516 clay-rich horizons containing vertic features overlying related calcic horizons (stage III;  
1517 Machette, 1985). Uppermost vertic horizon is ~1 m thick. **B.** Outcrop photo of paleosol  
1518 described in 3A. **C.** Close up of pedogenic nodules and mudstone near the top of the upper  
1519 calcic horizon described in 3A.

1520

1521 **Figure 4. Stratigraphic section of the Nianbo Formation in the Oiyug Basin.** The geographic  
1522 location for the base of this section is 29.9594°N, 89.7414°E.

1523

1524 **Figure 5. Clumped isotope-derived paleotemperatures of A. samples from the Penbo Basin**  
1525 **with relative age, and B. samples from the Oiyug Basin.** Ages are based on location in  
1526 stratigraphic section and interbedded ashes.  $\Delta_{47}$  is reported in CDES (carbon dioxide equilibrium  
1527 scale) reference frame (Dennis et al., 2011). Error bars represent  $\pm 1\sigma$  of all replicate analyses of  
1528 each sample ( $n$  listed in Table 1).

1529

1530 **Figure 6. Paleocene-Eocene elevation reconstruction of the Penbo basin.** We use a modified  
1531 version of Rowley's (2007) paleoaltimetry model. The average of the "primary"  $\Delta_{47}$ -derived  
1532 temperatures for lacustrine and pedogenic was used for the  $\delta^{18}\text{O}_c$  to  $\delta^{18}\text{O}_w$  fractionation factors  
1533 for carbonates of like lithology. Symbols are indicative of lithology. Error bars represent  
1534 propagation of analytical (s.e.m.) and model error in quadrature. The mean elevation for each  
1535 formation is indicated by the black circle with vertical line. The vertical dashed line marks the  
1536 modern hypsometric mean elevation of the Penbo basin.

1537

1538 **Figure 7. Cenozoic elevation reconstruction of the Oiyug basin, southern Tibet.** Calculated  
1539 paleo-elevations and oxygen isotopic compositions of pedogenic, lacustrine/marl, and  
1540 groundwater calcite, and nodular siderite and dolomite are plotted relative to sample location in  
1541 stratigraphic section and age. Symbols are indicative of lithology. Ages are taken from  
1542 paleomagnetic (Chen et al., 2008) and radiometric data (Zhou et al., 2010), as well as one  
1543  $^{40}\text{Ar}/^{39}\text{Ar}$  age from this study. Error bars represent propagation of analytical (s.e.m.) and model  
1544 error in quadrature. The mean elevation for each formation is indicated by the black circle with  
1545 vertical line. The mean elevation derived from lacustrine and pedogenic calcites in the Gazhacun  
1546 Formation are plotted separately to visualize the isotopic enrichment of lacustrine dolomites and  
1547 calcites. The vertical dashed line marks the modern hypsometric mean elevation of the Oiyug  
1548 basin.

1549

1550 **Figure 8. The Cenozoic marine Sr isotope record in relation to source flux compositions.**  
1551 The major feature of the Cenozoic record of seawater  $^{87}\text{Sr}/^{86}\text{Sr}$  (plotted here using measured  
1552 values on planktonic forams; Misra and Froelich, 2012) is the steep climb in ratios from roughly  
1553 36-38 Ma to present. This is conventionally interpreted as reflecting the onset of uplift in the  
1554 India-Eurasia collision system with chemical weathering of radiogenic terrains (e.g., Raymo and  
1555 Ruddiman, 1992; Richter et al., 1992). The modern day isotopic composition of the Ganges-  
1556 Brahmaputra dissolved Sr flux is sufficiently high (e.g., Palmer and Edmond, 1992; Galy et al.,  
1557 1999; indicated on schematic) and sufficiently large that it shifts the modern global average river  
1558 input flux to high  $^{87}\text{Sr}/^{86}\text{Sr}$  ratios (e.g., Edmonds, 1992). This sustains the marine  $^{87}\text{Sr}/^{86}\text{Sr}$  ratio  
1559 at elevated values relative to the Paleogene. Our results indicate that the Linzizong Arc was  
1560 already at modern elevations in the late Paleocene and early Eocene. If chemical weathering

1561 rates were accelerated in these early stages of India-Eurasia collision, they likely would not have  
1562 exerted significant influence on the marine Sr isotope record, because the arc lithologies had  
1563 relatively nonradiogenic isotopic compositions (Mo et al., 2008). Major Cenozoic climate and  
1564 tectonic events are marked with arrows: Onset of India-Asia Collision (OIAC), Paleocene-  
1565 Eocene Thermal Maximum (PETM), Mid-Eocene Climatic Optimum (MECO), Mid-Miocene  
1566 Climatic Optimum (MMCO).  
1567  
1568

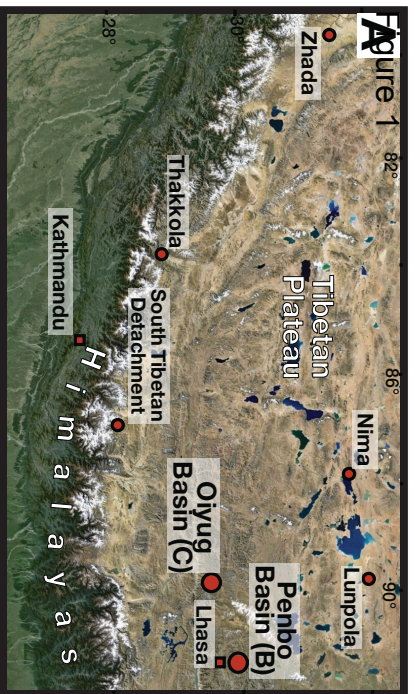
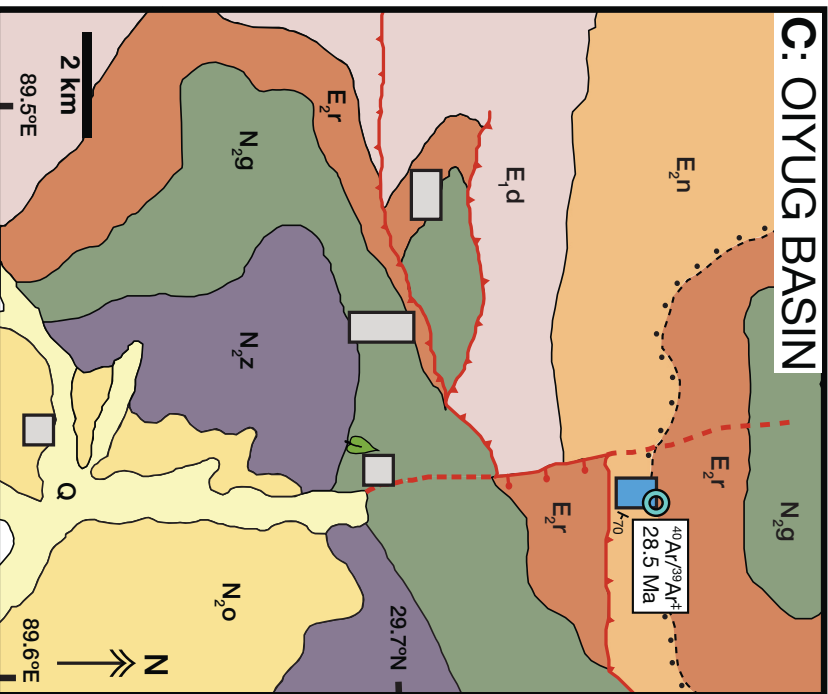
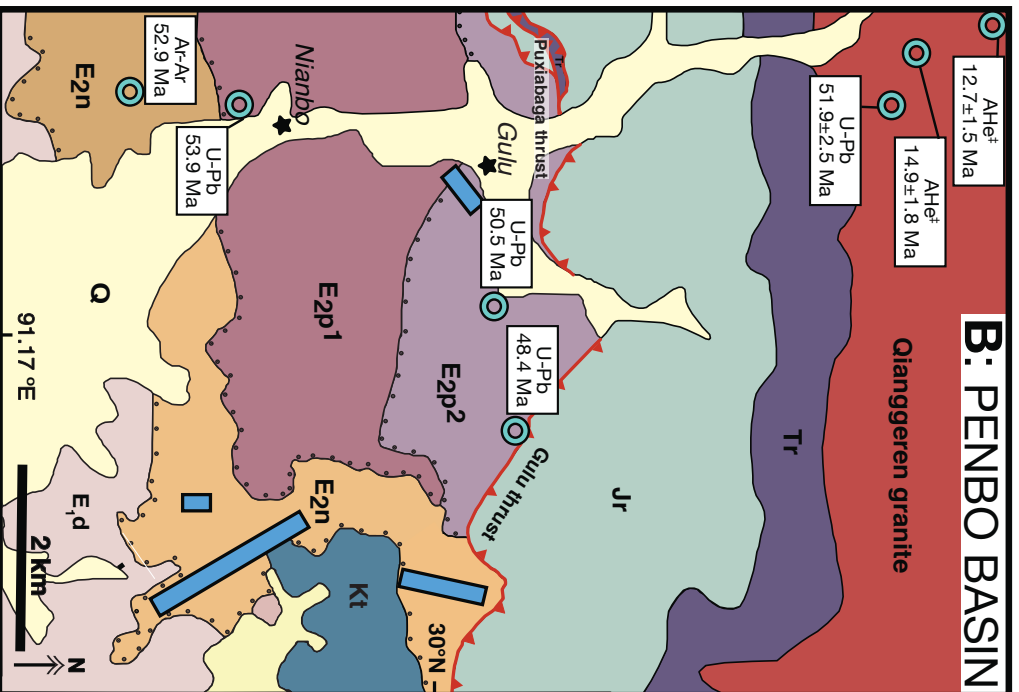


Figure 1

### C: OIYUG BASIN



### B: PENBO BASIN



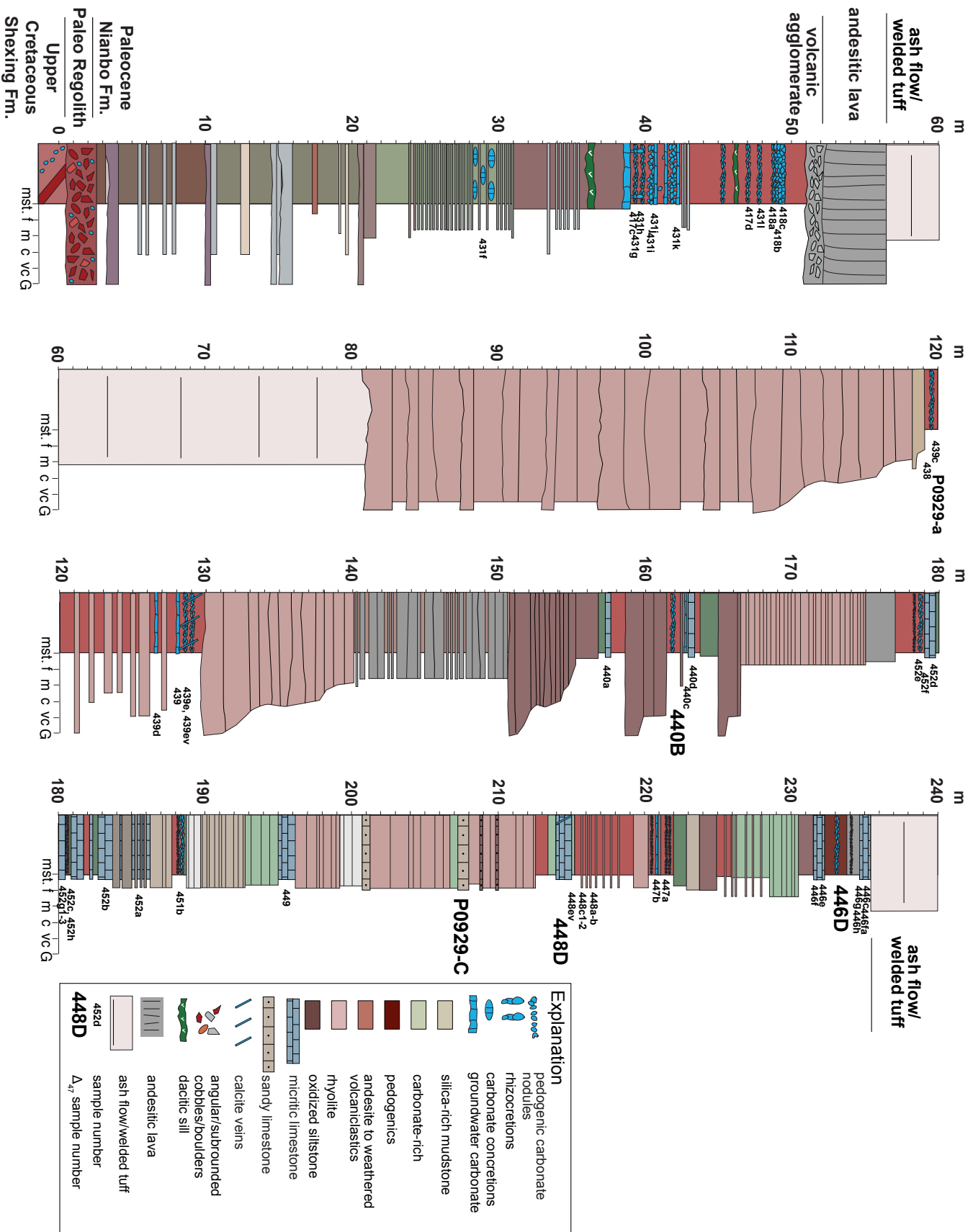
### Stratigraphy

Unit	Description
Q	Quaternary fluvial-valley fill deposits alluvium
<i>Linzizhong Group</i>	
N <sub>2</sub> o	Miocene-Pliocene Oiyug Fm lacustrine shale, mudstone, marl nodular siderite and calcite
N <sub>2</sub> z	Miocene Zongdang volcanics tuffaceous sandstone, conglomerates dacite, andesite, rhyolite
N <sub>2</sub> g	Miocene Gazhacun Fm tuffaceous sandstone, conglomerates dacite, andesite, rhyolite
E <sub>2</sub> r	Eocene-Oligocene Rigongla Fm alluvial fan and fluvial conglomerates, sandstones overbank mudstone; groundwater carbonate dacite
E <sub>2</sub> p <sup>1-2</sup>	Eocene Pana Fm thickly bedded sandstones and conglomerates andesite
E <sub>2</sub> n	Paleocene-Eocene Nianbo Fm groundwater and pedogenic carbonate highly weathered volcanics oxidized siltstone; sandy limestone sandstone interbedded with carbonate andesite; quartzite; rhyolite
E <sub>1</sub> d	Paleocene Dianzhong Fm thickly bedded basalts with interbedded ashes
Kt	Upper Cretaceous Takena Fm marine limestone
Jr	Jurassic clastic red beds
Tr	Triassic

### Explanation

- Reverse fault
- Uncertain location of unconformity
- Radiometric Age († = this study)
- Sampled Section Location, this study
- Currie et al., 2016 and this study
- Fossil Flora Location, Spicer et al., 2003

# Stratigraphic Log of the Nianbo Formation, Linzhou, Southern Tibet

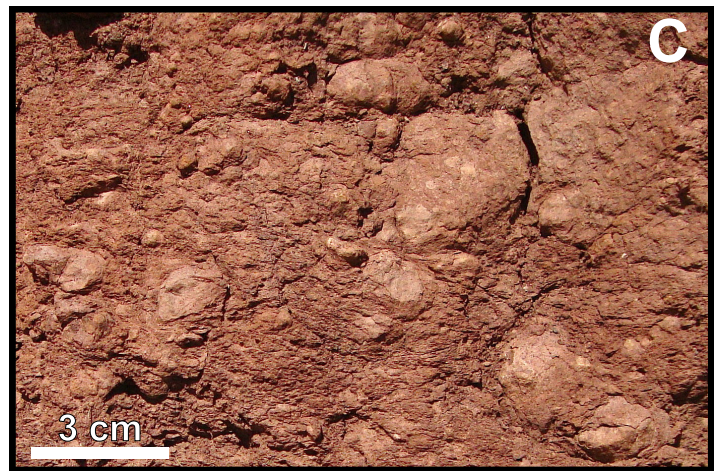
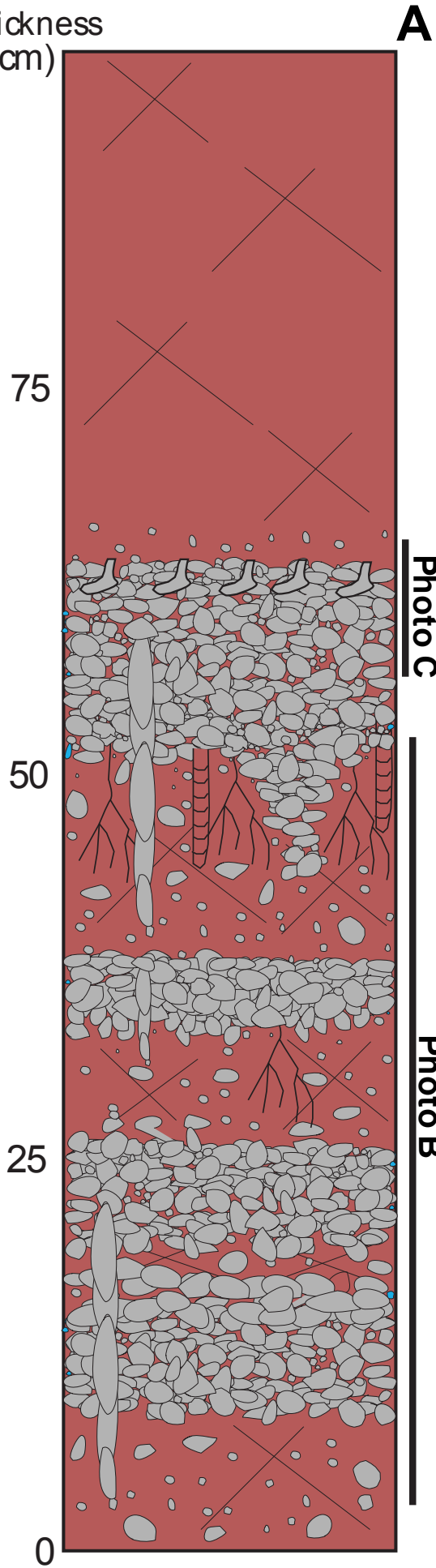


Explanation	
	pedogenic carbonate nodules
	rhizocretions
	carbonate concretions
	groundwater carbonate
	silica-rich mudstone
	carbonate-rich
	pedogenics
	andesite to weathered
	volcaniclastics
	rhyolite
	oxidized siltstone
	micritic limestone
	sandy limestone
	calcite veins
	angular/subrounded cobbles/boulders
	deccritic sill
	andesitic lava
	ash flow/welded tuff
	sample number
	sample number

Paleocene  
Nianbo Fm.  
Paleo Regolith  
Upper  
Cretaceous  
Shexing Fm.

Figure 3

Thickness  
(cm)

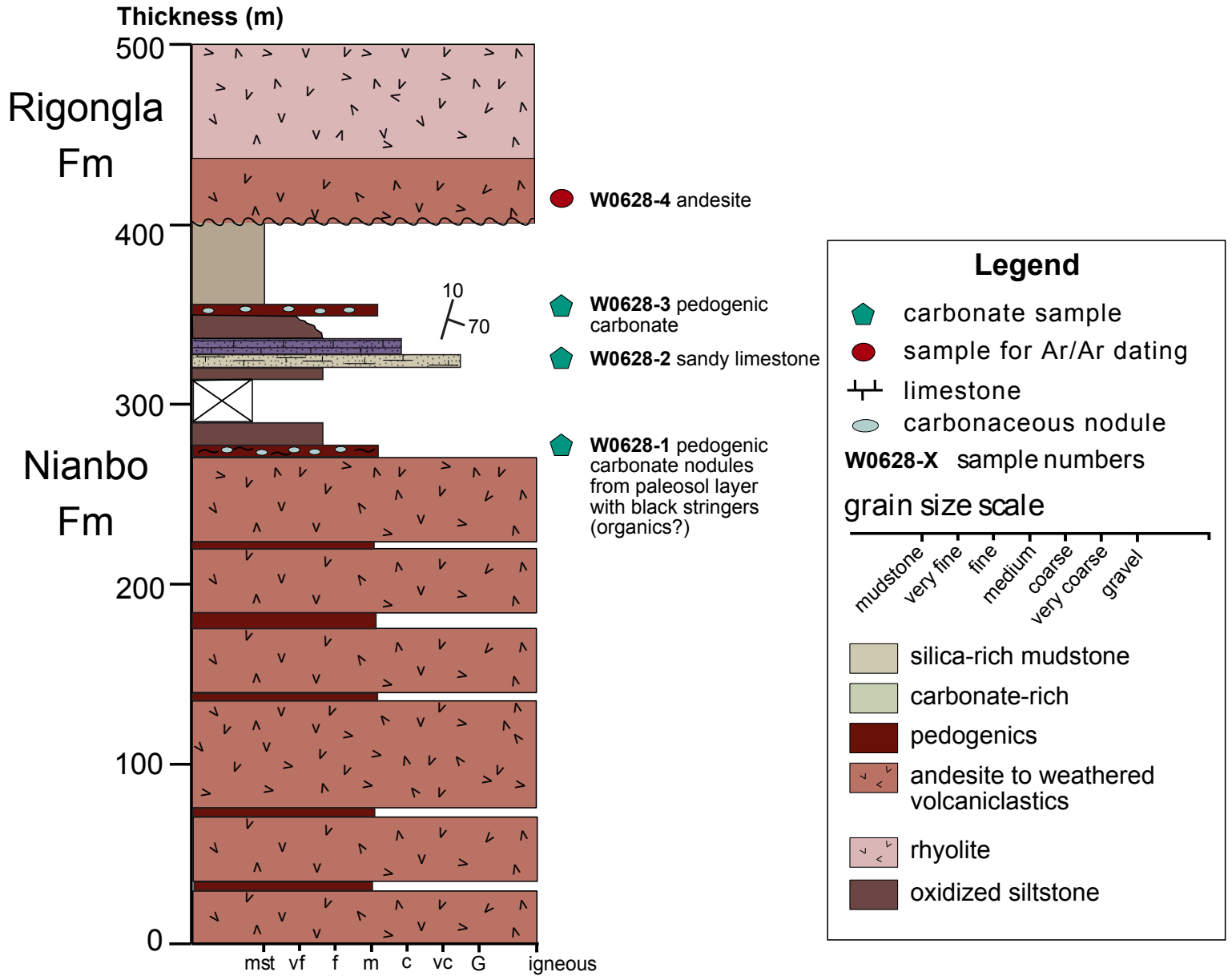


**Explanation**

- pedogenic carbonate nodules
- rhizcretions
- calcified hymenoptera brood cells
- MnO/day-coated slickensides
- root traces
- meniscate vertical burrows

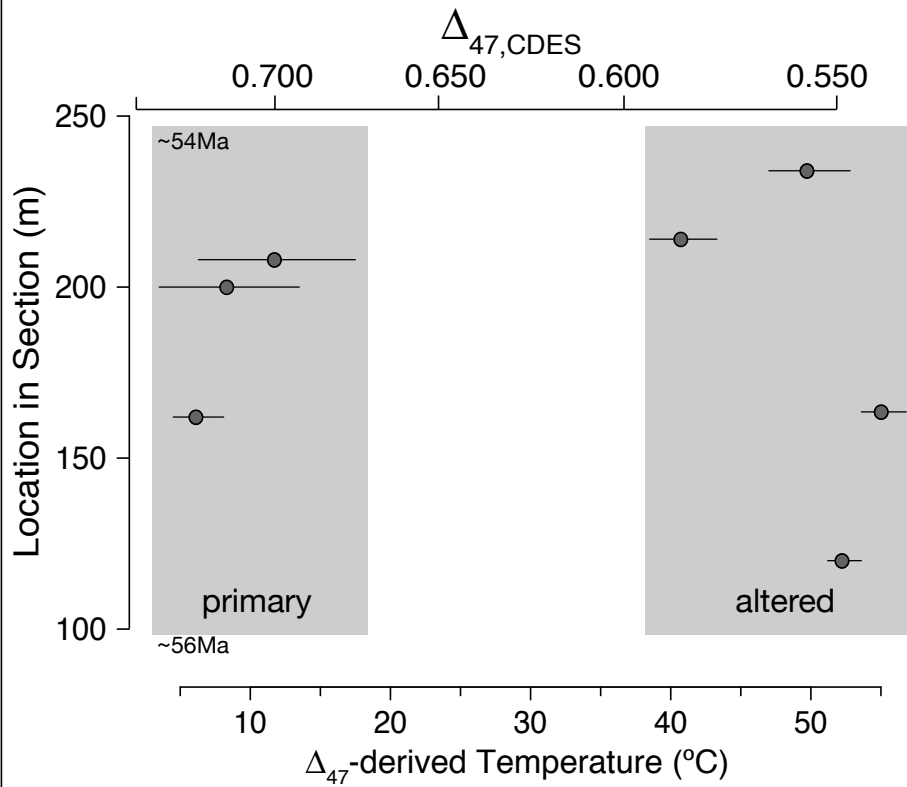
Figure 4

# Nianbo & Rigongla Formations, Oiyug Basin





### A. Penbo Basin, Nianbo Fm.



### B. Oiyug Basin

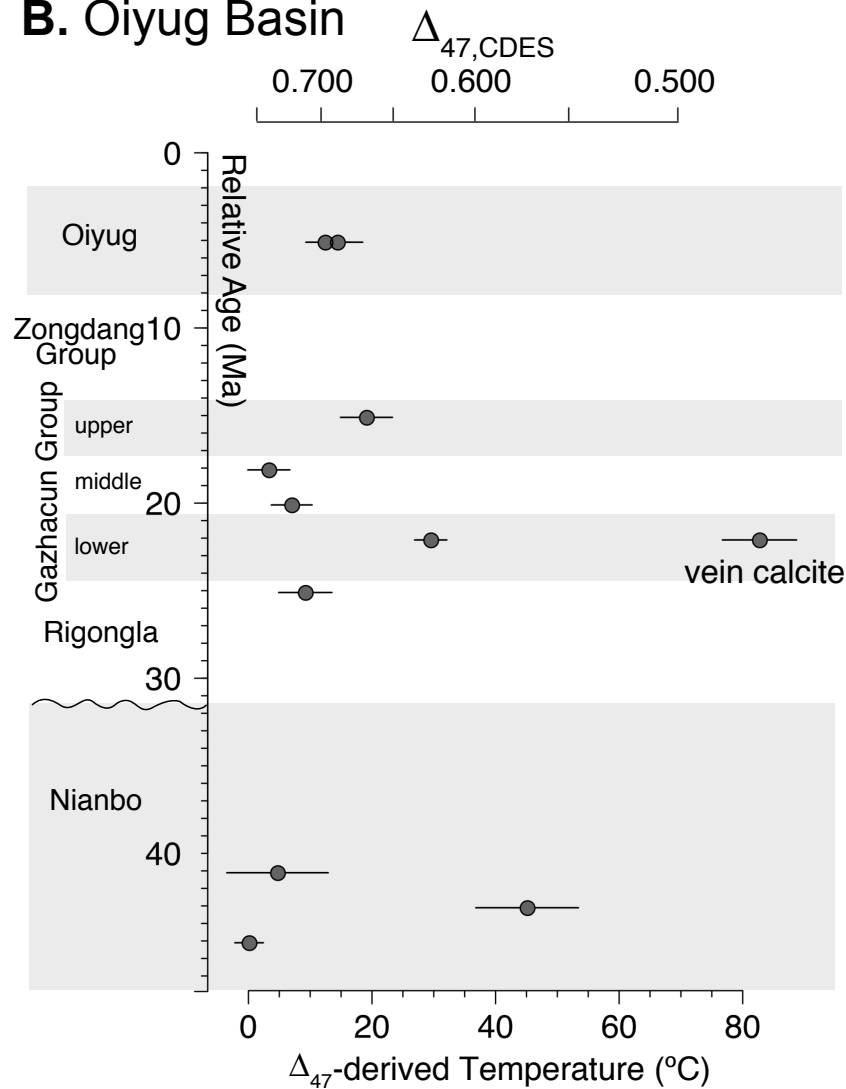


Figure 6

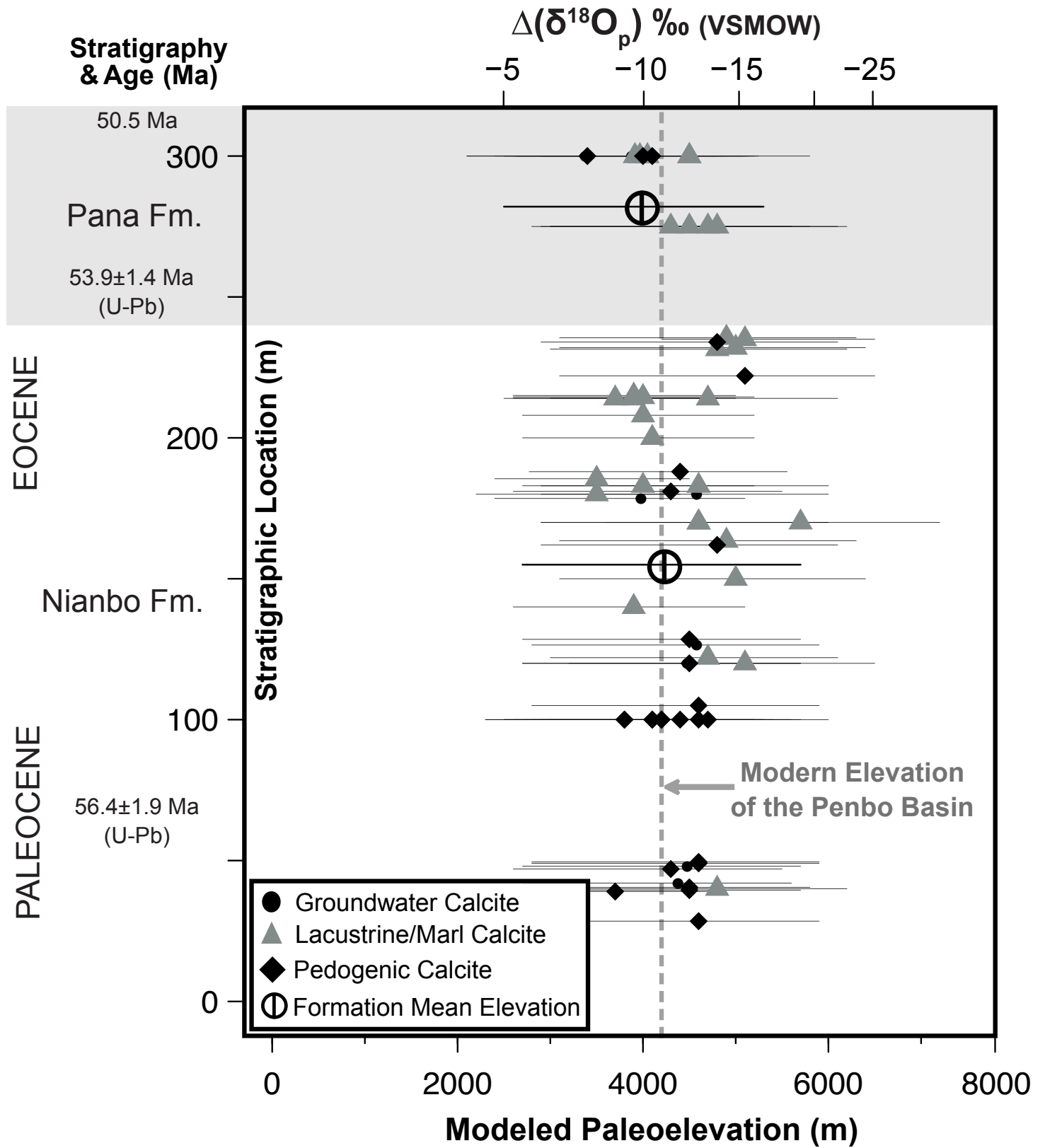


Figure 7

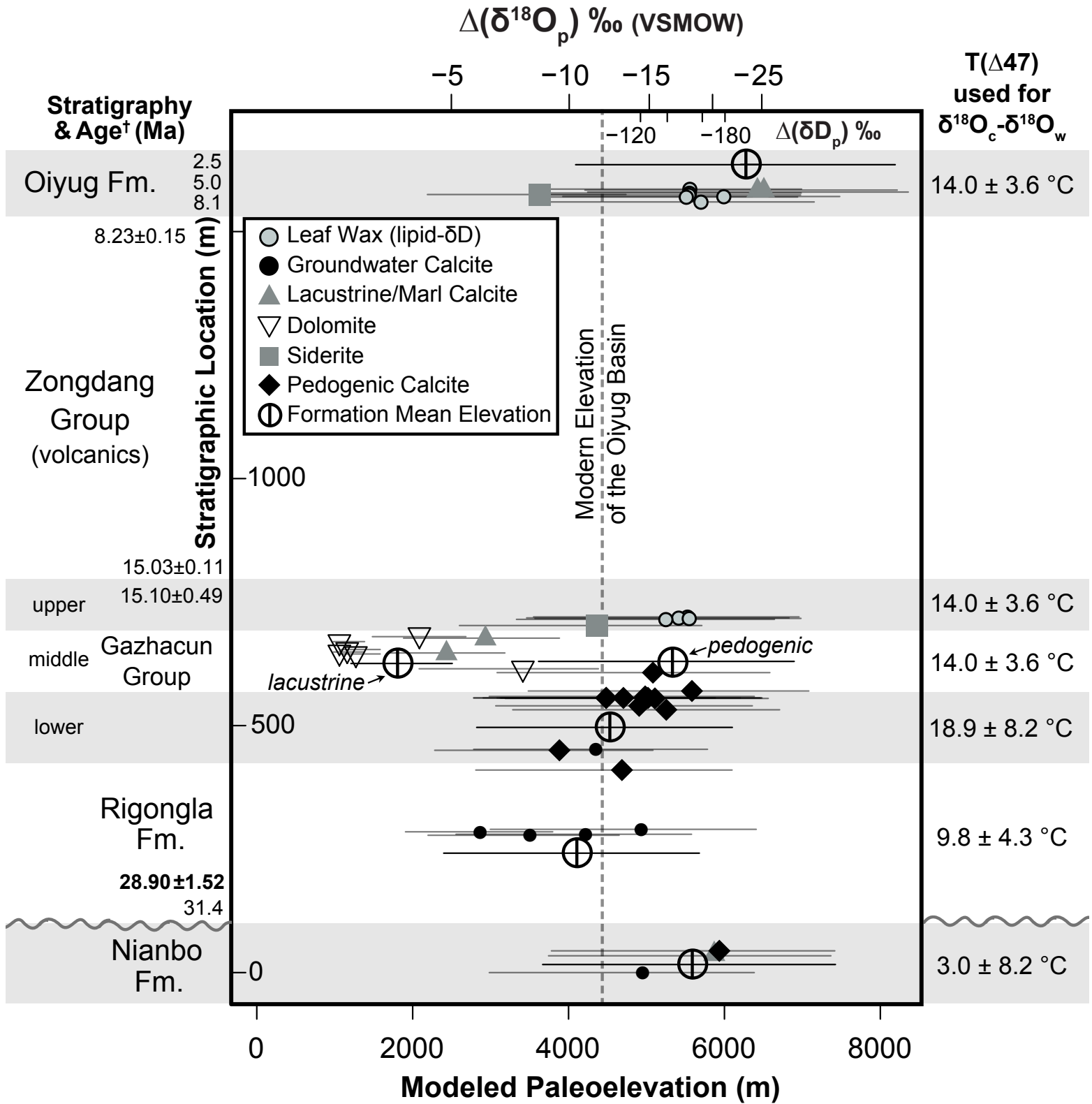


Figure 8

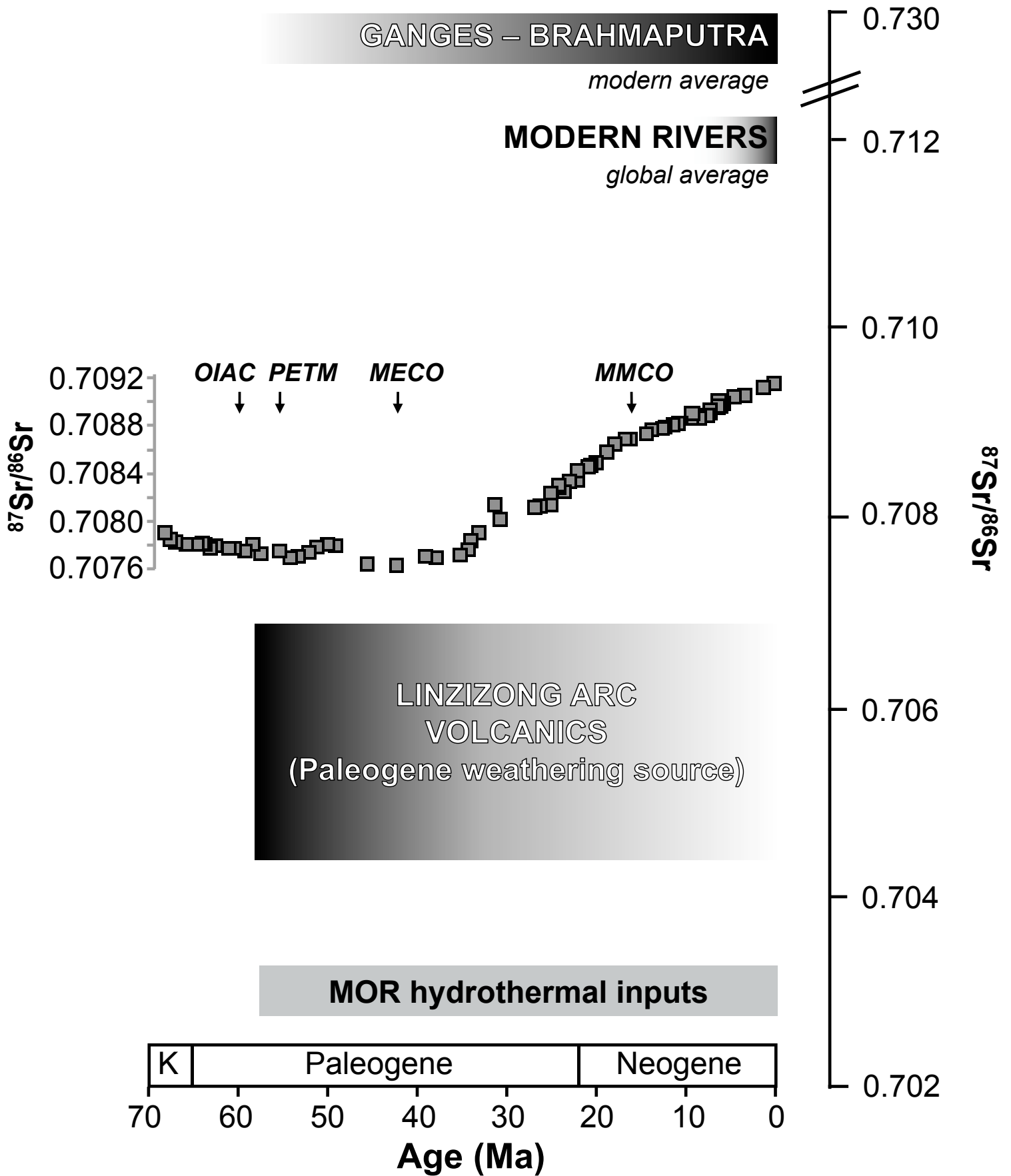


Table 1

**TABLE 1. STABLE ISOTOPE DATA FOR ALL CARBONATES AND CALCULATED PALEO-ELEVATIONS OF THE PENB**

		Lacustrine Carbonate		T( $\Delta_{47}$ )°C ( $\pm$ 5°C) : 10.2 °C 15.2 °C 5.2 °C					
				$\alpha$ (calcite-H <sub>2</sub> O) : 1.03170 1.03057 1.03288					
		Pedogenic Carbonate		T( $\Delta_{47}$ )°C ( $\pm$ 5°C) : 6.3 °C 8.1 °C 4.5 °C					
				$\alpha$ (calcite-H <sub>2</sub> O) : 1.03262 1.03219 1.03305					
Sample	Carbonate Type	Location in Section (m)	$\delta^{13}\text{C}$ (VPDB) (‰)	$\delta^{18}\text{O}_c$ (VPDB) (‰)	$\delta^{18}\text{O}_w$ (VSMOW) (‰)			mean $\delta^{18}\text{O}_w$ $\pm$ 2.2‰	$\otimes$ ( $\delta^{18}\text{O}_w$ ) (‰)
<b>Pana Formation</b>									
483C	lacustrine limestone	300	-7.6	-13.9	-14.7	-13.6	-15.8	-14.7 $\pm$ 2.2	-10.1
484A	lacustrine limestone	300	-7.2	-14.0	-14.9	-13.8	-16.0	-14.9 $\pm$ 2.2	-10.3
483D	lacustrine limestone	300	-6.3	-14.3	-15.2	-14.1	-16.3	-15.2 $\pm$ 2.2	-10.6
483B	lacustrine limestone	300	-7.5	-14.7	-15.5	-14.4	-16.6	-15.5 $\pm$ 2.2	-10.9
483A	lacustrine limestone	300	-7.3	-14.8	-15.6	-14.5	-16.7	-15.6 $\pm$ 2.2	-11.0
491B	groundwater calcite nodule	300	-6.6	-13.1	-14.8	-14.4	-15.2	-14.8 $\pm$ 0.8	-8.2
491C	groundwater calcite nodule	300	-5.8	-11.7	-13.4	-13.0	-13.8	-13.4 $\pm$ 0.8	-6.8
490A	paleosol carbonate nodule	300	-7.6	-14.1	-15.8	-15.4	-16.2	-15.8 $\pm$ 0.8	-9.2
490B	paleosol carbonate nodule	300	-7.2	-13.6	-15.2	-14.8	-15.7	-15.2 $\pm$ 0.8	-8.6
491A	paleosol carbonate nodule	300	-6.1	-11.7	-13.4	-13.0	-13.8	-13.4 $\pm$ 0.8	-6.8
475B	lacustrine limestone	275	-3.2	-13.7	-14.5	-13.5	-15.7	-14.6 $\pm$ 2.2	-10.0
475C	lacustrine limestone	275	-3.8	-14.4	-15.2	-14.2	-16.4	-15.3 $\pm$ 2.2	-10.7
475D	lacustrine limestone	275	-4.5	-15.4	-16.2	-15.1	-17.3	-16.2 $\pm$ 2.2	-11.6
475A	lacustrine limestone	275	-4.1	-16.1	-16.9	-15.8	-18.0	-16.9 $\pm$ 2.2	-12.3
								Mean Elevation (km)*	
<b>Nianbo Formation</b>									
446C	lacustrine limestone	236	-2.7	-16.7	-17.5	-16.5	-18.7	-17.6 $\pm$ 2.2	-13.0
446H	lacustrine limestone	235	<b>-2.2</b>	-17.9	-18.7	-17.7	-19.9	-18.7 $\pm$ 2.2	-14.1
446D	paleosol carbonate nodule	234	-4.6	-17.3	-18.9	-18.5	-19.4	-18.9 $\pm$ 0.8	-12.3
446F	lacustrine limestone	232	-3.5	-16.1	-16.9	-15.8	-18.0	-16.9 $\pm$ 2.2	-12.3
446E	lacustrine limestone	232	-3.2	-17.3	-18.1	-17.0	-19.2	-18.1 $\pm$ 2.2	-13.5
447A	paleosol carbonate nodule	222	-3.8	-19.0	-20.7	-20.3	-21.1	-20.7 $\pm$ 0.8	-14.1
448C	lacustrine limestone	215	<b>-3.8</b>	-12.7	-13.5	-12.4	-14.6	-13.5 $\pm$ 2.2	-8.9
448A	lacustrine limestone	215	-3.9	-12.0	-12.8	-11.7	-13.9	-12.8 $\pm$ 2.2	-8.2
448E	lacustrine limestone	214	-4.8	-11.4	-12.2	-11.1	-13.3	-12.2 $\pm$ 2.2	-7.6
448D	lacustrine limestone	214	-4.0	-12.0	-12.8	-11.7	-13.9	-12.8 $\pm$ 2.2	-8.2
448	lacustrine limestone	214	-3.5	-15.3	-16.2	-15.1	-17.3	-16.2 $\pm$ 2.2	-11.6
<b>P0929-c</b>	<b>lacustrine limestone</b>	<b>208</b>	<b>-3.3</b>	<b>-12.7</b>	<b>-13.1</b>	<b>-11.9</b>	<b>-14.4</b>	<b>-13.1 <math>\pm</math> 2.5</b>	<b>-8.6</b>
<b>DL104-3b</b>	<b>lacustrine limestone</b>	<b>200</b>	<b>-2.5</b>	<b>-12.4</b>	<b>-13.6</b>	<b>-12.5</b>	<b>-14.7</b>	<b>-13.6 <math>\pm</math> 2.2</b>	<b>-9.0</b>
451B	paleosol carbonate nodule	188	-2.7	-15.3	-17.0	-16.6	-17.4	-17.0 $\pm$ 0.8	-10.4
452A	lacustrine limestone	186	-4.0	-10.9	-11.7	-10.7	-12.9	-11.8 $\pm$ 2.2	-7.2
452B	lacustrine limestone	183	-3.7	-12.3	-13.1	-12.0	-14.3	-13.1 $\pm$ 2.2	-8.6
452D	lacustrine limestone	183	-3.5	-15.0	-15.8	-14.8	-17.0	-15.9 $\pm$ 2.2	-11.3
452C	paleosol carbonate nodule	181	-3.2	-14.8	-16.4	-16.0	-16.8	-16.4 $\pm$ 0.8	-9.8
452G1	lacustrine limestone	180	-3.5	-11.8	-13.5	-13.1	-13.9	-13.5 $\pm$ 0.4	-6.9
452G3	groundwater calcite nodule	180	-4.2	-16.0	-17.7	-17.2	-18.1	-17.7 $\pm$ 0.4	-11.1
452E	groundwater calcite nodule	179	-3.9	-13.8	-15.5	-15.0	-15.9	-15.5 $\pm$ 0.4	-8.9
514	lacustrine limestone	170	-2.1	-15.1	-15.9	-14.8	-17.0	-15.9 $\pm$ 2.2	-11.3
514A	lacustrine limestone	170	-2.0	-15.2	-16.0	-14.9	-17.1	-16.0 $\pm$ 2.2	-11.4
511	lacustrine limestone	170	-0.1	-21.8	-22.6	-21.5	-23.7	-22.6 $\pm$ 2.2	-18.0
440D	lacustrine limestone	164	-4.5	-16.3	-17.1	-16.0	-18.3	-17.1 $\pm$ 2.2	-12.5
<b>440B</b>	<b>paleosol carbonate nodule</b>	<b>162</b>	<b>-3.8</b>	<b>-17.2</b>	<b>-18.9</b>	<b>-18.5</b>	<b>-19.3</b>	<b>-18.9 <math>\pm</math> 0.8</b>	<b>-12.3</b>
505	lacustrine limestone	150	-0.2	-17.3	-18.1	-17.0	-19.2	-18.1 $\pm$ 2.2	-13.5
508	lacustrine limestone	140	-3.8	-12.3	-13.1	-12.0	-14.2	-13.1 $\pm$ 2.2	-8.5
439E	paleosol carbonate nodule	129	-4.6	-15.8	-17.5	-17.1	-17.9	-17.5 $\pm$ 0.8	-10.9
439D	groundwater calcite nodule	127	-4.3	-16.3	-18.0	-17.6	-18.4	-18.0 $\pm$ 0.8	-11.4
456	lacustrine limestone	122	-3.7	-15.5	-16.3	-15.2	-17.4	-16.3 $\pm$ 2.2	-11.7
504A	lacustrine limestone	120	-0.7	-17.8	-18.6	-17.5	-19.7	-18.6 $\pm$ 2.2	-14.0
439	groundwater calcite nodule	120	-5.2	-15.6	-17.3	-16.9	-17.7	-17.3 $\pm$ 0.8	-10.7
439C	paleosol carbonate nodule	120	-5.4	-15.5	-17.2	-16.8	-17.6	-17.2 $\pm$ 0.8	-10.6
523	paleosol carbonate nodule	105	-3.4	-16.3	-17.9	-17.5	-18.4	-18.0 $\pm$ 0.8	-11.4
512	paleosol carbonate nodule	100	-3.5	-15.1	-16.8	-16.3	-17.2	-16.8 $\pm$ 0.8	-9.6
534A	paleosol carbonate nodule	100	-5.8	-14.5	-16.1	-15.7	-16.6	-16.1 $\pm$ 0.8	-9.5
534C	paleosol carbonate nodule	100	-5.3	-15.4	-17.1	-16.7	-17.5	-17.1 $\pm$ 0.8	-10.5
534D	paleosol carbonate nodule	100	-6.7	-12.8	-14.5	-14.1	-14.9	-14.5 $\pm$ 0.8	-7.9
534F	paleosol carbonate nodule	100	-3.3	-14.3	-16.0	-15.6	-16.4	-16.0 $\pm$ 0.8	-9.4
534G	paleosol carbonate nodule	100	-2.8	-16.3	-17.9	-17.5	-18.3	-17.9 $\pm$ 0.8	-11.3
534I	paleosol carbonate nodule	100	-4.5	-13.8	-15.5	-15.1	-15.9	-15.5 $\pm$ 0.8	-8.9
534J	paleosol carbonate nodule	100	-6.1	-14.2	-15.9	-15.5	-16.3	-15.9 $\pm$ 0.8	-9.3
534K	paleosol carbonate nodule	100	-5.5	-12.8	-14.5	-14.1	-14.9	-14.5 $\pm$ 0.8	-7.9
534L	paleosol carbonate nodule	100	-3.5	-16.7	-18.3	-17.9	-18.7	-18.3 $\pm$ 0.8	-11.7
418B	paleosol carbonate nodule	50	-7.0	-16.2	-17.9	-17.5	-18.3	-17.9 $\pm$ 0.8	-11.3
418A	paleosol carbonate nodule	49	-7.1	-16.1	-17.8	-17.4	-18.2	-17.8 $\pm$ 0.8	-11.2

431L	groundwater calcite nodule	48	-8.5	-15.6	-17.2	-16.8	-17.6	-17.2 ± 0.8	-10.6
417D	paleosol carbonate nodule	47	-10.4	-14.9	-16.6	-16.1	-17.0	-16.6 ± 0.8	-10.0
431K	groundwater calcite nodule	42	-8.9	-15.2	-16.9	-16.5	-17.3	-16.9 ± 0.8	-10.3
431I	paleosol carbonate nodule	41	-8.7	-15.9	-17.6	-17.2	-18.0	-17.6 ± 0.8	-11.0
431H	lacustrine limestone	40	-8.8	-16.0	-16.8	-15.8	-18.0	-16.9 ± 2.2	-12.3
431G	paleosol carbonate nodule	40	-7.2	-15.7	-17.4	-17.0	-17.8	-17.4 ± 0.8	-10.8
417C	paleosol carbonate nodule	39	-10.4	-12.6	-14.3	-13.9	-14.7	-14.3 ± 0.8	-7.7
431F	paleosol carbonate nodule	29	-6.6	-16.0	-17.6	-17.2	-18.1	-17.7 ± 0.8	-11.1
								<b>Mean Elevation (km)*</b>	

The unique  $T(\Delta_{47})$  values from clumped isotope samples (bold) were used to calculate the calcite-water fractionation for those samples. The average  $T(\Delta_{47})$  for pedogeni clumped isotope samples were used to calculate the appropriate calcite-water fractionation for the remaining samples, by sample type.

\* Error estimates for mean elevations are reported as the quadrature of the model error for each elevation estimate.

O BASIN

---

---

Model Elevation  
(km)  $\pm 2\sigma$

---

---

3.9 +1.1/-1.3  
4.0 +1.1/-1.3  
4.0 +1.2/-1.3  
4.5 +1.3/-1.6  
4.5 +1.3/-1.7  
3.9 +1.0/-1.5  
3.4 +0.8/-1.3  
4.1 +1.1/-1.6  
4.0 +1.1/-1.5  
3.4 +0.8/-1.3  
4.3 +1.3/-1.5  
4.5 +1.3/-1.6  
4.7 +1.4/-1.7  
4.8 +1.4/-1.8  
**4.1 +1.2/-1.6**

4.9 +1.4/-1.8  
5.1 +1.4/-1.9  
4.8 +1.3/-1.9  
4.8 +1.4/-1.8  
5.0 +1.4/-1.9  
5.1 +1.4/-2.0  
4.0 +1.2/-1.4  
3.9 +1.1/-1.3  
3.7 +1.1/-1.2  
3.9 +1.1/-1.3  
4.7 +1.4/-1.7  
**4.0 +1.2/-1.3**  
**4.1 +1.2/-1.4**  
4.4 +1.2/-1.7  
3.5 +1.0/-1.1  
4.0 +1.2/-1.3  
4.6 +1.4/-1.7  
4.3 +1.2/-1.7  
3.5 +0.9/-1.3  
4.6 +1.3/-1.8  
4.0 +1.1/-1.6  
4.6 +1.4/-1.7  
4.6 +1.4/-1.7  
5.7 +1.5/-2.1  
4.9 +1.4/-1.8  
**4.8 +1.3/-1.9**  
5.0 +1.4/-1.9  
3.9 +1.2/-1.3  
4.5 +1.2/-1.8  
4.6 +1.3/-1.8  
4.7 +1.4/-1.7  
5.1 +1.4/-1.9  
4.5 +1.2/-1.8  
4.5 +1.2/-1.8  
4.6 +1.3/-1.8  
4.2 +1.2/-1.4  
4.2 +1.1/-1.7  
4.4 +1.2/-1.7  
3.8 +1.0/-1.5  
4.2 +1.1/-1.6  
4.6 +1.1/-1.6  
4.1 +1.1/-1.6  
4.1 +1.1/-1.6  
3.8 +1.0/-1.5  
4.7 +1.3/-1.8  
4.6 +1.3/-1.8  
4.6 +1.3/-1.8

4.5 +1.2/-1.8

4.3 +1.2/-1.7

4.4 +1.2/-1.7

4.5 +1.3/-1.8

4.8 +1.4/-1.8

4.5 +1.2/-1.8

3.7 +1.0/-1.4

4.6 +1.3/-1.8

**4.4 +1.3/-1.7**

ic and lacustrine



Table 2

**TABLE 2. STABLE ISOTOPE DATA FOR ALL CARBONATES AND CALCULATED PALEO-ELEVATIONS OF THE OIYUG BASIN.**

Oiyug Formation (Fm.)			$^{11}\text{T}(\Delta_{47})^{\circ}\text{C} (\pm 3.6^{\circ}\text{C})$ : 14.0 °C 17.6 °C 10.4 °C							
			$\alpha$ (siderite-H <sub>2</sub> O) : 1.03328 1.03252 1.03413							
Sample	Carbonate Type	Location in Section (m)	$\delta^{13}\text{C}$ (VPDB) (‰)	$\delta^{18}\text{O}_c$ (VPDB) (‰)	$\delta^{18}\text{O}_w$ (VSMOW) (‰)			mean $\delta^{18}\text{O}_w$ $\pm 2$ (‰)	$\delta^{18}\text{O}_w$ (‰)	Model Elevation (km) $\pm 2\sigma$
621I	calcite marl	1580	1.3	-28.0	-30.1	-29.4	-30.8	-30.1 $\pm$ 1.5	-25.5	6.5 +1.8/-2.3
621H	calcite marl	1584	-0.1	-27.4	-29.9	-29.1	-30.7	-29.9 $\pm$ 1.6	-25.3	6.5 +1.8/-2.3
621F	siderite nodule	1575	12.9	-10.8	-13.1	-12.4	-14.0	-13.2 $\pm$ 1.5	-8.6	3.6 +1.1/-1.4
									Mean Elevation (km)*	6.5 +1.8/-2.3
Upper Gazhacun Fm.			$^{11}\text{T}(\Delta_{47})^{\circ}\text{C} (\pm 3.6^{\circ}\text{C})$ : 14.0 °C 17.6 °C 10.4 °C							
			$\alpha$ (siderite-H <sub>2</sub> O) : 1.03328 1.03252 1.03413							
Sample	Carbonate Type	Location in Section (m)	$\delta^{13}\text{C}$ (VPDB) (‰)	$\delta^{18}\text{O}_c$ (VPDB) (‰)	$^{18}\text{O}_w$ (VSMOW) (‰)			mean $^{18}\text{O}_w$ $\pm 1.7$ ‰	$\delta^{18}\text{O}_w$ (‰)	Model Elevation (km) $\pm 2\sigma$
618A	siderite nodule	690	4.2	-17.1	-18.2	-17.4	-19.1	-18.3	-11.7	4.4 +1.3/-1.8
Middle Gazhacun Fm.			$^{11}\text{T}(\Delta_{47})^{\circ}\text{C} (\pm 3.6^{\circ}\text{C})$ : 14.0 °C 17.6 °C 10.4 °C							
			$\alpha$ (dolomite-H <sub>2</sub> O) : 1.03393 1.03312 1.03484							
			$\alpha$ (calcite-H <sub>2</sub> O) : 1.03084 1.03007 1.03169							
Sample	Carbonate Type	Location in Section (m)	$\delta^{13}\text{C}$ (VPDB) (‰)	$\delta^{18}\text{O}_c$ (VPDB) (‰)	$\delta^{18}\text{O}_w$ (VSMOW) (‰)			mean $\delta^{18}\text{O}_w$ $\pm 2$ (‰)	$\delta^{18}\text{O}_w$ (‰)	Model Elevation (km) $\pm 2\sigma$
555	pedogenic calcite	670	-5.8	-20.0	-21.6	-20.8	-22.6	-21.7 $\pm$ 1.8	-15.1	5.1 +1.5/-2.0
W8	dolomite nodule	680	-7.3	-7.6	-10.5	-9.8	-11.4	-10.6 $\pm$ 1.6	-4.0	2.1 +0.6/-0.6
553	calcareous shale	677	-3.8	-13.0	-11.8	-10.9	-12.7	-11.8 $\pm$ 1.6	-5.2	3.0 +0.9/-1.1
W7	dolomite nodule	670	-5.4	-5.5	-8.5	-7.7	-9.3	-8.5 $\pm$ 1.7	-1.9	1.1 +0.3/-0.1
W3	dolomite nodule	654	-6.3	-5.7	-8.7	-7.9	-9.5	-8.7 $\pm$ 1.6	-2.1	1.2 +0.4/-0.1
W2	dolomite nodule	649	-5.1	-5.5	-8.5	-7.7	-9.3	-8.5 $\pm$ 1.7	-1.9	1.1 +0.3/-0.1
551	calcareous mudstone	647	-2.5	-11.6	-11.6	-10.9	-12.4	-11.6 $\pm$ 1.6	-5.0	2.5 +0.7/-0.8
W1	dolomite nodule	645	-5.4	-5.8	-8.8	-8.0	-9.6	-8.8 $\pm$ 1.6	-2.2	1.3 +0.3/-0.2
550	dolomite nodule	615	-11.3	-11.3	-14.2	-13.5	-15.1	-14.3 $\pm$ 1.6	-7.7	3.4 +1.0/-1.3
554B	pedogenic calcite	570	-7.8	-19.7	-25.0	-24.2	-25.9	-25.0 $\pm$ 1.7	-18.4	5.6 +1.5/-2.1
									Pedogenic-derived Mean Elev. (km)*	5.3 +1.5/-2.0
									Lacustrine-derived Mean Elev. (km)*	2.0 +0.6/-0.7
Lower Gazhacun Fm.			$^{11}\text{T}(\Delta_{47})^{\circ}\text{C} (\pm 8.2^{\circ}\text{C})$ : 18.9 °C 27.1 °C 10.7 °C							
			$\alpha$ (calcite-H <sub>2</sub> O) : 1.03279 1.03105 1.03477							
Sample	Carbonate Type	Location in Section (m)	$\delta^{13}\text{C}$ (VPDB) (‰)	$\delta^{18}\text{O}_c$ (VPDB) (‰)	$\delta^{18}\text{O}_w$ (VSMOW) (‰)			mean $\delta^{18}\text{O}_w$ $\pm 2$ (‰)	$\delta^{18}\text{O}_w$ (‰)	Model Elevation (km) $\pm 2\sigma$
548	pedogenic calcite	559	-8.0	-20.1	-21.5	-20.8	-22.2	-21.5 $\pm$ 1.5	-14.9	5.0 +1.4/-2.0
165Ca	pedogenic calcite	556	-6.9	-19.8	-18.7	-17.1	-20.5	-18.8 $\pm$ 3.4	-12.2	4.5 +1.4/-1.7
165D	pedogenic calcite	556	-7.1	-20.0	-18.9	-17.3	-20.7	-19.0 $\pm$ 3.4	-12.4	4.5 +1.4/-1.7
165Fa	pedogenic calcite	556	-6.9	-19.7	-18.6	-17.0	-20.4	-18.7 $\pm$ 3.4	-15.0	5.0 +1.5/-1.9
165Fb	pedogenic calcite	556	-6.8	-19.7	-18.6	-17.0	-20.4	-18.7 $\pm$ 3.4	-15.0	5.0 +1.5/-1.9
165Fc	pedogenic calcite	556	-5.9	-18.0	-16.9	-15.3	-18.7	-17.0 $\pm$ 3.4	-13.3	4.7 +1.5/-1.8
165G	pedogenic calcite	556	-6.8	-19.6	-18.5	-16.9	-20.3	-18.6 $\pm$ 3.4	-14.9	5.0 +1.5/-1.9
R2	pedogenic calcite	555	-7.0	-20.2	-19.1	-17.5	-20.9	-19.2 $\pm$ 3.4	-15.5	5.1 +1.5/-1.9
547	pedogenic calcite	540	-6.0	-19.1	-18.0	-16.4	-19.8	-18.1 $\pm$ 3.4	-14.4	4.9 +1.5/-1.8
546	pedogenic calcite	532	-6.4	-21.1	-20.0	-18.4	-21.8	-20.0 $\pm$ 3.4	-16.4	5.3 +1.5/-2.0
543B	groundwater calcite	452	-3.3	-19.5	-18.5	-16.8	-20.3	-18.5 $\pm$ 3.4	-11.9	4.4 +1.4/-1.6
543A	pedogenic calcite	450	-7.6	-19.4	-16.1	-15.7	-16.7	-16.2 $\pm$ 1.0	-9.6	3.9 +1.2/-1.6
									Mean Elevation (km)*	4.5 +1.5/-1.7
Rigongla Fm.			$^{11}\text{T}(\Delta_{47})^{\circ}\text{C} (\pm 4.3^{\circ}\text{C})$ : 9.8 °C 14.1 °C 5.5 °C							
			$\alpha$ (calcite-H <sub>2</sub> O) : 1.03180 1.03081 1.03281							
Sample	Carbonate Type	Location in Section (m)	$\delta^{13}\text{C}$ (VPDB) (‰)	$\delta^{18}\text{O}_c$ (VPDB) (‰)	$\delta^{18}\text{O}_w$ (VSMOW) (‰)			mean $\delta^{18}\text{O}_w$ $\pm 2$ (‰)	$\delta^{18}\text{O}_w$ (‰)	Model Elevation (km) $\pm 2\sigma$
579	pedogenic calcite	410	-6.2	-18.9	-19.8	-18.9	-20.8	-19.8	-13.2	4.7 +1.4/-1.9
576	groundwater calcite	290	-3.4	-20.4	-21.3	-20.4	-22.3	-21.3	-14.7	5.0 +1.4/-2.0
575E	groundwater calcite	285	-3.7	-11.9	-12.8	-11.8	-13.7	-12.8	-6.2	2.9 +0.9/-1.0

575C	groundwater calcite	280	-2.6	-16.8	-17.7	-16.8	-18.7	-17.7	-11.1	4.3 +1.3/-1.7	
575B	groundwater calcite	278	-3.8	-13.9	-14.8	-13.9	-15.8	-14.8	-8.2	3.6 +1.1/-1.3	
Mean Elevation (km)*										4.1 +1.3/-1.6	
Nianbo Fm.			††T(Δ <sub>47</sub> )°C (± 8.2°C) :			3.0 °C	11.2 °C	-5.2 °C			
			α (calcite-H <sub>2</sub> O) :			1.03342	1.03147	1.03548			
Sample	Carbonate Type	Location in Section (m)	δ <sup>13</sup> C (VPDB) (‰)	†δ <sup>18</sup> O <sub>c</sub> (VPDB) (‰)	δ <sup>18</sup> O <sub>w</sub> (VSMOW) (‰)			mean δ <sup>18</sup> O <sub>w</sub> ±2 (‰)	‡Δ(δ <sup>18</sup> O <sub>w</sub> ) (‰)	Model Elevation (km) ±2σ	
<b>W0628-3</b>	<b>paleosol</b>	<b>44</b>	<b>-1.5</b>	<b>-24.9</b>	<b>-26.8</b>	<b>-25.0</b>	<b>-28.7</b>	<b>-26.8 ± 3.7</b>	<b>-20.2</b>	<b>5.9 +1.5/-2.1</b>	
W0628-2	lacustrine limestone	34	-4.1	-24.6	-27.0	-25.2	-29.0	-27.0 ± 3.8	-20.4	5.9 +1.5/-2.1	
<b>W0628-1</b>	<b>paleosol</b>	<b>0</b>	<b>-3.5</b>	<b>-18.6</b>	<b>-21.6</b>	<b>-21.0</b>	<b>-22.1</b>	<b>-21.6 ± 1.1</b>	<b>-15.0</b>	<b>5.0 +1.4/-2.0</b>	
Mean Elevation (km) ±										5.6 +1.5/-2.1	

Note: Samples with Δ<sub>47</sub> measurements are in bold. For these samples, their unique T(Δ<sub>47</sub>) was used to calculate δ<sup>18</sup>O<sub>w</sub>.

† †δ<sup>18</sup>O<sub>c</sub> of all samples except the Nianbo Fm have been previously published in Currie et al. (2005) and Currie et al. (2016). All †δ<sup>18</sup>O<sub>w</sub> values are calculated using new T(Δ<sub>47</sub>) measurements.

†† Temperature error is reported as the standard error of the mean of all clumped isotope measurements from that formation or sample type.

‡ low elevation †δ<sup>18</sup>O<sub>w</sub> values: -6.6‰ for Rigongla and Gazhacun Fms; -4.6‰ for Oiyug Fm, based on WMMTs derived from Khan et al. (2014) and Siwalik Fm paleosol carbonate data (Quade and Cerling, 1995; Quade et al., 2013)

+ Temperature used for dolomite-water and calcite-water fractionation factors of lacustrine samples is the average of lacustrine calcite clumped isotope temperatures, as these would have the most similar depositional conditions.

\* Error estimates for mean elevations are reported as the quadrature of the model error for each elevation estimate.

#### Water-Carbonate Oxygen Fractionation Factors

calcite/water  $\zeta = \text{EXP}(((18.03 * 10^3/T)-32.42)/1000)$  (Kim & O'Neil, 1997)

siderite/water  $\zeta = \text{EXP}(((2.62 * 10^6/T^2)-2.17)/1000)$  (Zhang et al., 2001)

dolomite/water  $\zeta = \text{EXP}(((2.73 * 10^6/T^2)+0.26)/1000)$  (Vasconcelos et al. 2005)

Oiyug Formation

Sample	Carbonate Type	Location in Section (m)	$\delta^{13}\text{C}$ (VPDB) (‰)	$\delta^{18}\text{O}_c$ (VPDB) (‰)	mean $\delta^{18}\text{O}_w$ $\pm 2$ (‰)	$\Delta(\delta^{18}\text{O}_w)$ (‰)	Model Elevation (km) $\pm 2\sigma$
621I	calcite marl	1580	1.3	-28.0	-30.1 $\pm$ 1.5	-25.5	6.5 +1.8/-2.3
621H	calcite marl	1584	-0.1	-27.4	-29.9 $\pm$ 1.6	-25.3	6.5 +1.8/-2.3
621F	siderite nodule	1575	12.9	-10.8	-13.2 $\pm$ 1.5	-8.6	3.6 +1.1/-1.4
Mean Elevation (km)*							6.5 +1.8/-2.3

Upper Gazhacun Fm.

618A	siderite nodule	690	4.2	-17.1	-18.3	-11.7	4.4 +1.3/-1.8
------	-----------------	-----	-----	-------	-------	-------	---------------

Lower Gazhacun Fm.

555	pedogenic calcite	670	-5.8	-20.0	-21.7 $\pm$ 1.8	-15.1	5.1 +1.5/-2.0
W8	dolomite nodule	680	-7.3	-7.6	-10.6 $\pm$ 1.6	-4.0	2.1 +0.6/-0.6
553	calcareous shale	677	-3.8	-13.0	-11.8 $\pm$ 1.6	-5.2	3.0 +0.9/-1.1
W7	dolomite nodule	670	-5.4	-5.5	-8.5 $\pm$ 1.7	-1.9	1.1 +0.3/-0.1
W3	dolomite nodule	654	-6.3	-5.7	-8.7 $\pm$ 1.6	-2.1	1.2 +0.4/-0.1
W2	dolomite nodule	649	-5.1	-5.5	-8.5 $\pm$ 1.7	-1.9	1.1 +0.3/-0.1
551	calcareous mudstone	647	-2.5	-11.6	-11.6 $\pm$ 1.6	-5.0	2.5 +0.7/-0.8
W1	dolomite nodule	645	-5.4	-5.8	-8.8 $\pm$ 1.6	-2.2	1.3 +0.3/-0.2
550	dolomite nodule	615	-11.3	-11.3	-14.3 $\pm$ 1.6	-7.7	3.4 +1.0/-1.3
554B	pedogenic calcite	570	-7.8	-19.7	-25.0 $\pm$ 1.7	-18.4	5.6 +1.5/-2.1
Mean Elevation (km)*							5.3 +1.5/-2.0
Mean Elevation (km)*							2.0 +0.6/-0.7

Lower Gazhacun Fm.

548	pedogenic calcite	559	-8.0	-20.1	-21.5 $\pm$ 1.5	-14.9	5.0 +1.4/-2.0
165Ca	pedogenic calcite	556	-6.9	-19.8	-18.8 $\pm$ 3.4	-12.2	4.5 +1.4/-1.7
165D	pedogenic calcite	556	-7.1	-20.0	-19.0 $\pm$ 3.4	-12.4	4.5 +1.4/-1.7
165Fa	pedogenic calcite	556	-6.9	-19.7	-18.7 $\pm$ 3.4	-15.0	5.0 +1.5/-1.9
165Fb	pedogenic calcite	556	-6.8	-19.7	-18.7 $\pm$ 3.4	-15.0	5.0 +1.5/-1.9
165Fc	pedogenic calcite	556	-5.9	-18.0	-17.0 $\pm$ 3.4	-13.3	4.7 +1.5/-1.8
165G	pedogenic calcite	556	-6.8	-19.6	-18.6 $\pm$ 3.4	-14.9	5.0 +1.5/-1.9
R2	pedogenic calcite	555	-7.0	-20.2	-19.2 $\pm$ 3.4	-15.5	5.1 +1.5/-1.9
547	pedogenic calcite	540	-6.0	-19.1	-18.1 $\pm$ 3.4	-14.4	4.9 +1.5/-1.8
546	pedogenic calcite	532	-6.4	-21.1	-20.0 $\pm$ 3.4	-16.4	5.3 +1.5/-2.0
543B	groundwater calcite	452	-3.3	-19.5	-18.5 $\pm$ 3.4	-11.9	4.4 +1.4/-1.6
543A	pedogenic calcite	450	-7.6	-19.4	-16.2 $\pm$ 1.0	-9.6	3.9 +1.2/-1.6
Mean Elevation (km)*							4.5 +1.5/-1.7

Riqongla Fm.

579	pedogenic calcite	410	-6.2	-18.9	-19.8	-13.2	4.7 +1.4/-1.9
576	groundwater calcite	290	-3.4	-20.4	-21.3	-14.7	5.0 +1.4/-2.0
575E	groundwater calcite	285	-3.7	-11.9	-12.8	-6.2	2.9 +0.9/-1.0
575C	groundwater calcite	280	-2.6	-16.8	-17.7	-11.1	4.3 +1.3/-1.7
575B	groundwater calcite	278	-3.8	-13.9	-14.8	-8.2	3.6 +1.1/-1.3
Mean Elevation (km)*							4.1 +1.3/-1.6

Nianbo Fm.

W0628-3	paleosol	44	-1.5	-24.9	-26.8 $\pm$ 3.7	-20.2	5.9 +1.5/-2.1
W0628-2	lacustrine limestone	34	-4.1	-24.6	-27.0 $\pm$ 3.8	-20.4	5.9 +1.5/-2.1
W0628-1	paleosol	0	-3.5	-18.6	-21.6 $\pm$ 1.1	-15.0	5.0 +1.4/-2.0

Mean Elevation (km) ± 5.6 +1.5/-2.1
-------------------------------------

Note: Samples with  $\Delta_{47}$  measurements are in bold. For these samples, their unique  $T(\Delta_{47})$  was used to calculate  $\delta^{18}\text{O}_w$ .

†  $\text{TM}^{\delta}\text{O}_c$  of all samples except the Nianbo Fm have been previously published in Currie et al. (2005) and Currie et al. (2016). All  $\text{TM}^{\delta}\text{O}_w$   $T$  temperature error is reported as the standard error of the mean or the clumped isotope measurements from that formation or sample type.

‡ low elevation  $\text{TM}^{\delta}\text{O}_w$  values: -6.6‰ for Rigongla and Gazhacun Fms; -4.6‰ for Oiyug Fm, based on WMMTs derived from Khan et al.

\* Temperature used for dolomite-water and calcite-water fractionation factors of lacustrine samples is the average of lacustrine calcite clumped isotope temperatures, as these would have the most similar depositional conditions.

\* Error estimates for mean elevations are reported as the quadrature of the model error for each elevation estimate.

#### Water-Carbonate Oxygen Fractionation Factors

calcite/water  $\zeta$  =  $\text{EXP}(((18.03 * 10^3/T) - 32.42)/1000)$  (Kim & O'Neil, 1997)

siderite/water  $\zeta$  =  $\text{EXP}(((2.62 * 10^6/T^2) - 2.17)/1000)$  (Zhang et al., 2001)

dolomite/water  $\zeta$  =  $\text{EXP}(((2.73 * 10^6/T^2) + 0.26)/1000)$  (Vasconcelos et al. 2005)

TABLE 3. ISOTOPIC DATA FOR ALL CLUMPED ISOTOPE SAMPLES

Sample & Lithology	Weight % - CO <sub>2</sub>	$\delta^{18}\text{O}_{\text{CO}_2}$ * (‰VPDB)	$\delta^{13}\text{C}$ (‰VPDB) <sup>†</sup>	$\delta^{18}\text{O}_{\text{CO}_2}$ (‰VSMOW) <sup>†</sup>	$\delta_{47, \text{SEWIG}}^{\dagger}$	$\Delta_{47, \text{COES}}^{\ddagger}$ (‰)	T( $\Delta_{47}$ ) (°C) <sup>#</sup>	$\delta^{18}\text{O}_w$ (VSMOW)**	Number of Analyses	Formation
<b>OIYUG BASIN</b>										
<b>Nodular &amp; Groundwater Calcite</b>										
621H	36	-27.4	-0.1 ± 0.0	12.4 ± 0.1	-9.4 ± 0.1	0.698 ± 0.016	13.0 ± 3.7	-27.6 ± 1.6	11	Oiyug
W0628-1	90	-18.6	-3.3 ± 0.0	22.1 ± 0.1	-2.7 ± 0.1	0.755 ± 0.011	0.7 ± 2.3	-21.6 ± 1.1	6	Nianbo
<b>Laustriine/Marl Calcite</b>										
6211	37	-28.0	1.3 ± 0.0	12.1 ± 0.0	-8.4 ± 0.0	0.689 ± 0.015	15.0 ± 3.5	-30.1 ± 1.5	12	Oiyug
W0628-2	11	-24.6	-3.3 ± 0.1	17.3 ± 0.3	-7.6 ± 0.2	0.572 ± 0.027	45.7 ± 8.3	-18.5 ± 2.9	3	Nianbo
<b>Pedogenic Calcite</b>										
555	21	-20.0	-5.8 ± 0.0	19.8 ± 0.1	-7.6 ± 0.1	0.668 ± 0.017	19.7 ± 4.2	-21.7 ± 1.8	7	Middle Gazhacun
554B	51	-19.7	-7.9 ± 0.0	20.0 ± 0.1	-9.2 ± 0.1	0.739 ± 0.017	3.9 ± 3.4	-25.0 ± 1.7	4	Middle Gazhacun
548	29	-20.1	-8.4 ± 0.0	19.6 ± 0.0	-10.1 ± 0.1	0.721 ± 0.020	7.6 ± 3.3	-21.5 ± 1.5	5	Lower Gazhacun
543A	55	-19.4	-7.7 ± 0.0	21.2 ± 0.0	-8.0 ± 0.0	0.625 ± 0.010	30.1 ± 2.6	-16.2 ± 1.0	4	Lower Gazhacun
579	18	-18.9	-5.8 ± 0.2	20.9 ± 0.1	-7.0 ± 0.3	0.711 ± 0.020	9.8 ± 4.3	-19.8 ± 1.9	6	Upper Rigongla
W0628-3	6	-24.9	-1.2 ± 0.1	14.6 ± 0.3	-8.1 ± 0.2	0.738 ± 0.040	5.3 ± 8.2	-26.8 ± 3.7	3	Nianbo
<b>Vein Calcite</b>										
5434V	N.D.	-27.1	-2.7 ± 0.0	14.6 ± 0.0	-9.9 ± 0.0	0.467 ± 0.014	83.3 ± 6.0	-15.1 ± 1.7	2	Lower Gazhacun
<b>PENBO BASIN</b>										
<b>Laustriine/Marl Calcite</b>										
504A	54	-17.8	-0.7 ± 0.1	23.1 ± 0.4	0.5 ± 0.4	0.549 ± 0.003	52.4 ± 1.2	-10.5 ± 0.4	3	Nianbo
448D	42	-12.0	-4.1 ± 0.1	29.2 ± 0.3	3.4 ± 0.3	0.586 ± 0.007	40.9 ± 2.4	-6.7 ± 0.9	2	Nianbo
P0929-c	29	-12.7	-3.3 ± 0.1	28.1 ± 0.0	3.1 ± 0.0	0.701 ± 0.023	11.9 ± 5.6	-13.1 ± 2.5	2	Nianbo
DL104-3b	34	-12.4	-2.4 ± 0.1	28.4 ± 0.2	4.4 ± 0.3	0.717 ± 0.022	8.5 ± 5.0	-13.6 ± 2.2	3	Nianbo
440D	N.D.	-16.3	-3.7 ± 0.1	24.9 ± 0.1	-0.6 ± 0.1	0.540 ± 0.006	55.2 ± 1.5	-8.5 ± 0.5	2	Nianbo
<b>Pedogenic Calcite</b>										
446D	54	-17.3	-3.0 ± 0.1	23.5 ± 0.1	-1.2 ± 0.1	0.557 ± 0.008	49.9 ± 2.9	-10.4 ± 1.0	3	Nianbo
440B	8	-17.2	-4.2 ± 0.1	23.7 ± 0.1	2.1 ± 0.1	0.726 ± 0.008	6.3 ± 1.8	-18.9 ± 0.8	2	Nianbo

\* = measured on Delta V gas bench

† = measured on MAT253

§ = Carbon Dioxide Equilibrium Scale of Dennis et al. (2011)

# = Zaarur et al. (2013); T(°C)=[(52800/( $\delta_{47}$ -0.0520))] 273.1\*\* = The measured oxygen isotopic composition of the carbonate and measured T( $\Delta_{47}$ ) are used to calculate the oxygen isotopic value of water in equilibrium with the carbonate. As some samples are inter-

"secondary" calcite, these water values are different than those used in the elevation calculations.

Note: The Zaarur et al. thermometer was determined on carbonate samples digested at 25 °C and is therefore most appropriate for our analyses. Temperatures derived from our least altered samples are in the Oiyug Basin and ~6-12 °C in the Penbo Basin. N.D. = No Data.

Italicized sample names,  $\Delta_{47}$  values, and calculated temperatures denote samples petrographically interpreted as geochemically altered or secondary calcite.

51

interpreted as

in the  $-1.30^{\circ}\text{C}$  range

TABLE 4. APATITE U-TH/HE THERMOCHRONOMETRY AND POTASSIUM FELDSPAR AR/R GEOCH

Sample name & mapped unit	Aliquot <sup>†</sup>	Corrected age (Ma) <sup>‡</sup>	F <sub>T</sub> <sup>§</sup>	<sup>238</sup> U (nmol/g)	<sup>232</sup> Th (nmol/g)	<sup>147</sup> Sm (nmol/g)	<sup>4</sup> He (nmol/g)	Mass (ug)
L0706-2 granite intrusion Penbo Basin	X	15.10 ± 0.10	0.703	100.968 ± 0.114	200.385 ± 0.888	113.781 ± 0.109	1.992 ± 0.010	3.31
	Y	16.56 ± 0.11	0.807	48.015 ± 0.072	95.882 ± 0.540	63.609 ± 0.031	1.204 ± 0.004	11.66
	Z	12.93 ± 0.08	0.727	75.998 ± 0.175	345.718 ± 1.483	422.563 ± 0.201	1.875 ± 0.008	4.17
		<b>Mean age (±1 <math>\hat{\sigma}</math>)</b>	<b>14.86 ± 1.83 Ma</b>					
L0706-3 granite intrusion Penbo Basin	X	11.50 ± 0.06	0.793	89.580 ± 0.180	473.757 ± 2.001	738.337 ± 0.301	2.347 ± 0.007	9.44
	Y	12.35 ± 0.07	0.742	179.654 ± 0.215	501.425 ± 2.131	399.745 ± 0.195	3.459 ± 0.011	4.88
	Z	14.36 ± 0.09	0.717	91.660 ± 0.177	199.523 ± 0.854	150.095 ± 0.094	1.811 ± 0.008	3.78
		<b>Mean age (±1 <math>\hat{\sigma}</math>)</b>	<b>12.74 ± 1.47 Ma</b>					

<sup>†</sup> Single crystal conventional (U-Th)/He analyses

<sup>‡</sup> (U-Th)/He ages are calculated from total measured abundances in all cases, not concentrations.

<sup>§</sup> Correction factor for a-ejection; Farley et al., 1996

Sample name & mapped unit	Aliquot	<sup>36</sup> Ar <sub>a</sub> (moles)	<sup>37</sup> Ar <sub>Ca</sub> (moles)	<sup>39</sup> Ar <sub>Cl</sub> (moles)	<sup>39</sup> Ar <sub>K</sub> (moles)	<sup>40</sup> Ar <sub>f</sub> (moles)	Apparent Age (Ma)	Error (Ma 2 $\sigma$ )
W0628-4 Rigongla Fm Oiyug Basin	1	6.27E-17	3.54E-15	6.52E-18	8.73E-15	7.09E-14	33.81	0.50
	2	1.17E-16	4.33E-15	2.61E-18	7.16E-15	6.92E-14	40.19	0.63
	3	8.62E-17	6.36E-15	3.56E-18	9.47E-15	8.02E-14	35.27	0.44
		<b>Inverse isochron age (±2<math>\sigma</math>)</b>	<b>28.90 ± 1.52 Ma</b>					

Notes: (1) Isotope abundances corrected for blank, mass discrimination, nucleogenic interferences and post-irradiation decay

(2) GA1550 flux monitor (age = 98.790 ± 0.543 Ma) used to calculate J = 0.00169000 ± 0.00001690

(3) Error reported at 2 $\sigma$  level and includes uncertainty in J

(4) Isotope abundances calculated with instrument sensitivity of 8.20 × 10<sup>-17</sup> moles/fA

## RONOLOGY RESULTS

---

---

Raw age (Ma)	U (ppm)	Th (ppm)	Sm (ppm)
10.44	24.21	46.50	114.05
13.24	11.51	22.25	63.760
9.21	18.22	80.22	423.58
8.98	21.48	109.93	740.11
9.02	43.08	116.35	400.70
10.14	21.98	46.30	150.46

---

---

---

---

$^{40}\text{Ar}^*$ (%)	$^{39}\text{Ar}_k$ (%)	K/Ca	Error (2 $\sigma$ )
79.28	34.44	1.06	4.92E-03
66.66	28.22	0.71	3.25E-03
75.89	37.34	0.64	2.79E-03

---

---



Table 5

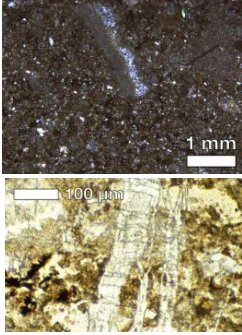
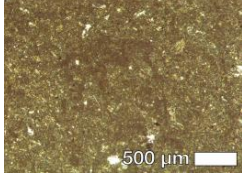
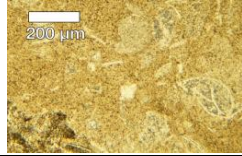
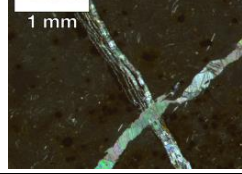
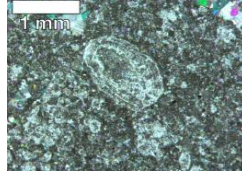
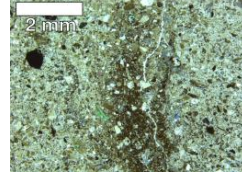
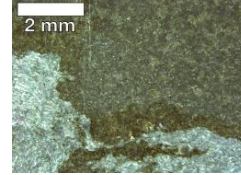
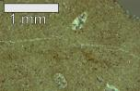

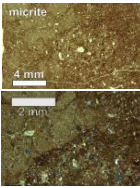

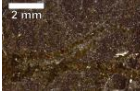

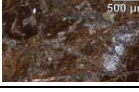
Sample	Petrographic Image	Textural Description	Petrographic Interpretation	T( $\Delta_{47}$ ) (°C)
446D		Abundant sparry calcite filling voids and veins; silicification	Diagenetic/High T	49.9 ± 2.9
DL104-3b		Micro-spar and small amount of dense micrite; recrystallized ostracodes; minor vuggy calcite spar	Primary/Low T	8.5 ± 5.0
P0929-c		Micro-spar with patchy dense micrite; sparry vuggy calcite; some silicification	Primary/Low T	11.9 ± 5.6
448D		Dense micrite to micro-spar; ostracodes; vein calcite and pyrite	Diagenetic/High T	40.9 ± 2.4
440D		Micro-spar/sparry calcite; silicification; ostracode fossils	Minor Alteration	55.2 ± 1.5
440C		Sparry calcite; calcite veins; silicification	Diagenetic/High T	---
446H		Coarse micro-spar/sparry calcite; fibrous calcite	Diagenetic/High T	---

Table 6

TABLE 6. PETROGRAPHY OF OIYUG BASIN CARBONATES				
Sample	Petrographic Image	Textural Description	Petrographic Interpretation	T( $\Delta_{47}$ ) (°C)
554B		Matrix-supported limestone Very fine grain micritic matrix Numerous microfossils <1mm	Primary/Low T	3.9 ± 3.4
555		Red-brown matrix with gray, micritic, cm-sized regions (labeled) No visible recrystallization or iron rims between calcite and oxidized siliciclastics	Primary/Low T	19.7 ± 4.2
579		Fissures traverse the slide from left to right (likely micron-scale veins) Abundant ~1mm rounded quartz crystals (sand clasts) Mud matrix Hematite rim on micritic region?	Minor alteration	9.8 ± 4.3
621I		Slightly recrystallized sparry calcite matrix mixed with micrite Finely laminated	Primary/Low T	15.0 ± 3.5
W0628-1		Clast-supported and loosely lithified Birefringent vein with an iron-stained rim of a different texture	Primary/Low T	0.7 ± 2.3
W0628-2		Clast-supported Extensive crosscutting of veins Pervasive infill of sparry calcite in fissures	Diagenetic/High T	45.7 ± 8.3
W0628-3		Matrix appears to have been micritic but has been extensively cross-cut by sparry veins	Diagenetic/High T	5.3 ± 8.2